Universität
Augsburg
University

Precipitation and humidity observation using a microwave transmission experiment and commercial microwave links

Dissertation zur Erlangung des Doktorgrades an der
Fakultät für Angewandte Informatik der
Universität Augsburg

vorgelegt von

Dipl.-Phys. Christian Chwala

2015

Erstgutachter:	Univ.-Prof. Dr. Harald Kunstmann
Zweitgutachter:	Univ.-Prof. Dr. Jucundus Jacobeit
Externer Gutachter:	Univ.-Prof. Dr.-Ing. Uwe Siart

Tag der mündlichen Prüfung: 21.12.2015

Contents

List of Figures

List of Tables

List of Symbols

$\boldsymbol{E}_{\text{inc}}$	Incident electric field
$\boldsymbol{E}_{\text{sca}}$	Scattered electric field
$\Delta\phi$	Change of phase angle
ΔA	Specific differential attenuation in dB
ΔC_{ext}	Differential extinction crosssection in m^2
ΔQ_{ext}	Differential extinction efficiency
ϵ_r	Relative permitivity
ϵ_r'	Real part of relative permitivity
ϵ_r''	Imaginary part of the relative permitivity
λ	Wavelength in m
$\mathscr{E}_{\text{dry}}$	Error rate for missing detection of dry event
$\mathscr{E}_{\text{mean}}$	Mean error rate
$\mathscr{E}_{\text{wet}}$	Error rate for missing detection of wet event
$\mathscr{F}$	Fourier transform
μ	Shape parameter of gamma DSD
μ_r	Relative permeability
ω	Hamming window
$\overline{A}$	Path averaged attenuation in dB
$\overline{R}$	Path averaged rain rate in mm/h

σ	Radar cross section in m^2
$\mathbf{S}$	Scattering matrix
$\vec{E}_0$	Electric field amplitude vector
$\vec{E}$	Electric field vector
$\vec{R}$	Vector of RSL values
A	Specific attenuation in dB/km
a	Parameter of the A-R and ΔA-R power law relation
B	Bandwidth in Hz
b	Parameter of the A-R and ΔA-R power law relation
c	speed of light in vacuum
c_n	Chebyshev shape parameters
C_{abs}	Absorption cross section in m^{-2}
C_{ext}	Extinction cross section in m^{-2}
C_{sca}	Scattering cross section in m^{-2}
D	Drop diameter in mm
D_0	Median volume drop diameter in mm
D_{a}	Drop diameter in horizontal direction in mm
D_{b}	Drop diameter in vertical direction in mm
f	frequency in GHz
F_{s}	Sampling rate
f_{divide}	Frequency at which power spectrum is divided in high and low part
k_b	Boltzmann constant = 1.381×10^{-23} J/K
k_{eff}	Effective wave number in m^{-1}
$k_{\text{eff}}^{\text{im}}$	Imaginary component of the effective wave number in m^{-1}
l	Inner length of trihedral reflector
M	Molecular weight of water: 18.02 g mol^{-1}
N	Refractivity

n	Refractive index
$N(D)$	Drop number concentration of the drop size distribution in $\mathrm{mm}^{-1}\ \mathrm{m}^{-3}$
N_0	Concentration parameter of gamma DSD in $\mathrm{mm}^{-(1-\mu)}\ \mathrm{m}^3$
N_0	Initial refractivity
P	Air pressure in mbar
$P(f,t)$	Power spectral density
P_0	Standard air pressure of 1013 hPa
P_r	Received power in dBm
P_t	Transmitted power in dBm
$P_{\text{mean dry}}(f)$	Mean dry spectrum
$P_{\text{norm}}(f,t)$	Normalized power spectral density
$P_{\text{sum diff}}(t)$	Difference of normalized low and high frequency spectral amplitudes
$P_{\text{sum high}}(t)$	Sum of normalized low frequency spectral amplitudes
$P_{\text{sum low}}(t)$	Sum of normalized low frequency spectral amplitudes
$P_{\text{thermalnoise}}$	Thermal noise power
$p_{\text{v,sat}}$	Water vapor saturation pressure in mbar
p_{v}	Water vapor pressure in mbar
q	Absolute humidity in $\mathrm{g/m}^{-3}$
q_{sat}	Absolute humidity at saturation level in $\mathrm{g/m}^3$
Q_{ext}	Extinction efficiency
R	Rain rate in mm/h
r	Path length in m
$r(\Theta)$	Distance of drop surface from center for Chebyshev shaped rain drop in mm
$R(t)$	RSL at time t
R_G	Gas constant: 8.3144621×10^{-2} mbar $\mathrm{m}^3\ \mathrm{mol}^{-1}\ \mathrm{K}^{-1}$
$R_{\text{base}}(t)$	RSL baseline at time t
RH	Relative humidity in %

T	Temperature in $^{\circ}C$
T_k	Temperature in Kelvin
v	Terminal velocity of rain drops in m/s
v_{P_0}	Terminal velocity of rain drops at standard air pressure in m/s
w	Wet and dry error rate weighting factor
x	Size parameter relating drop diameter to wavelength
DAQ	Data acquisition
DSD	Drop size distribution
DWD	German weather service (Deutscher Wetterdienst)
FFT	Fast Fourier transform
GPM	Global Precipitation Measurement
HF	High frequency
MODIS	Moderate Resolution Imaging Spectroradiometer
MW	Microwave
NWP	Numerical weather prediction
PCB	PC Board
SBC	Single board computer
STFT	Short term Fourier transform
TRMM	Tropical Rainfall Measuring Mission

1 Introduction

It's hard to make predictions, especially about the future.
— Markus M. Ronner

1.1 Motivation

1.1.1 Good models need good observations

How will the global average land surface temperature evolve? When will the rainy season in West Africa start? What will be the peak height of a river flood?

Since predicting the future is one of the core businesses in hydrology and atmospheric research, these are their typical questions. Hence, a wealth of models exits to describe the processes in the soil and atmosphere for a wide range of temporal and spatial scales. Even though these models are very different, they have two things in common. First, their performance has to be validated against a certain truth to judge their usefulness. Second, since the modeled processes are often chaotic (in the sense that small deviations in the present may results in large deviations in the future), their performance will depend on the correctness of the initial conditions [Lorenz, 1965]. Both require accurate measurements of the relevant parameters.

The spatial and temporal distribution of precipitation is one of the crucial parameters. For hydrological modeling it provides the relevant input to predict streamflow. For weather and climate forecasts it is one of the key output parameters which in turn is used by other models to e.g. predict flood or drought events. Atmospheric humidity also plays an important role. In particular the ability of weather models to predict convective events depends on the initial humidity field [Ducrocq et al., 2002].

That is, the accurate observation of precipitation and humidity is of utmost importance for the successful operation and development of forecasting models. However, due to the high spatial and temporal variability of precipitation and humidity, their observations may lack accuracy and spatial representativeness. This in particular true for precipitation. Thus an improvement of the current observation techniques is desired to enable future improvement of flood-, drought- and climate forecasts.

1.1.2 State of the art observation techniques and their limitations

Precipitation observation

Most commonly precipitation is observed using rain gauges. Being point measurement they lack spatial representativeness, though, in particular during convective events of small spatial size. Additional uncertainties are introduced by wind and exposure-induced errors [Nešpor and Sevruk, 1999, Sevruk and Zahlavova, 1994]. Rain gauge density varies from country to country and from region to region. In Germany the DWD operates one of the densest networks with more than 1 000 rain gauges. In less developed countries a much smaller number of gauges may be available for a much larger area. E.g. the number of gauges that is currently included in the global data sets for gauge based spatial precipitation estimation is in the order of 1 000 for the whole of South America.

In contrast to rain gauges, weather radar observations have a high spatial coverage. First weather radar measurements were already carried out in the 1940's and 1950's (see Atlas [1964] for a brief summary). From 1980 on many national meteorological services then began to install networks of weather radars. The DWD, for example, operates 16 C-Band radars to cover the whole of Germany. However, results of radar observations are impaired by several error sources. The relation of measured reflectivity and rain rate has a strong dependence on the drop size distribution which is usually unknown [Ulbrich and Lee, 1999]. Furthermore the variability of the vertical profile of reflectivity [Hazenberg et al., 2011, Smith et al., 1986], ground clutter, (partial) beam blockage and enhanced bright band interception can caused significant bias in rain rate estimates derived from weather radars. The latter two are particularly increased in mountain regions [Andrieu et al., 1997].

To improve the quantitative precipitation estimation from weather radars, many of the operational single polarization systems are being upgraded to dual polarization systems. In Germany the last two DWD C-band radars will be upgraded by the end of 2014. Similar e.g. in France and the United States. Compared to single polarization radars which only provided one reflectivity measurement Z_h, the dual polarization systems offer measurements of the differential reflectivity Z_{dr}, the specific differential phase shift K_{dp} and the co-polar correlation coefficient ρ_{hv}. These additional parameters can be used to estimate the DSD and to perform hydrometeor classification [Bringi and Chandrasekar, 2001]. In summary this leads to a significant improvement of the radar based quantitative precipitation estimation. The problem of beam blockage, ground clutter and the vertical profile of reflectivity however remain [Berne and Krajewski, 2013]. In addition radar calibration, in particular of Z_{dr}, poses a challenge in operational applications.

Typically the operational radar networks only cover the land area of a certain country, since they cannot reach out far on the ocean with their maximal range of around 200 km. For a global coverage, especially above the oceans, satellite measurements are necessary. The most prominent satellite mission dedicated to precipitation observation is the Tropical Rainfall Measuring Mission (TRMM). Since its launch in 1997 the TRMM satellite provides precipitation information by radar and radiometer measurements. The temporal and spatial resolution of its multi-satellite product ($0.25^\circ \times 0.25^\circ$ every 3 hours [Huffman et al., 2007]) is however poor compared to that of weather radar. TRMM's successor, the Global Precipitation

Measurement (GPM) core satellite, was launched in 2014 with the aim to improve resolution and accuracy [Hou et al., 2013]. With the fully established multi-satellite observatory revisit time over land will be in the order of one to two hours. Spatial resolution will increase down to 6 km. Even though this is a large step forward from TRMM, satellite measurements will not be of value for small scale convective precipitation events with only very duration and small spatial extent.

Humidity observation

Observations of atmospheric humidity (often also referred to as atmospheric water vapor) are mostly performed by operational surface stations and radiosonde measurements. Even though, the spatial and temporal variability of humidity is not as high as that of precipitation, the data from stations and radiosondes has only limited spatial representativeness.

Hence, new retrieval techniques have been developed to improve the spatial and temporal resolution of the observations. Cuccoli et al. [2001] investigated the potential of exploiting attenuation data from satellite up- and downlinks operating in the range of 22.235 GHz. Their simulation showed that data from up- and downlinks can be used to estimate the vertical profile of humidity. Besides attenuation data from a satellite signal, its time delay information can also be exploited to estimate atmospheric humidity. Bevis et al. [1992] derived water vapor column values using data from the Global Positioning System (GPS). The *UK Met Office* uses as similar approach and assimilates the total zenith delay derived from GPS receivers into their weather prediction system [Bennitt and Jupp, 2012]. They could show that the performance of cloud forecasts is improved with this additional assimilation.

As with precipitation observations, global coverage of humidity observations can only be provided by satellite measurements. The Moderate Resolution Imaging Spectroradiometer (MODIS) aboard two NASA satellites provides column water vapor with a spatial resolution of 1 km [Gao and Kaufman, 2003]. Due to the long revisit time, the temporal resolution is low though. Only daily data is available.

Much higher temporal resolution can be achieved using radar phase delay measurements Fabry et al. [1997], which where successfully tested during the International H2O Project (IHOP) [Weckwerth et al., 2005] and the REFRACTT project [Roberts et al., 2008]. This technique has proven to provide good spatial and temporal near-surface estimates of humidity. The range of the observations is however limited by the slope of the land and the number of available ground targets. Maximum achieved range was 60 km. In addition, the unwrapping of the aliased phase is challenging in an operational application.

1.1.3 Commercial microwave links as remote sensing tool

A new tool that provides important additional information on near-surface precipitation and humidity are commercial microwave links, like they are used in cell phone networks for most interconnections of the cell phone towers. They are typically operated in the frequency range between 10 GHz and 40 GHz. At these frequencies the propagation of electromagnetic radiation is considerably influenced by precipitation and atmospheric humidity.

In particular the interaction between microwave radiation and precipitation can cause

strong attenuation, i.e. large signal losses, which lead to disturbed communication along microwave links. Hence, this effect was studied since the early days of electromagnetic wave propagation research. A first description of the theory of the attenuating effect of precipitation was given by Stratton [1930]. Later, Mueller [1946] could prove the effect with experimental data. The motivation for both works, however, was to predict the attenuation caused by heavy rain, to assure working communication along microwave links during strong precipitation events. Hence, they treated precipitation as an unwanted source of disturbance.

The first to think the other way round, to exploit the disturbance of the signal and estimate rain rates from the attenuation, were weather radar researchers in the 1960s. They used corner reflectors as fixed radar targets and derived line integrated precipitation estimates from their attenuation measurements [Atlas, 1964]. Atlas and Ulbrich [1977] later introduced the concept of using microwave point to point links instead of the expensive weather radars to perform attenuation measurements. Based on this idea, several experiments with purpose-built microwave links were carried out to derive line integrated precipitation information from attenuation measurements [Holt et al., 2003, Leijnse et al., 2007a, Minda and Nakamura, 2005, Rahimi et al., 2004, Upton et al., 2005]. Rincon and Lang [2002] also showed that it is possible to estimate the line integrated drop size distribution (DSD) using a dedicated dual frequency microwave link. The number of those microwave link experiments was, however, still limited due to the costs involved in building and operating them.

This limitation was overcome by using attenuation data from existing commercial microwave link networks operated by cell phone providers [Messer et al., 2006]. Since those networks exist wherever a cell phone network exists, this technique can provide good spatial coverage in inhabited areas. The densities of the links varies, though. Denser populated areas exhibit a higher density, whereas the network is coarser in rural areas. According to reported figures of 100 000 links per 350 000 km^2 in Germany and 12 000 links per 35 000 km^2 in the Netherlands [Leijnse et al., 2007c] an average density of ≈ 0.3 links per km^2 can be assumed for European countries. Data is typically available with a time resolution of 1 to 15 minutes, depending on the acquisition scheme of the network operators.

Since the introduction of the method by Messer et al. [2006] with data from Israel, studies using commercial microwave links have been conducted in the Netherlands [Leijnse et al., 2007c, Overeem et al., 2011] and Switzerland [Schleiss and Berne, 2010]. In Israel and the Netherlands, where data from one or several cell phone providers is available countrywide, Zinevich et al. [2008] and Overeem et al. [2013] have shown that spatial rainfall information can be derived using a large number of microwave links. Furthermore, important analysis of the uncertainties introduced by wet antenna attenuation and the heterogeneity of the drop size distribution along the link have been performed [Leijnse et al., 2008, Zinevich et al., 2010].

With their line integrated nature and high temporal resolution, microwave links can provide a good complement to rain gauge and radar measurements, in particular in urban and mountain regions (see Figure 1.1). In sparsely gauged areas, e.g. in developing countries, they could even serve as sole data source.

Since atmospheric humidity also introduces attenuation of microwave signals [Liebe et al., 1991], data from commercial microwave link networks can be used to estimate near-surface

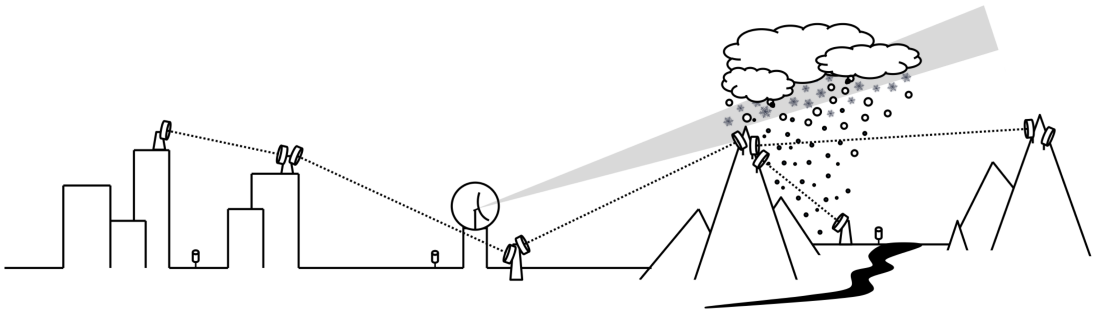

Figure 1.1 – Schematic of the observation of a small convective shower by gauges, weather radar and microwave links. This illustrates the disadvantages of radar measurements in urban and mountain regions. Beam blockage, ground clutter and the vertical variability of precipitation affect the accuracy of the radar based rain rate estimation. The low spatial representativeness of rain gauges is also apparent from the schematic. It has to be noted though, that the depicted case, with a very isolated rain event and a perfect coverage by microwave links, was chosen to illustrate the advantages of microwave links.

absolute humidity values as well [David et al., 2009]. Similar to the additional precipitation information provided by microwave link data, this could complement the coarse station observations for humidity.

1.1.4 The PROCEMA project

To initiate the research with commercial microwave links in Germany and to further the work carried out in Israel the virtual institute *Regional Precipitation Observation by Cellular Network Microwave Attenuation and Application to Water Resources Management* (PROCEMA) was funded by the *Helmholtz Association of German Research Centres* under grant VH-VI-314. Within PROCEMA scientists from the *Karlsruhe Institute of Technology* (KIT), the *Technische Universität München* (TUM), *Tel Aviv University* and the *Kinneret Limnological Laboratory* joined forces to fill the methodological gaps in this new and innovative technique.

For Germany the PROCEMA project was divided into three topics:

1. The in depth analysis of the interaction of microwave radiation with precipitation using drop by drop simulations of scattering [Hipp et al., 2011].
2. The development of a stochastic merging techniques for microwave link-, radar- and gauge data for improved spatial rainfall estimates.
3. The analysis of commercial microwave link signals and the development of a dedicated microwave transmission experiment.

This manuscript is the result of the research conducted for the third topic. The main development of the transmission experiment was done during the first 18 month of the project at TUM in Munich, whereas the analysis of commercial microwave link data and of the data from the transmission experiment were carried out at the KIT Campus Alpin in Garmisch-Partenkirchen.

1.2 Thesis Structure

1.2.1 Objectives

The main objectives of this thesis were:

- The establishment of computer code to calculate microwave attenuation at different frequencies caused by an ensemble of drops with variable drop size distribution
- The development of a dedicated dual frequency dual polarization microwave transmission experiment
- The analysis of commercial microwave link data in Germany

1.2.2 Outline

The thesis is organized around the two main topics. First, the development and operation of a dual frequency dual polarization microwave transmission experiment for precipitation and humidity remote sensing. Second, the exploitation of commercial microwave link data for precipitation remote sensing. The outline is as follows:

Chapter 1 is this introduction which gives a motivation for the research work and highlights the innovations.

Chapter 2 introduces the theory of microwave interaction with precipitation and humidity. The relevant parameters of precipitation are described and their effect on the attenuation of microwave radiation is studied in detail. For the relation between rain rate and microwave attenuation, power law relations are derived and the effect of temperature and drop size distribution on the power law parameters is examined. Furthermore the impact of atmospheric humidity on microwave radiation is presented. Its attenuating effect and its effect on the phase delay are described. Finally a relation between absolute humidity and phase delay is derived.

Chapter 3 summarizes the development of the dual frequency dual polarization microwave transmission experiment and presents first results. Starting from the experiment's requirements, a concept is derived and its realization is described. After an introduction of the test site and the setup, results for precipitation and humidity observation are presented. For precipitation, single- and dual-polarization measurements are used. Based on accompanying disdrometer measurements, these are then analyzed with regard to the impact of drop size distribution variations. The humidity observations are based on phase delay measurements from both frequencies which are then compared to weather station observations.

Chapter 4 covers the exploitation of data from commercial microwave link networks to estimate rain rates. Data from five microwave links in alpine and pre-alpine terrain are analyzed. A new algorithm for the detection of rain events in the microwave link data is presented. The resulting rain rates are compared to rain gauge data and weather radar observations.

Chapter 5 concludes with a summary of the realized work and the derived results. In addition an outlook for future research with the microwave transmission experiment and the commercial microwave links is given.

1.2.3 Innovations

The main innovations of this work are:

- The development, buildup and field installation of a monostatic dual frequency dual polarization microwave transmission experiment
- The comparison of dual polarization attenuation measurements simultaneously at two frequencies with attenuation data simulated from disdrometer drop size data
- The first line integrated estimation of absolute humidity changes by phase delay measurements with very high temporal resolution
- The first analysis of commercial microwave link data in Germany and at the same time the first analysis of commercial microwave link data in alpine terrain
- The development of a new wet/dry classification algorithm for received signal level time series

2 Theory of microwave interaction with precipitation and humidity

Observations always involve theory.

— Edwin Hubble

This chapter shall give an overview of the theory on which all observation techniques in chapter 3 and chapter 4 are based. It presents the basic principles of the interaction of microwave radiation with precipitation and humidity. A special emphasis is put on studying the influence of different rain fall parameters on microwave attenuation.

2.1 Microwave radiation and precipitation

The term microwave radiation refers to electromagnetic radiation in the frequency range from 1 GHz and 100 GHz. This electromagnetic radiation interacts with any dielectric particle in its path of propagation. A fraction of the incident radiation is absorbed, a portion is scattered and a remaining attenuated part propagates further. All three fractions depend on the relation between the incident radiation and the particle parameters. Hence, a measurement of the scattered power or a measurement of the attenuation that is caused along a certain path yields information about the scatterer.

This fact is the basis of microwave remote sensing. The fraction of radiation that is scattered back, usually in the opposite direction of the incoming radiation, is analyzed with radar devices. The attenuating effect of scatterers can be examined using a transmission experiment similar to the one presented in chapter 3 or by exploiting data from commercial microwave communication links, as presented in chapter 4.

Measurement alone are however of no value since they do not directly relate to the quantity of interest, e.g. the rain rate. To be able to draw conclusion about the scattering particles from the measurements, it is crucial to know the details of the interaction between the radiation and the scatterer. In case of precipitation, the relation between microwave radiation and precipitation particles or an ensemble of precipitation particles has to be analyzed. As a first step to do so, the individual particles which constitute precipitation, shall be described.

2.1.1 Properties of precipitation

The fact that their are different types of precipitation is obvious. Rain, snow and hail are easily distinguishable by eye. It is also easy to observe that precipitation consists of a large number of small particles (e.g. rain drops or snow flakes). But do they all have the same size and shape? Do the typical sizes change with the strength of the precipitation event? Do the drops all fall at a certain speed? Are they symmetric? How does all that impact the interaction with microwave radiation? And how can we accurately measure precipitation?

The following sections will discuss these questions, focusing on liquid precipitation (rain) since solid precipitation (snow, hail) is not analyzed within the scope of this work.

Rain rate

The most relevant parameter of precipitation for applications in hydrology and meteorology is the amount of water that is provided by a precipitation event in a given time. It is defined as the rain rate or rain intensity R in mm/h, which is a measure for the resulting water height per square meter in mm after a duration of one hour.

Measuring the rain rate at ground level is straight forward. The most simple device would be a bucket with a defined collection area. Rain rates can then be derived by recording the volume changes of collected rain water at given time intervals. This concept has been perfected by modern weighting rain gauges which determine changes of the recorded water volume with a very accurate scale. The other most common method is to use tipping bucket rain gauges.

Rain gauges directly observe the rain water arriving at the ground. No theoretical assumption are needed to derive rain rates from their measurements. Hence they are regarded as the truth concerning rainfall.

Since the area they can cover with their collection area is quite small (200 to 400 cm^2) and since the rain gauge network density is usually quite low (< 1 gauge per 10 km^2), their measurements lack spatial representativeness. This is in particular true in mountainous terrain where the installation of gauges is complicated and costly but where the spatial variability of rain fall is high due to the impact of the topography. The additional uncertainties introduced by wind and exposure-induced errors [Nešpor and Sevruk, 1999, Sevruk and Zahlavova, 1994] are also more dominant in complex terrain. To limit the influence of wind, wind shields can be installed at the gauge sites or pit gauges can be used.

Rain gauge measurements do not require any information on the precipitation particles. Microwave remote sensing techniques however depend on the interaction with each drop. Hence it is important to know how the ensemble of drops is related to the rain rate.

Rain rate is a flux of water volume and hence can be regarded as a part determining the volume and a part determining the velocity. With a drop diameter D in mm and the terminal velocity of the rain drops $v(D)$ in m/s the rain rate R in mm/h can be defined as the integral over the drop diameters in the unit volume by the equation

$$R = 0.6 \times 10^{-3} \pi \int_0^\infty v(D) D^3 N(D)\, dD \tag{2.1}$$

where $N(D)$ in 1/mm $1/m^3$ is the number concentration of the drops in the unit volume

per diameter [Bringi and Chandrasekar, 2001]. As will be shown in section 2.1.2 $N(D)$ also fundamentally determines the attenuation A of microwaves caused by rainfall. Hence , $N(D)$ links A and R together. It has to be noted however, that two different DSDs $N(D)$ can yield the same R, but the resulting values of A may be different. Or the other way round, different DSDs $N(D)$ can yield the same attenuation A, but different rain rates R. That is, knowing $N(D)$ and its properties is of crucial importance when rain rates shall be derived from attenuation measurements.

Drops size distribution (DSD)

Measuring the $N(D)$, is not as straight forward as measuring rain rate. The simplest measurement technique is to use dyed filter paper which is exposed to rain and then derive the drop sizes from the stains Kleinschmidt et al. [1935]. However this technique requires a lot of manual operation and is not usable for continuous measurements.

With the invention of the disdrometer by Joss and Waldvogel [1967] automated and continuous measurements were made possible. The disdrometer electronically recorded the impact of rain drops on a surface and calculated a DSD from the different kinetic energies of different drop sizes. Modern disdrometers, like the one used in this work and described in section 3.3, are based on an optical principle of operation. They detect the diameter and fall speed of a drop falling through a widened laser beam by analyzing the resulting shadow with a CCD camera. This optical detection principle is taken even one step further by the 2D video disdrometer Schönhuber et al. [1994]. It is capable of recording the true projected shape of precipitation particles with two perpendicularly looking cameras. Since it is not only detecting the horizontal diameter, complex shapes like those of snow crystal can be analyzed.

Similar to measurements with rain gauges, disdrometers also only provide point measurements and hence lack spatial representativeness. Estimates with a better spatial coverage can be derived with modern dual-polarization and/or dual-frequency weather radars [Bringi and Chandrasekar, 2001] and microwave transmission devices [Rincon and Lang, 2002].

Because the DSD is crucial for the interaction of microwave radiation with precipitation is has been studied since the beginnings of weather radar research, e.g. by Laws and Parsons [1943]. The first observations carried out to determine $N(D)$, suggested a negative exponential relation of the form

$$N(D) = N_0 e^{-\Lambda D} \tag{2.2}$$

with

$$\Lambda = \alpha R^{\beta} \tag{2.3}$$

where N_0 ($\mathrm{m}^{-3}\ \mathrm{mm}^{-1}$) is a concentration parameter and α and β are parameters determining the shape of the distribution.

However observed sudden changes in N_0 which occurred independently from R could not be represented well using equation (2.2). Ulbrich [1983] thus introduced an additional shape

Type	Abbreviation	N_0 in $\mathrm{mm}^{-(1-\mu)}\ \mathrm{m}^{-3}$	μ	Λ in mm^{-1}
Marshall Palmer	MP	0.80×10^4	0	$4.10\ R^{-0.210}$
Joss Drissle	JD	3.00×10^4	0	$5.70\ R^{-0.210}$
Joss Thunderstorm	JT	0.14×10^4	0	$3.00\ R^{-0.210}$
Laws-Parson	LP	$1.98 \times 10^4\ R^{-0.384}$	2.93	$5.38\ R^{-0.186}$

Table 2.1 – Parameters of equation (2.4) for the drop size distribution (DSD) of Marshall and Palmer [1948], the two types of Joss and Waldvogel [1969] for drizzle and thunderstorm, and a representation of the Laws and Parsons [1943] DSD taken from [Wolf, 2001]. JD and JT are two extreme cases which result in DSDs with a very small and a very large number of large drops, respectively. MP and LP should be representative for common wide spread rain events, where LP makes use of the shape parameter μ which, when positive, decreases the number of small drops.

parameter μ to represent the DSD by a gamma distribution of the form

$$N(D) = N_0 D^{\mu} e^{-\Lambda D} \tag{2.4}$$

where N_0 now has the units $\mathrm{mm}^{-(1-\mu)}\ \mathrm{m}^3$.

The slope parameter Λ of the exponential distribution can also be related to the median volume drop diameter D_0, which is defined such that the drops with $D < D_0$ contribute half of the total rain water content W. It can be written as

$$\frac{\pi}{6}\int_0^{D_0} D^3\, N(D)\, dD = \frac{1}{2}\frac{\pi}{6}\int_0^{\infty} D^3\, N(D)\, dD = \frac{1}{2}W. \tag{2.5}$$

For a gamma DSD this yields $\Lambda D_0 = 3.67 + \mu$, which can be used in equation (2.4) resulting in

$$N(D) = N_0 D^{\mu} e^{-(3.67+\mu)\, D_0^{-1} D}. \tag{2.6}$$

For the study of the effect of different DSD types on microwave attenuation, four classical drop size distributions commonly used in the literature will be employed. Their parameter sets for equation (2.4) are listed in table 2.1. Figure 2.1 shows the resulting DSDs for the different parameter sets for equation (2.4). In addition two examples of a measured DSD data are plotted. The data was recorded with the *Thies Laser Disdrometer* described in section 3.3.

The plots reveal that there is considerable difference between the four theoretical DSDs. Considering the three DSD types with $\mu = 0$, i.e. MP, JD, JT, MP lies in the middle between the two extreme cases JD and JT that are representative for drizzle (JD) and heavy precipitation in a thunderstorm (JT). The LP type in particular differs in the region of small drop sizes. This is due to the shape parameter μ which is non-zero for LP. As mentioned above, μ was introduced allow this effect. The measured disdrometer data clearly show that the shape parameter μ is necessary to be able to fit the theoretical DSDs to real measured data by increasing or decreasing the drop number towards small drop diameters.

With the obvious differences between the DSD types, the question arises, which one to

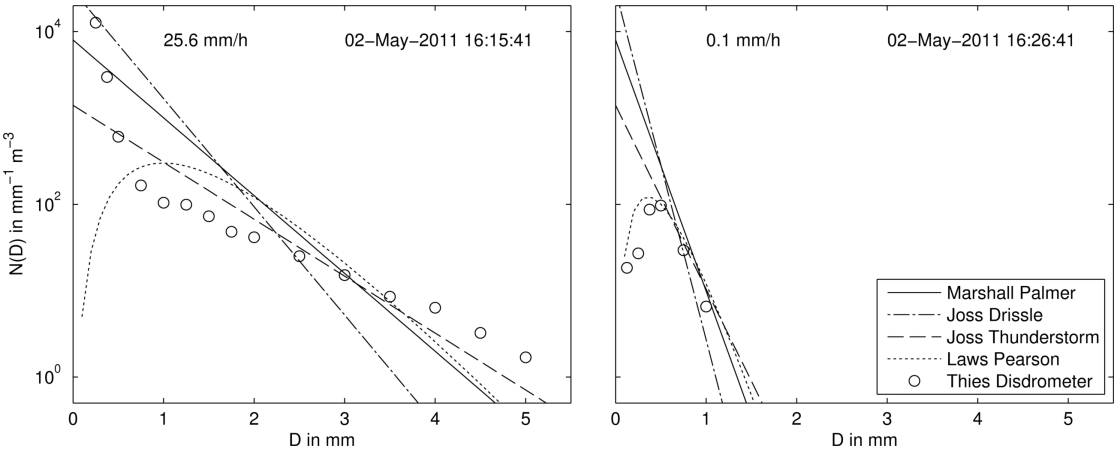

Figure 2.1 – Examples of different theoretical and measured drop size distributions (DSDs) for strong (left plot) and light (right plot) rain. The theoretical DSDs are derived using equation (2.4) and the values from table 2.1. The measured DSDs have been recorded by the disdrometer described in section 3.3

use if there is no measured DSD data available. Experimental data show that the spread of DSD parameters is even larger than the one covered by the four theoretical DSD types from table 2.1. Furthermore, the DSD changes from rain event to rain event and also within a rain cell, depending on the altitude and location within the cell [Ulbrich, 1983]. In particular at the onset of a rain event, large deviations can occur due to sorting processes of the falling drops [Kumjian and Prat, 2014]. That is, it is impossible to always use the "correct" DSD. However, the impact of the choice of the DSD type on the rain rate estimation is less severe for microwave transmission devices, than it is for radar, as will be shown in section 2.1.2. Hence, even though it is not optimal to estimate rain rates from microwave transmission measurements using a fixed DSD type, the uncertainties are much smaller than for radar derived rain rates.

It has to be noted that the rain rate which is used to calculate the theoretical DSD in equation (2.4) is not consistent with the rain rate that is calculated with equation (2.1) using the theoretical DSD and the theoretical terminal velocity v. Hence, in the following all rain rates corresponding to a theoretical DSD are not the ones to generate it, but are calculated from the theoretical $N(D)$ with equation (2.1) and (2.7).

Terminal velocity

The second integrand for the rain rate in equation (2.1) is the terminal velocity v of the rain drops, which is the maximum fall speed of a drop, where the gravitational force equals the drag force of the air. The assumption that the relevant vertical velocity of the drop, equals its terminal velocity is thus only valid in the absence of vertical wind. Nevertheless, this is a good approximation, except near obstacles where the horizontal wind component which is usually not equal to zeros is transformed to vertical wind.

Like the drop size distribution the terminal velocity has been studied since the beginnings of weather radar research. One of the first accurate data sets of the relation of the terminal

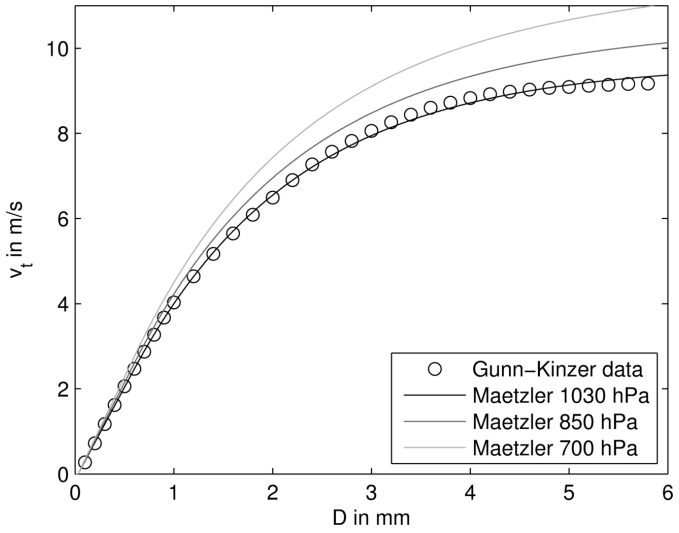

Figure 2.2 – The terminal velocity of rain drops. Shown is the data acquired by Gunn and Kinzer [1949] and the approximation by Mätzler and Martin [2003] described in equation (2.7) for different values of atmospheric pressure.

velocity v to the drop diameter D was given by Gunn and Kinzer [1949]. They measured the fall time of artificially produced charged water drops for laboratory conditions at sea level with two inducting rings as start and stop triggers. Their data could be explained later by a physical model of Beard [1976] which fitted the data very well. An approximation of this model is given by Mätzler and Martin [2003] which calculates terminal velocity at standard air pressure P_0 = 1013 hPa as

$$v_{P_0} = \begin{cases} 0 & \text{if } D \le 0.03\text{mm} \\ 4.323\,(D - 0.03) & \text{if } 0.03\text{mm} < D \le 0.6\text{mm} \\ 9.65 - 10.3\,e^{-0.6\,D} & \text{if } D > 0.6\text{mm} \end{cases} \tag{2.7}$$

where v_{P_0} is in m/s and the drop diameter D in mm. The third expression stemming from [Atlas et al., 1973] and being widely used would cause negative fall velocities for D<0.11 mm. With the second expression, which is a linear fit to measurements of Gunn and Kinzer [1949], this problem is avoided for drops down to D>0.03 mm.

Since the drag force that limits the terminal velocity depends on the density of the air, an adjustment of v_{P_0} with air pressure P is made resulting in the adjusted terminal velocity

$$v = v_{P_0} \left(\frac{P_0}{P} \right)^{0.291 + 0.0256\,D} . \tag{2.8}$$

Figure 2.2 shows the resulting terminal velocities for different air pressures compared to the data of Gunn and Kinzer [1949]. For the relevant range of drop diameters for rain 0 mm < D < 5 mm, the approximation from equation (2.7) fits the data very well.

Regarding the accuracy of the theoretical DSD it shall be noted that not all drops fall at

their terminal velocity all the time. Large drops which fall at their high terminal velocity occasionally break up and the resulting smaller drops first continue to fall at the high velocity of their parent drop before relaxing to the terminal velocity corresponding to their diameter [Montero-Martínez et al., 2009].

Drop shape

The interaction of microwave radiation with rain drops depends on the size and also on the shape of the drops. This is due to the fact that microwave based communication and remote sensing systems like the ones employed in chapter 3 and 4 used polarized radiation. That is, a vertically polarized microwave will be affected most by the vertical extension of the scatterer, likewise in horizontal direction. As a consequence, knowledge of the shape of rain drops falling at terminal velocity is of importance to accurately describe the interaction.

Theoretically deriving the shape of a falling rain drop is a complex task. It involves relating the air drag forces and the surface tension to the shape and even considering flow patterns within the rain drop. Pruppacher and Beard [1970] give an explanation of all those effects and present experimental results from wind tunnel measurements. For drops with $D \geq 0.5$ mm they found a linear relation of the ratio between horizontal and vertical axis of the drops. For smaller drops a more complicated relation is suggested. Thus, for this work, an approximation by a quadratic dependence on D is used for small drops, leading to the ratio

$$\frac{D_\mathrm{b}}{D_\mathrm{a}} = \begin{cases} 1.00 - 0.128\,(D/2)^2 & \text{if } D < 0.5\text{mm} \\ 1.03 - 0.124\,(D/2) & \text{if } D \geq 0.5\text{mm} \end{cases} \tag{2.9}$$

where D_b and D_a are the minor (vertical) and major (horizontal) axes of the drops. The drop shape is then approximated as an oblate spheroid.

Photographs of falling rain drops show that the actual rain drop shape deviates from an oblate spheroid, in particular on the bottom, where the shape is flattened. Savic [1953] proposed to describe the shape of the surface of a falling drop in gas as a generalized Chebyshev shape. It is rotationally symmetric about the vertical axis and the distance of the surface from the center is given by

$$r(\Theta) = \frac{1}{2} D \left(1 + \sum_{n=0}^{\infty} c_n \cos n\Theta\right) \tag{2.10}$$

where Θ is the angle to the axis of symmetry and D is the diameter of a sphere with equal volume. Chuang and Beard [1990] give a set of c_n which produces drop shapes in good agreement to the photos taken in the wind tunnel experiment by Pruppacher and Beard [1970]. They will hence be used in the following analysis. Figure 2.3 shows example drop shapes for the oblate spheroid and the generalized Chebyshev shapes which serve as basis for calculating the attenuation in the next section.

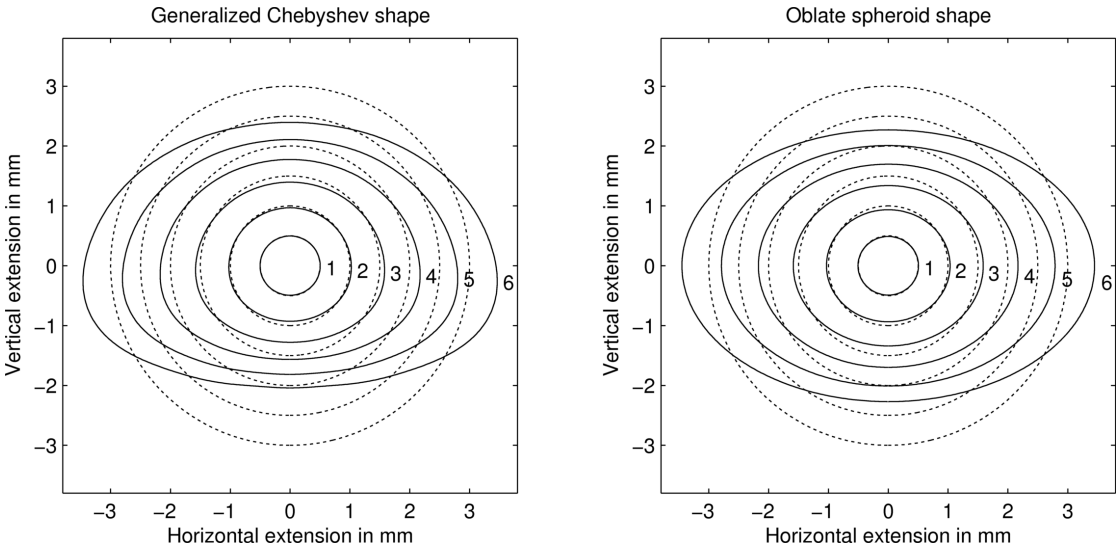

Figure 2.3 – Rain drop shapes approximated by a generalized Chebyshev shape [Chuang and Beard, 1990] and by an oblate spheroid [Pruppacher and Beard, 1970]. The dotted lines indicate a spherical drop with the same equivolume diameter.

Refractive index of water

When a rain drop is illuminated by electromagnetic radiation, it's not only its shape that is of importance to describe scattering and absorption processes. The refractive index n, which governs the propagation speed of radiation and refraction at the interface between two media, has to be considered. For a raindrop the refractive index of liquid water without salt is used. It exhibits a dependence on the frequency of the incident wave f and the water temperature T, which can be explained by relaxation and resonance effects of the H_2O molecules with the electromagnetic radiation.

The refractive index equals

$$n = \sqrt{\epsilon_r \mu_r} \tag{2.11}$$

where ϵ_r is the relative permitivity and μ_r is the relative permeability. The later describing the response to a magnetic field is very close to one so that $n = \sqrt{\epsilon_r}$. The relative permitivity of water is a complex quantity,

$$\epsilon_r = \epsilon_r' - i\epsilon_r'' \tag{2.12}$$

where ϵ_r' is the real part and ϵ_r'' is the imaginary part which describes the loss radiation experiences in water.

A detailed model describing ϵ_r is provided by Liebe et al. [1991]. Fitting their model to experimental data they obtained

$$\epsilon_r(f) = \frac{\epsilon_0 - \epsilon_1}{1 - i(f/\gamma_1)} + \frac{\epsilon_1 - \epsilon_2}{1 - i(f/\gamma_2)} + \epsilon_2 \tag{2.13}$$

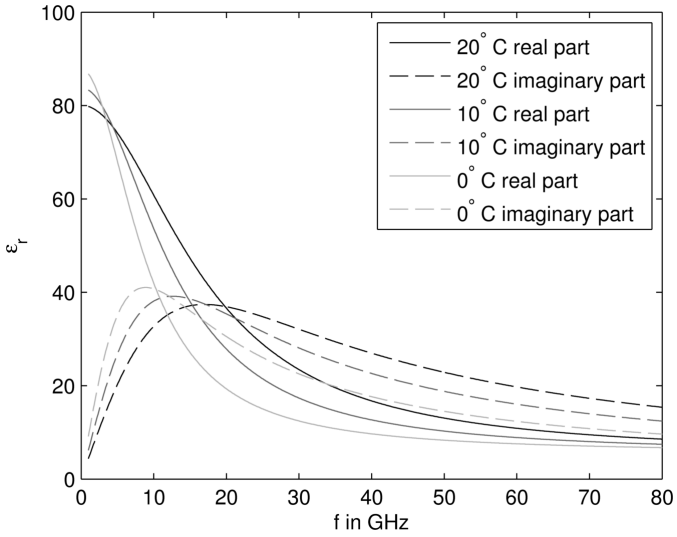

Figure 2.4 – Real and imaginary part of the refractive index ϵ_r of water for different temperatures.

where

$$\epsilon_0 = 77.66 - 103.3\,\Theta, \tag{2.14}$$

$$\epsilon_1 = 0.0671\,\epsilon_0, \tag{2.15}$$

$$\epsilon_2 = 3.52 + 7.52\,\Theta \tag{2.16}$$

and

$$\gamma_1 = 20.20 + 146.4\,\Theta + 316\,\Theta^2 \text{ GHz} \tag{2.17}$$

$$\gamma_2 = 39.8\,\gamma_1 \tag{2.18}$$

with

$$\Theta = 1 - \frac{300}{273.15 + T} \tag{2.19}$$

a relative inverse representation of the temperature T in $°C$. The resulting real and imaginary part of $\epsilon_r(f)$ for a different water temperatures are shown in figure 2.4.

2.1.2 Attenuation by rain drops

To explain the effect rain drops have on the propagation of microwave radiation, it is important to understand how electromagnetic waves interact with matter. This section shall present the fundamentals necessary for the following analyses. A detailed derivation of all necessary mathematical calculations can be found in the standard text books for electrodynamics e.g. Ishimaru [1978].

In the cases examined in this work, the microwave radiation is always a monofrequent and

linearly polarized plain electromagnetic wave. The scattering particles, here the rain drops, in general, can be regarded as an aggregation of a large number of discrete elementary charges, which will be excited by the incident wave. Because of the excitation, which extracts some of the incident energy, secondary electromagnetic waves are radiated. Their superposition yields the total elastically scattered field. If the elementary charges do not oscillate in phase with the incident wave, energy is dissipated and hence absorbed by the scatterer. Both effects reduce the amount of energy of the incident wave. The resulting wave directly in the direction of propagation therefore experiences a loss, the extinction, which is equal to the sum of the absorbed and scattered energy. To quantify these magnitudes the so called cross sections C_{ext}, C_{abs} and C_{sca} of the extinction, absorption and scattering have to be calculated. Their unit is m^{-2}. According to the above considerations they are related by the equation

$$C_{\text{ext}} = C_{\text{abs}} + C_{\text{sca}}. \tag{2.20}$$

For one scatterer, by definition, C_{ext} determines the attenuation it causes. For a group of scatterers, two cases have to be distinguished to calculate the total attenuation. In the first case the secondary waves emitted from a scatterer significantly contribute to the incident field of the other scatteres. Calculations of the total extinction thus have to take into account all secondary waves of all particles which are then scattered again by all other particles. Within a typical observation area or volume for microwave remote sensing of precipitation, one would have to deal with millions of scattering particles. Hence, calculation and even computation of the total extinction would get time consuming if not impossible. Fortunately, for scattering by rain drops in natural rain showers, the second case can be assumed where secondary waves can be neglected due to the low density of scatteres. Single-scattering approximation is valid and the attenuation caused by a group of rain drops is only dependent on the individual values of C_{ext}.

Attenuation by a given DSD

To introduce the basic theory of attenuation one assumes an electromagnetic field of a plane wave with an amplitude $\vec{E}_0$ propagating along the z-axis in a medium with the effective wave number k_{eff} in m^{-1}

$$\vec{E} = \vec{E}_0 \exp\left(-i\, k_{\text{eff}}\, z\right). \tag{2.21}$$

The attenuation per unit distance can then be written as

$$\frac{|\vec{E(z)}|}{|\vec{E(0)}|} = \exp\left(-k_{\text{eff}}^{\text{im}}\, z\right) \tag{2.22}$$

where $k_{\text{eff}}^{\text{im}}$ is the imaginary part of k_{eff}. With the relation

$$k_{\text{eff}}^{\text{im}} = \frac{1}{2} \int_D C_{\text{ext}}(D)\, N(D)\, dD \tag{2.23}$$

for a DSD with N(D) in the unit volume (detailed derivation in e.g Bringi and Chandrasekar [2001] section 1.10) the specific attenuation A in the common units dB/km can be derived from equation (2.22), resulting in

$$A = 20 \log \frac{|\vec{E(z)}|}{|\vec{E(0)}|} = -8.686\, k_{\text{eff}}^{\text{im}} \times 10^3 \tag{2.24}$$

$$= 4.343 \times 10^3 \int_D C_{\text{ext}}(D)\, N(D)\, dD. \tag{2.25}$$

Given that $N(D)$ is known, one only needs to determine $C_{\text{ext}}(D)$ to calculate the attenuation for a certain rain event.

Methods for the calculation of $C_{\text{ext}}(D)$ depend on the relation between wavelength λ in m and drop diameter D in mm. The Rayleigh approximation can be used to calculate C_{ext} if the size parameter

$$x = \frac{2\pi \, \frac{D}{2} \times 10^{-3}}{\lambda} \ll 1. \tag{2.26}$$

This would simplify the calculation. But with typical wavelengths for microwave communication and remote sensing system of $\lambda \approx 1$cm and typical rain drop diameters of up to 0.5 cm, equation (2.26) is not fulfilled. The approximation with geometric optics, where $x \gg 1$, is also not applicable. Since $x \approx 1$ the interaction between the incident wave and the scatterer happen in the resonance region. There, the excited field inside the scatterer can become quite large because the wavelength of the exciting wave matches the inner size of the drop which then acts as a resonator.

In case of the calculation of the attenuation of microwave radiation due to rain drops, directly solving the Maxwell's equations is necessary. One option is to use the Mie solution. Olsen et al. [1978] shows how they can be employed to calculate attenuation for different theoretical DSD types. However, the Mie solution is only applicable for spherical scatterers. Since the shape of rain drops deviates significantly from a sphere (Figure 2.3) a more sophisticated method will be needed to be able to calculate C_{ext}.

Calculation of the extinction cross section C_{ext}

For calculating the scattering of electromagnetic waves by resonant non-spherical particles, the T-Matrix approach introduced by Waterman [1971] has become a standard tool. A thorough review of the method can be found in Mishchenko et al. [1996]. The first author also provides a computational implementation written in FORTRAN, which is freely available at his website (http://www.giss.nasa.gov/staff/mmishchenko/t_matrix.html).

For the following calculations the double precision T-matrix code for non-spherical particles with fixed orientation is used. The code was slightly modified to be directly embedded in MATLAB via a custom MEX-file, which allows to use custom C or FORTRAN code directly in MATLAB. Calculations were carried out for a frequency range from 1 GHz to 80 GHz and drop diameters from 0.125 mm to 5.5 mm. Both drop shapes, the oblate spheroids and generalized Chebyshev type, described in section 2.1.1, were used. The refractive index of water was

calculated according to equation (2.13). Since numerical procedures of the double precision code exhibit convergence problems for the larger Chebyshev shaped particles, the maximum frequency and diameter is limited to the selected range. However, rain drops with $D > 5$ mm are uncommon and the frequency range of the applications in this work is within the chosen range.

The T-Matrix code returns the scattering matrix

$$\mathbf{S} = \begin{pmatrix} S_{11} & S_{12} \\ S_{21} & S_{22} \end{pmatrix} \tag{2.27}$$

which relates the incident field $\boldsymbol{E}_{\mathrm{inc}}(0)$ to the scattered field $\boldsymbol{E}_{\mathrm{sca}}(r)$ at the distance r by

$$\boldsymbol{E}_{\mathrm{sca}}(r) = \mathbf{S}\,\boldsymbol{E}_{\mathrm{inc}}(0)\,\frac{\exp(-i\,k\,r)}{r} \tag{2.28}$$

which can be written in vector form as

$$\begin{pmatrix} E_{\mathrm{sca}\perp}(r) \\ E_{\mathrm{sca}\parallel}(r) \end{pmatrix} = \begin{pmatrix} S_{11} & S_{12} \\ S_{21} & S_{22} \end{pmatrix} \begin{pmatrix} E_{\mathrm{inc}\perp}(0) \\ E_{\mathrm{inc}\parallel}(0) \end{pmatrix} \frac{\exp(-i\,k\,r)}{r} \tag{2.29}$$

where $E_\perp$ and $E_\parallel$ denote the component perpendicular and parallel to the scattering plane. For linearly polarized radiation, $E_\perp$ and $E_\parallel$ can be regarded as horizontal and vertical polarization. Since this work only considers copolar quantities, i.e. where the polarization of incident and scattered wave are equal, only the diagonal components S_{11} and S_{22} are relevant in the following.

The scattering matrix **S** is dependent on the angles of the incident and scattered wave and the drop orientation angles. They where chosen so that the incident and scattered wave propagate in the same direction and are perpendicular to the axis of rotational symmetry of the drop. Employing the optical theorem, which states that the extinction cross section C_{ext} is linked to the imaginary part of the forward scattering amplitude S_{forward} (e.g. Ishimaru [1978]) by

$$C_{\mathrm{ext}} = \frac{4\pi}{k}\,\mathrm{Im}(S_{\mathrm{forward}}) \tag{2.30}$$

the demanded extinction cross sections for vertical and horizontal polarization are given by

$$C_{\mathrm{ext,V}} = \frac{4\pi}{k}\,\mathrm{Im}(S_{11}) \tag{2.31}$$

$$C_{\mathrm{ext,H}} = \frac{4\pi}{k}\,\mathrm{Im}(S_{22}) \tag{2.32}$$

where $k = \omega/c = 2\pi f/c$ and c the is speed of light.

Since C_{ext} contains the effect of the the geometric scattering cross section σ_{geo} (in our case,

the frontal projection area of the drops), it is interesting to look at the extinction efficiency

$$Q_{\text{ext}} = \frac{C_{\text{ext}}}{\sigma_{\text{geo}}} \tag{2.33}$$

which better reveals the resonant effect which occurs if the size parameter $x = 1$. Figure 2.5 shows the computed values of Q_{ext}, C_{ext} and the integrand $N(D) \cdot C_{\text{ext}}$ of equation (2.25) for two frequencies and the whole range of drop diameters D. The two frequencies are the same that are used by the transmission experiment in chapter 3. Drop diameters were restricted to $D < 6$ mm, which is generally regarded as the physical upper limit for rain drops.

Dependence of C_{ext} on drop diameter

As pointed out by Atlas and Ulbrich [1977] and Leijnse et al. [2007b], $v_t D^3$ and C_{ext} have almost the same slope in the log-log plot for 34.8 GHz. That indicates an almost linear relation between A and R at this frequency and a low dependency of the A-R relation on the DSD shape. There is, however, a significant deviation between C_{ext} and $v_t D^3$ for drops larger than approximately 2.5 mm. That is, if a sufficient number of large drops is present in the rain event, this linearity of A-R and its low dependence on the DSD shape, will vanish. The diameter at which this deviation between C_{ext} and $v_t D^3$ starts depends on the transition from Rayleigh scattering to resonance scattering [Aydin and Daisley, 2002]. As mentioned before this takes place when the size parameter $x = 1$ (see equation (2.26)). For 34.8 GHz this is true at $D \approx 2.7$ mm. This can also be seen by looking at the extinction efficiency Q_{ext}, shown in the top row of Figure 2.5 where the main resonance peak can be found around 2.7 mm.

For 22.235 GHz the deviation from the slope of $v_t D^3$ is more pronounced, which indicates a less linear relation between A and R at this frequency. Due to the longer wavelength, the resonance scattering becomes dominant at a larger diameter than at 34.8 GHz. The asymmetry of the drops is thus larger at the 22.235 GHz resonance peak. Hence the difference between C_{ext} for horizontal and vertical polarization is more pronounced at 22.235 GHz than at 34.8 GHz for drop diameter D > 4.2 mm. $C_{\text{ext,22,h}}$ even exceeds $C_{\text{ext,35,h}}$ for large drops (the indices of C_{ext} indicate the frequency and polarization). That is, in the presence of large drops the attenuation and differential attenuation at 22.235 GHz can be very close to the values at 34.8 GHz, or even exceed them.

It is also interesting to analyze how the product of the extinction cross section and the DSD $C(D)_{\text{ext}} N(D)_{\text{MP}}$ behaves, since it is the integrand in equation (2.25) which is used to calculate the attenuation A. Hence the weight the different drop sizes contribute to the overall attenuation becomes visible. This is shown in the bottom row in Figure 2.5. The distribution of $C(D)_{\text{ext}} N(D)_{\text{MP}}$ peaks in the range of $D = 1$ mm to $D = 3$ mm. With increasing rain rate, the peak is shifted towards larger drops, since an increasing rain rate yields an increasing number of large drops. Comparing the two frequencies, it is obvious that $C_{\text{ext}} \cdot N(D)_{\text{MP}}$ is smaller for 22.235 GHz, which will result in a smaller attenuation for the same rain rate. It has to be noted, however, that for 34.8 GHz a considerable part of $C_{\text{ext}} \cdot N(D)_{\text{MP}}$ is contributed by diameters larger than the diameter at the first resonant scattering peak $D_{x=1}$ where $x = 1$ (dashed line in Figure 2.5). The kink in C_{ext} at $D_{x=1}$ decreases the contribution large drops have to the overall

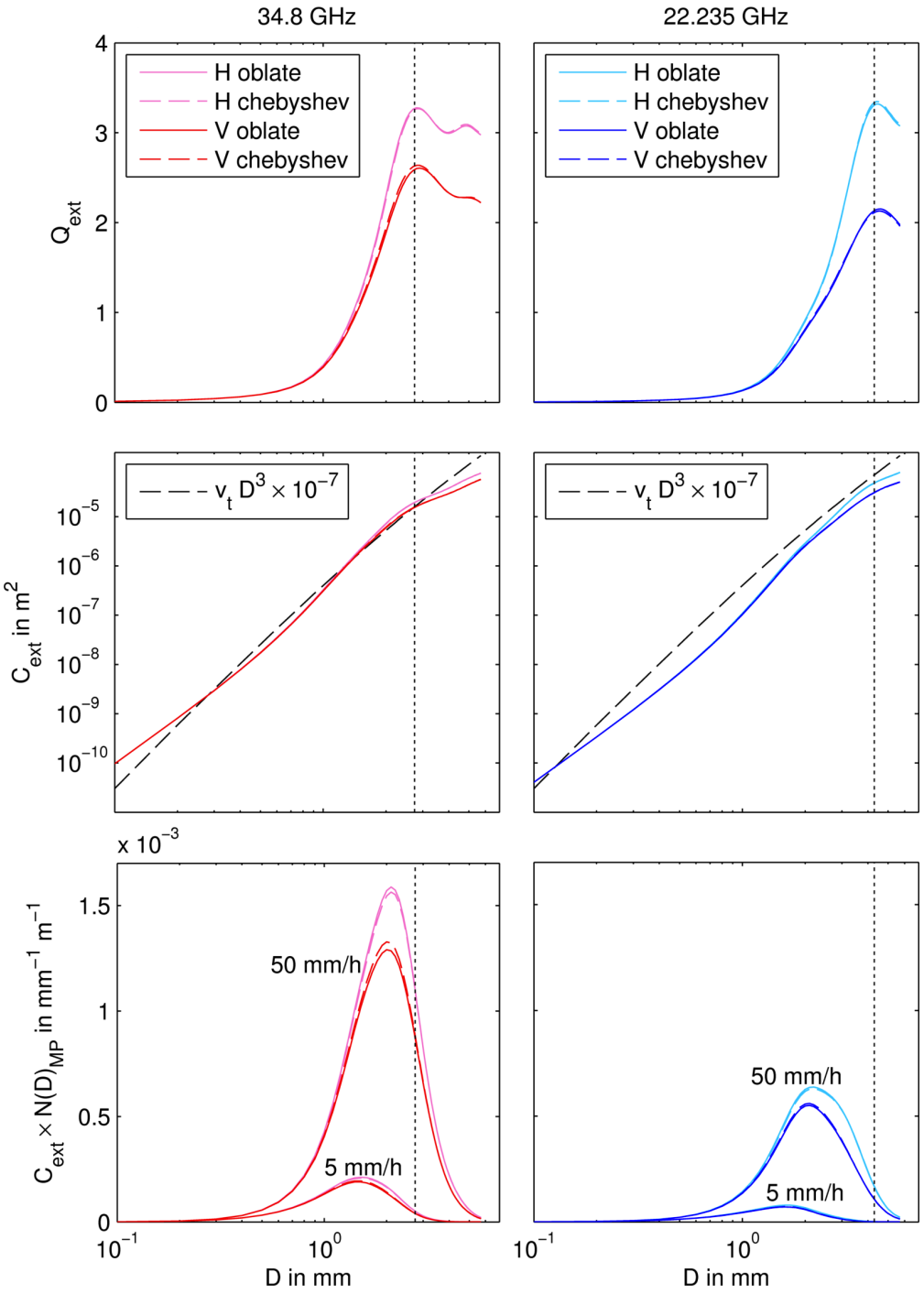

Figure 2.5 – Plots of the results from the T-Matrix calculations for the extinction efficiency Q_{ext} and extinction cross section C_{ext} for different rain drop shapes (oblate spheroid and generalized Chebyshev) and the two frequencies used for the experiments in section 3. The dotted line indicates where the size parameter $x = 1$, that is, where the effect of resonance is most prominent. The dashed black lines in the middle row visualize the integrand of equation (2.1) which takes the same place as C_{ext} in equation (2.25). The plots in the bottom row show the integrands of equation (2.25) and hence indicate the weight of the different drop diameters to the attenuation for a given rain rate. A Marshall-Palmer DSD was used to derive the applied $N(D)_{\text{MP}}$.

attenuation at 34.8 GHz. Since $D_{x=1}$ is larger for 22.235 GHz the effect of the kink is mitigated because it only affects the largest drops. As a consequence, the changes in the concentration of large drops will have a different impact on the attenuation for 34.8 GHz and 22.235 GHz. More details are discussed in the subsection on page 25.

Dependence of $C_{\mathbf{ext}}$ on drop shape

Figure 2.5 also shows the difference between calculations using an oblate spheroid drop shape and a generalized Chebyshev shape (see Figure 2.3). The deviations are generally very small. The only notable difference can be observed near $x = 1$ (dashed black line) for 34.8 GHz and vertical polarization. Since the differences and uncertainties introduced later in this section are more significant and since the computation time for the Chebyshev shape is quite high, the oblate spheroid shape is used in all following analyses.

Dependence of $C_{\mathbf{ext}}$ on temperature

As shown in Figure 2.4 the refractive index ϵ_r exhibits a temperature dependence which can be significant at certain frequencies. E.g. at around 30 GHz a change from 0°C to 20°C introduces a change of approximately 30% for both the real and the imaginary part. Hence it is necessary to examine the temperature dependence of C_{ext}. Similar to Figure 2.5, Figure 2.6 shows the computed values of $Q_{\text{ext}}(D)$, $C_{\text{ext}}(D)$ and the integrand $C_{\text{ext}}(D) \cdot N(D)$ of equation (2.25), now for different rain drop temperatures.

Compared to the variation of the drop shape, which has little effect, the different rain drop temperatures results in a visible deviation of the scattering parameters. The plot for Q_{ext}, with the linear y-axis, shows deviations for drop diameters $D > 1$mm whereas the plot for C_{ext}, with the logarithmic scale on the y-axis, reveals deviations for small drops.

Since the temperature response of ϵ_r is similar for 22.235 GHz and 34.8 GHz, the deviations of Q_{ext} and C_{ext} are similar for both frequencies and both polarization. For 34.8 GHz a slightly higher amplitude of the deviation can be observed. This can be explained by the slightly higher temperature dependent amplitude change of ϵ_r.

Looking at $C_{\text{ext}}(D) \cdot N_{\text{MP}}(D)$ in the bottom most plot of Figure 2.6, there is however a difference between 22.235 GHz and 34.8 GHz. At 34.8 GHz a temperature increase yields a decreased maximum of the peak, while the drop diameter of the peak stays the same. At 22.235 GHz the maximum increases but the peak also gets shifted towards smaller drop diameters. The cause for this is the opposing effect a temperature change has on C_{ext} for $D > 2$ mm and $D < 2$ mm. For $D > 2$ mm a temperature increase leads to decreased C_{ext}. For $D < 2$ mm a temperature increase leads to an increase of C_{ext}. This causes $C_{\text{ext}}(D) \cdot N_{\text{MP}}(D)$ to rise earlier at smaller drop diameters, so that its peak is is shifted to smaller drop diameters.

Dependence of A-R relation on temperature

Figure 2.6 has shown the temperature dependence of the scattering for a single drop with a given diameter. It does however not reveal how a temperature change effects the total attenuation for a ensemble of drops for a given rain rate. This relation between A and R is shown in Figure 2.7 for a Marshall-Palmer DSD and three different rain temperatures.

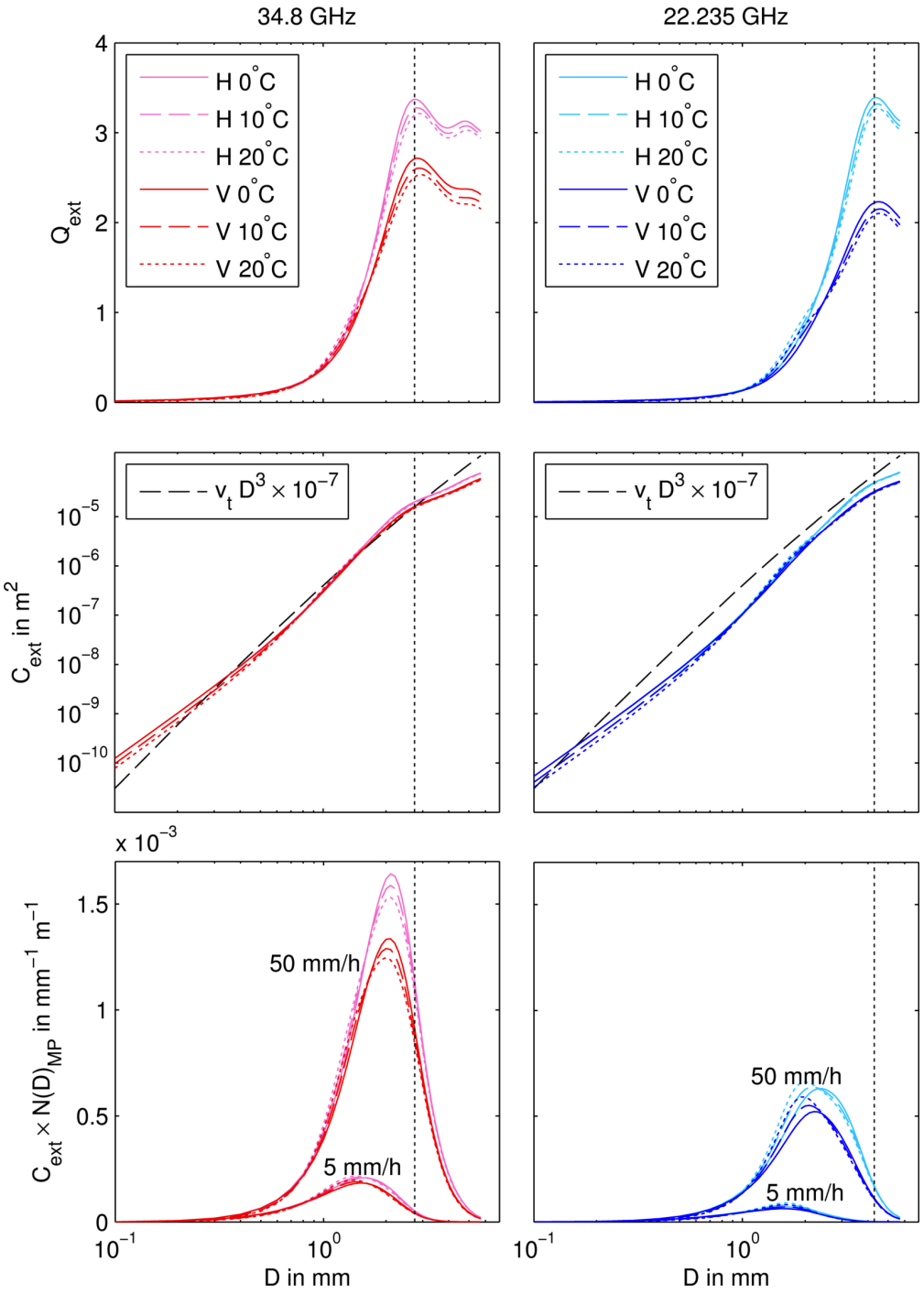

Figure 2.6 – Temperature dependence of the extinction efficiency Q_{ext}, extinction cross section C_{ext} for oblate spheroid shaped drops. The plots are similar to figure 2.5.

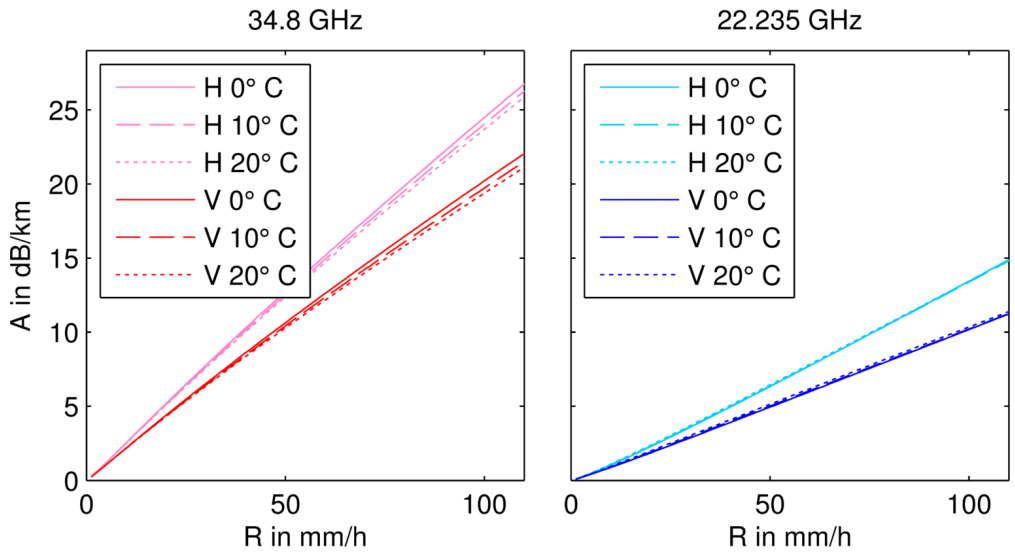

Figure 2.7 – Calculated attenuation A for different rain rates R with varying rain temperature.

With increasing temperature the decreased peak height of $C_{\text{ext}} \cdot N_{\text{MP}}$ for 34.8 GHz (Figure 2.6, lower left) results in a decrease of A. The deviation is still small, though. An increase from 0°C to 20°C only yields a difference smaller than 10%.

For 22.235 GHz the opposing effects of a temperature change at small and large drop diameters, as described above and visible in Figure 2.6, outweigh each other. The deviations between different drop temperatures are negligibly small and hardly visible in the plot.

Dependence of A-R relation on drop size distribution

In the previous subsections the dependence of the scattering characteristics on drop shape and drop temperature have been analyzed, but without changing the DSD. Section 2.1.1, in particular Figure 2.1, however showed that deviations between different theoretical DSD types, which represent different types of rain fall, can be significant. Since the extinction cross-section C_{ext} rapidly increases towards larger drop diameters, it can be expected that different DSD types, hence different numbers of large drops, will have a considerable impact on the overall attenuation A for a given rain rate R.

To examine the effect of the DSD on the A-R relation, Figure 2.8 shows the calculated values of A and R for the theoretical DSD types given in table 2.1. In comparison to the effect of temperature changes, depicted in figure 2.7, the variation of the DSD has a much larger impact on the A-R relation. However, there are certain areas where the DSD dependence seems to be quite small.

For 34.8 GHz and small rain rates $R < 10$ mm/h the deviations between the curves of different DSDs are almost invisible. This is due to the fact that $C_{\text{ext}}(D)$ and $v_t D^3$ have a similar shape at 34.8 GHz for diameters $D < 2.5$ mm. A change of the DSD hence has the same impact on A and R. Thus the DSD dependence is low as long as the contribution of drops with $D > 2.5$ mm is small. That also explains why the curve for JT, which has the highest concentration of large drops of all for DSDs, deviates from the others already at $R \approx 10$ mm/h. For MP, JD and

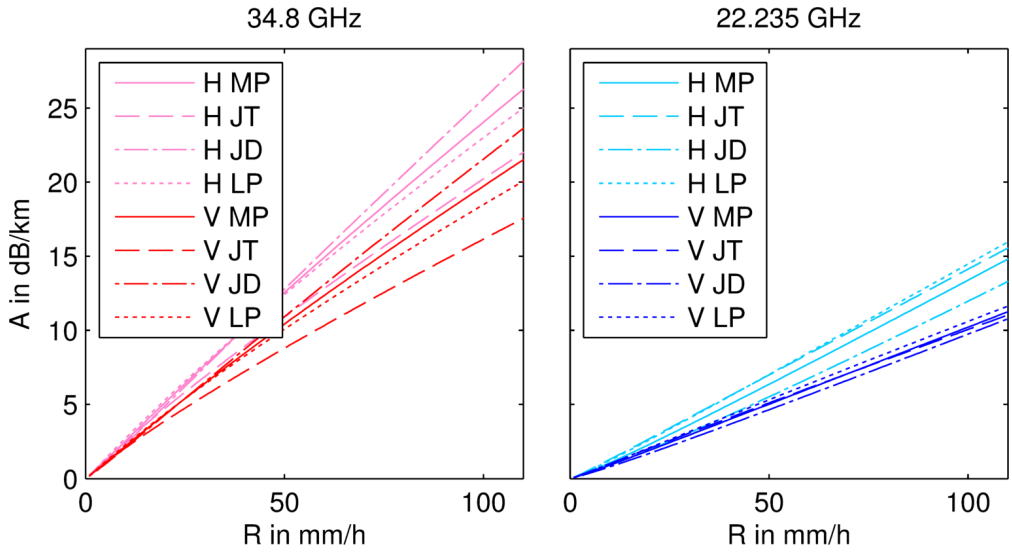

Figure 2.8 – Calculated attenuation A for different rain rates R with varying drop size distributions. The drop size distributions are the theoretical ones listed in table 2.1.

LP the divergence is low up to rain rates $R \approx 30$ mm/h. Above, they also start to diverge.

The behavior at 22.235 GHz is opposite. The difference between the DSDs constantly increases already at small rain rates. For higher rain rates, $R > 50$ mm/h, the divergence however seems to stagnate or even decrease. This can be explained by recalling the relation between $C_{\text{ext}}(D)$ and $v_t D^3$, which differ for small drop sizes but have the same slope for larger drops above the transition from Rayleigh- to Mie scattering at $D_{x=1}$ (see Figure 2.6). That is, the more larger drops are present, the more similar the dependence of A and R on the DSD are at 22.235 GHz. This is in particular true for vertical polarization, where $C_{\text{ext}}(D)$ and $v_t D^3$ have the same slope over a wide drop diameter range from 2 mm to 4 mm. Hence, there is a low divergence of the curves for the four different DSDs at 22.235 GHz in Figure 2.8.

2.1.3 Relation between attenuation A and rain rate R

As can be seen in Figure 2.8 the relation between attenuation A and R is nearly linear with a slight concavity or convexity. Thus, an approximation of the relation between attenuation A in dB/km and rainrate R in mm/h by a simple power law

$$A = a R^b \tag{2.34}$$

seems appropriate. The constants a and b for each frequency will depend on the temperature (see Figure 2.7) and the DSD (Figure 2.8), with the later being the dominant dependence.

Fitting the A-R power law

This dependence of A and R was already recognized during the early days of experimental research on microwave attenuation by precipitation Atlas and Ulbrich [1977]. By fitting equation (2.34) to measured A and R data, or to calculated A and R for theoretical or experimental

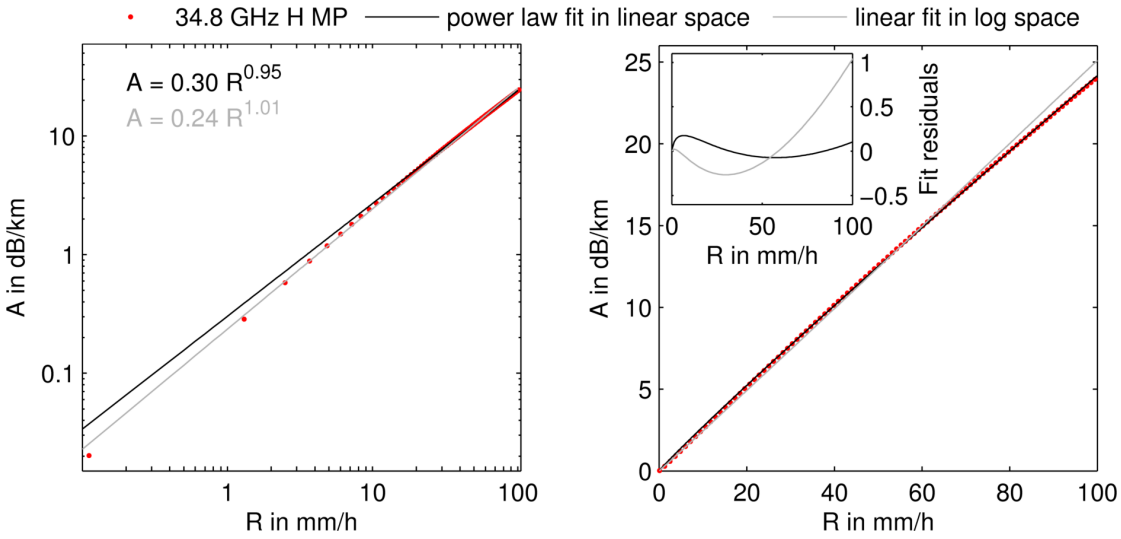

Figure 2.9 – Comparison of linear fit in log space and power law fit in linear space for calculated A and R values at 35 GHz and based on a Marshall-Palmer DSD. The plot on the right shows the data and the two fits in log space. On the right the same is shown in linear space. The fit residuals are plotted in the inset.

DSD data, one easily receives a and b. However, since equation (2.34) is only a approximation, deviations from the original data are inevitable and different fitting methods may yield different results.

This is shown in figure 2.9, where fits of equation (2.34) for rain rates ranging from 0.1 mm/h to 100.1 mm/h in steps of 1 mm/h using a Marshall-Palmer DSD and a temperature of 10°C are presented. The black line represents a non-linear least squares fit of the power law in equation (2.34) whereas the grey line was obtained from a non-linear least square fit in logarithmic space, where equation (2.34) is linear. Since the distribution of the data points differs for the two fitting methods, the results also differ. The linear fit in logarithmic space is governed by the smaller rain rates and hence has the largest residuals at high rain rates (see inset in figure 2.9). In contrast, the power law fit in linear space has a more even distribution of the residuals with a small peak at low rain rates at $R \approx 10$ mm/h. Consequently a and b are also different for the two fits. Their values are given in the top left of Figure 2.9.

It has to be noted that choosing a different range of R or a different distribution of the available data points, will yield different values of a and b even though the underlying DSD type is the same.

Results for different frequencies and different DSDs

From figure 2.8 it is evident that a changing DSD will result in a considerable change of the A-R relation and hence in different fitted values of a and b. Figure 2.10 gives a qualitative overview of the values a and b resulting from the two fit types and the four different theoretical DSD types listed in table 2.1.

For both, a and b, figure 2.10 reveals that there is considerable influence of the DSD type

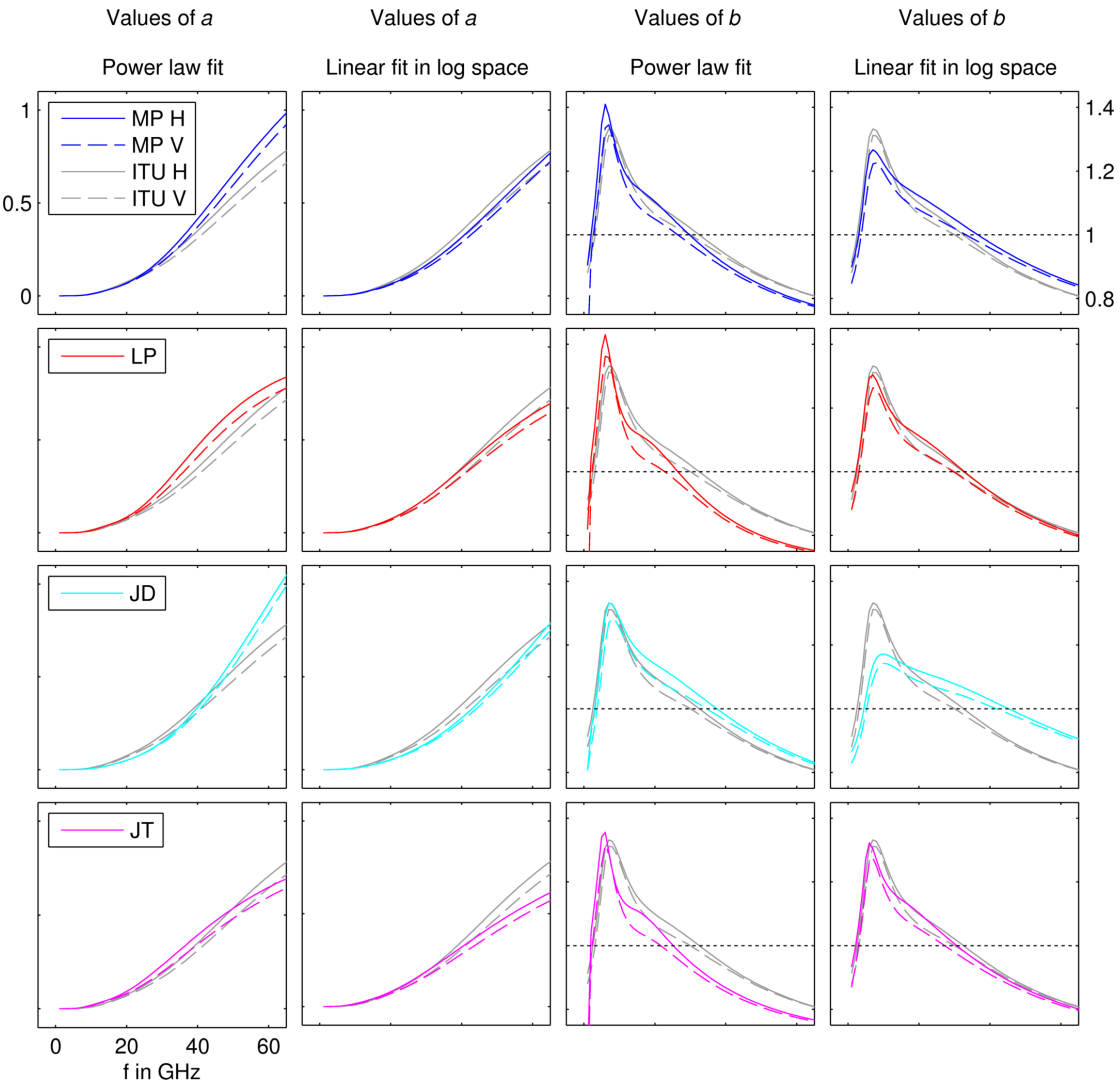

Figure 2.10 – Values for a and b for different theoretical DSDs (listed in table 2.1), obtained by power law fit and linear fit in logarithmic space of the A-R relation in equation (2.34). The calculations were performed with an oblate spheroid drop shape and a temperature of 10°C. As a comparison and to illustrate the differences between the four DSDs easier, the values for a and b recommended by ITU [2003] were added in light grey. The dotted horizontal lines indicate where $b = 1$.

and also from the fit type. The general frequency dependence is, however, following the same pattern. With increasing frequency the value of a is also steadily increasing. Hence the attenuating effect of a certain rain rate, which is mainly governed by the value of a, is also increasing with increasing frequency.

The value of b starts from values slightly below 1 at low frequencies, rises to a peak above 1 at around 10 GHz and then rolls off to below 1 with increasing frequency. The frequency regime where $b \approx 1$ is especially interesting when using attenuation measurements from commercial microwave links to derive rain rates. In this cases the measurements of the line integrated attenuation are used to derive line integrated rain rates using the A-R power law from equation (2.34). A non linearity, here a value of $b \neq 1$, will thus result in an error of the line integrated rain rate $\overline{R}$ since

$$\overline{A} = \frac{1}{L}\int_0^L A(x)\,\mathrm{d}x = \frac{1}{L}\int_0^L aR(x)^b\mathrm{d}x \overset{b\neq 1}{\neq} a\overline{R}^b,$$

where $\overline{A}$ is the measurement of the line integrated attenuation along x over a path length of L. The frequency regime where $b \approx 1$ is between 20 GHz and 40 GHz, depending on the DSD. Hence, it is unfortunately not possible to identify the optimal frequency for line integrated precipitation measurements since the DSD type is constantly changing. Nevertheless, the mean bias and root mean square error for line integrated measurements of rain rates up to path length of 10 km are well below 10% [Leijnse et al., 2008], since the non-linearity in this frequency range is still small, no matter which DSD is chosen.

In each subplot in figure 2.10 the values of a and b recommended by the ITU [2003] are also given as a comparison. They are often used in applications were no knowledge about the DSD data is available. Unfortunately it is not revealed how these recommended values where derived, hence, for which rain fall type the should be most appropriate. Judging by the results in figure 2.10 they seem to resemble the course of the linear fit in log space of the Laws-Parson (LP) DSD, except for frequencies above 40 GHz. That is, the values recommended by the ITU [2003] should be most applicable for typical wide spread rain (Laws-Parson DSD) and small rain rates where the linear fit in logarithmic space has the smallest residuals.

2.1.4 Relation between differential attenuation ΔA and rain rate R

The asymmetry of rain drops, depicted in figure 2.3, leads to different extinction cross sections and hence to a different attenuation for horizontal and vertical polarized microwave radiation (see Figure 2.6 and 2.7). Since the drop asymmetry depends on the drop diameter, which is linked to the rain rate via the DSD, the differential attenuation ΔA is also related to the rain rate R.

An advantage of differential attenuation is the general characteristic of differential measurements to cancel out system inherent biases. Ruf et al. [1996] showed that the long term stability of rain rate measurements with a dual polarization microwave transmission experiment is improved when using ΔA instead of A.

Furthermore, ΔA provides an additional independent measurement of a rain event, com-

plementing the measurement of A. While the derivation of a rain rate R from the sole measurement of A requires the assumption of a certain DSD type (e.g. Marshall-Palmer), the combination of A and ΔA offers the opportunity to estimate a further DSD parameter, e.g. the slope Λ or the shape parameter μ.

In the following, similar to section 2.1.3, the relation between ΔA and R together with their dependence on drop shape, temperature and DSD shall be examined.

Differential extinction cross sections ΔC_{ext}

Using the T-Matrix calculations of the extinction cross section C_{ext} from section 2.1.2, Figure 2.11 shows the differential cross section ΔC_{ext} and ΔQ_{ext}. The differential values are calculated by subtracting the values for vertical polarization minus those for horizontal polarization.

The resulting dependence of ΔQ_{ext} and ΔC_{ext} on the drop diameter is similar to the one of Q_{ext} and C_{ext}, steadily increasing with drop diameter, and with a kink at the transition from Rayleigh- to Mie-scattering (denoted by the dashed vertical line, where the size parameter $x = 1$). The overall magnitude is lower though. Only for very large drops with $D > 5$ mm, ΔC_{ext} almost reaches the value of C_{ext} (see Figure 2.5 for comparison). Hence a smaller sensitivity of the differential attenuation ΔA on R can be expected. Furthermore, in contrast to C_{ext}, ΔC_{ext} is not mimicking the course of $v_t D^3$. That is, ΔA will be more sensitive to wrong assumptions of the DSD. The impact of changing the drop shape from oblate spheroid to generalized Chebyshev has only little effect. Similar for the changes of temperature (not shown here for ΔQ_{ext} and ΔC_{ext}). All following calculations are hence only performed with oblate spheroid shaped drops at 10°C.

DSD dependence of ΔA-R relation

From the difference between ΔC_{ext} and $v_t D^3$ visible in figure 2.11, it can be presumed that there is a considerable dependence of the ΔA-R relation on the DSD. Figure 2.12 confirms this. In contrast to figure 2.8, the course of the different ΔA-R relations for both frequencies exhibit a considerable deviation which already starts at low rain rates $R < 10$ mm/h. At 34.8 GHz the divergence is stagnant with increasing rain rates, which is attributed to the kink of ΔC_{ext} for $D > 2.7$ mm, resulting in a more similar slope of ΔC_{ext} and $v_t D^3$. At 22.235 GHz the slope of ΔC_{ext} does not change till $D > 4.2$ mm. The absolute difference between the ΔA-R relations for the four DSDs is hence increasing with increasing rain rate. On the one hand, this is a limitation when using the ΔA-R relation for rain rate estimation without knowledge of the DSD. On the other hand, the strong dependence on the DSD can also be used for its estimation, if measurements of ΔA are combined with a measurements of A.

Power law fits for the ΔA-R relation

Similar to the A-R relation in equation (2.34), the relation between differential attenuation ΔA in dB/km and rain rate R in mm/h can be approximated by a power law

$$\Delta A = a R^b \tag{2.35}$$

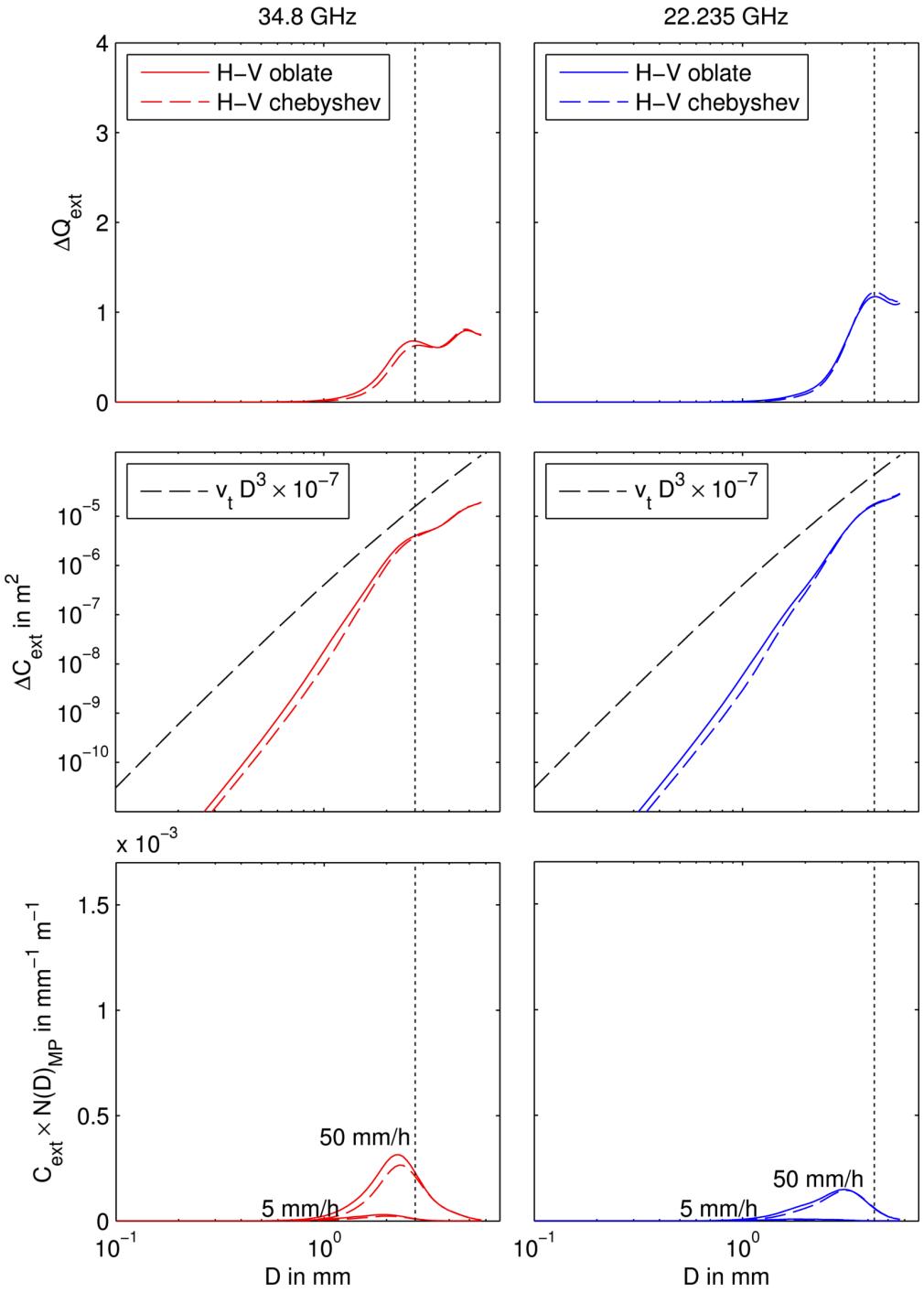

Figure 2.11 – Plots of the results from the T-Matrix calculations for the differential extinction efficiency ΔQ_{ext} and the differential extinction cross section ΔC_{ext} for different rain drop shapes (oblate spheroid and generalized Chebyshev) and the two frequencies used for the experiments in section 3. The plots are similar to figure 2.5 on page 22. The same scaling of the y-axis is used to ease visual comparison.

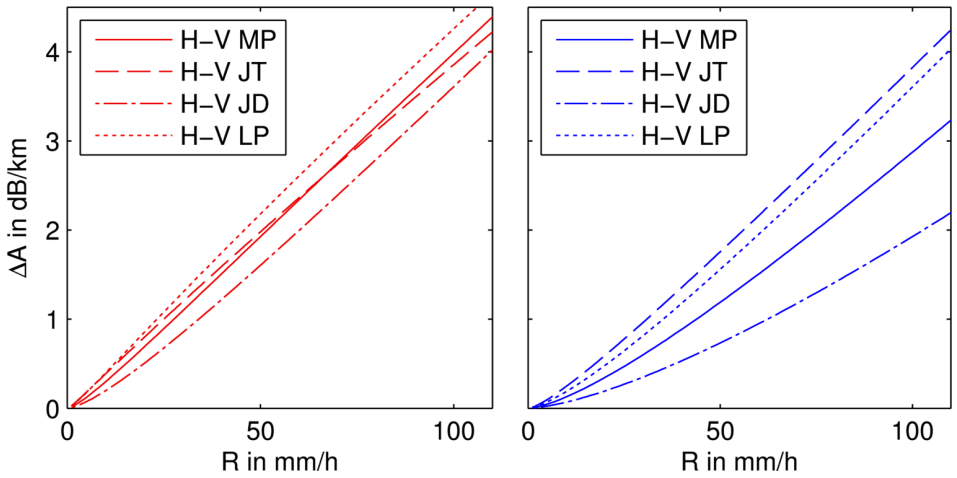

Figure 2.12 – Calculated differential attenuation ΔA for different rain rates R with varying drop size distributions. The drop size distributions are the theoretical ones listed in table 2.1. The plots are similar to figure 2.8, except for the y-axis range, which is lower here to account for the lower sensitivity of ΔA to R.

with a and b depending on the drop shape, temperature, DSD and frequency. Since the drop shape and temperature only play a minor role, they are kept constant for the following analysis. Oblate spheroid shaped drops and a temperature of 10°C are used for the calculations of ΔA.

The results of fitting equation (2.35) to ΔA and R data calculated for the four different DSD listed in table 2.1 are shown in figure 2.13. Like in figure 2.10 two different methods, a power law fit and a linear fit in logarithmic space where performed. The resulting dependence of a and b is also similar to the one of the A-R relation. With increasing frequency a is increasing whereas b has a peak at a frequency of approximately 10 GHz and then decreases towards higher frequencies.

There are, however, significant differences between the power law fits for the A-R relation (see figure 2.10) and the ΔA-R relation. In figure 2.13 the differences between the fitted values of a and b for the four DSDs are more pronounced and start to appear at lower frequencies. Furthermore, the ΔA-R relation exhibits a more pronounced non-linearity, with b reaching values of up to 1.4, in the frequency range from 15 GHz to 35 GHz, which is relevant in this work. This leads to increased errors in the estimation of line integrated rain rates derived from ΔA.

Together with the lower sensitivity of ΔA to R compared to A, it has to be concluded that measurements of differential attenuation are not optimal for rain rate estimation. However, their strong DSD dependence offers the possibility of the estimation of DSD shape parameters, when they are combined with measurements of A.

2.2 Microwave radiation and humidity

Precipitation is not the only source of disturbance for a microwave signal propagating through the earth's atmosphere. Indeed all other atmospheric parameters like gas concentrations,

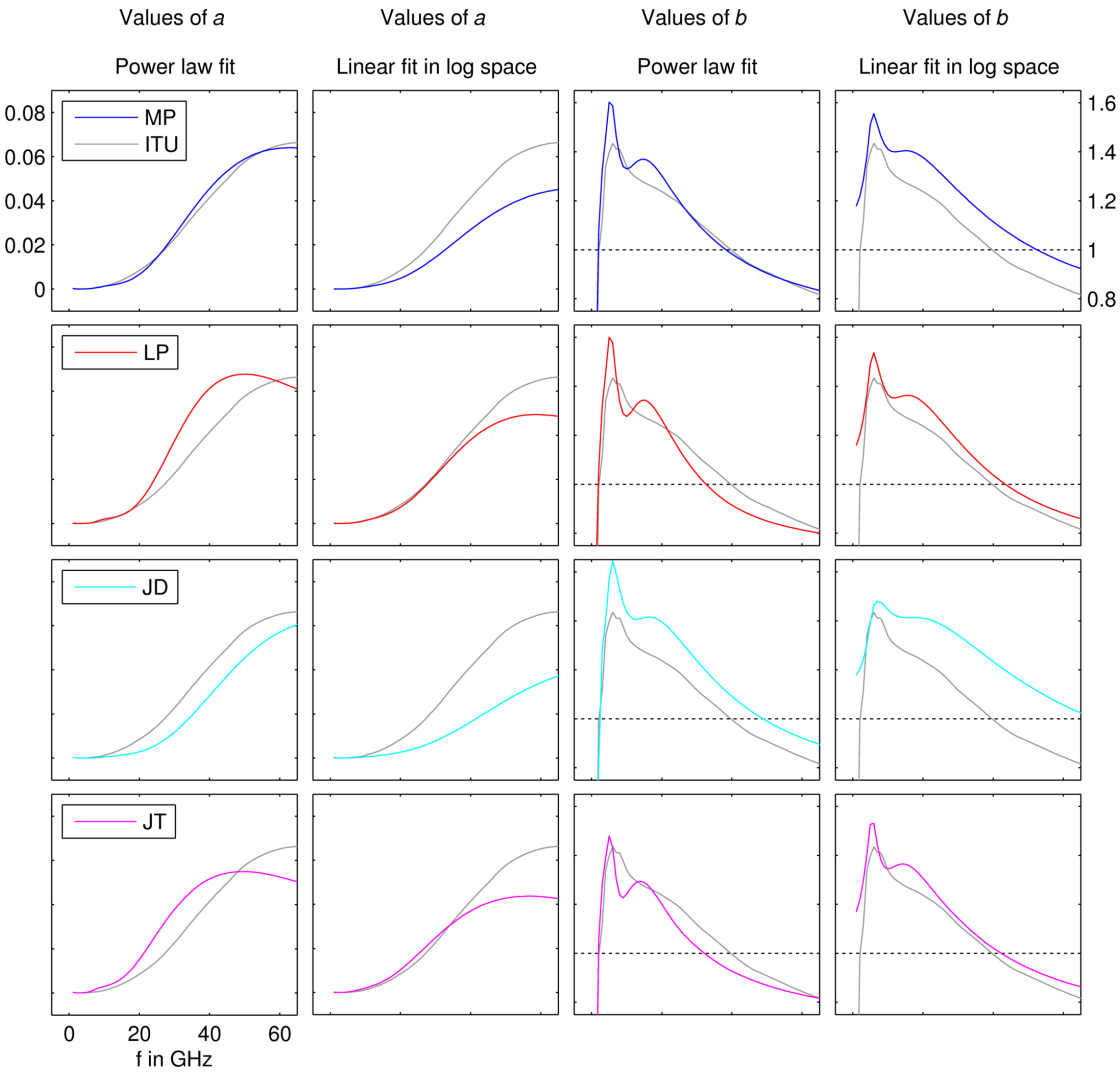

Figure 2.13 – Values for a and b obtained by power law and linear fit in log space of the ΔA-R relation in equation (2.35). The differential attenuation was obtained by subtracting attenuation in vertical polarization from attenuation in horizontal direction. The calculations were performed with oblate spheroid drop shape and a temperature of 10°C. As a comparison and to make illustration of the differences between the four DSDs easier, values for a and b derived from the recommended by ITU [2003] were added in light grey. Theses values were derived by calculating ΔA with the recommend a and b values for horizontal and vertical polarization and performing a power law fit of equation (2.35). The dotted horizontal lines indicate where $b = 1$.

pressure, humidity, temperature and even aerosols [Liebe, 1989] or dust particles [Ho et al., 2004] can cause signal impairment. Of those, humidity is the main contributor. Not only does it attenuate microwave radiation, it also influences the speed of electromagnetic wave propagation and hence causes a phase delay. Measurements of theses disturbances can then be used to estimate the humidity changes that caused them.

2.2.1 Properties of humidity

The term *humidity* refers to the amount of water vapor in the air. More precisely, it is the fraction that water vapor contributes to the mixture of gases in the earth's atmosphere. That is, it is not the air, holding the water vapor, but rather is air a mixture of gases of which one is water vapor.

Commonly, humidity is quantified as absolute humidity q or as relative humidity RH. Absolute humidity is defined as the mass of water vapor m_{w} within a certain volume V by

$$q = \frac{m_{\mathrm{w}}}{V} \tag{2.36}$$

with the most common units being g/m^3. Relative humidity RH given in % is defined as

$$RH = 100\% \times \frac{p_{\mathrm{v}}}{p_{\mathrm{v,sat}}} \tag{2.37}$$

where p_{v} is the actual water vapor pressure and $p_{\mathrm{v,sat}}$ is the saturation water vapor pressure. At 100% when $p_{\mathrm{v}} = p_{\mathrm{v,sat}}$, saturation is reached and water vapor starts to condense. The saturation water vapor pressure $p_{\mathrm{v,sat}}$ in mbar is a function of temperature and can be approximated by

$$p_{\mathrm{v,sat}} = 6.112 \exp\left(\frac{17.67\,T}{T+243.5}\right) \tag{2.38}$$

where T is in °C [Bolton, 1980]. Absolute humidity q can be derived from water vapor pressure p_{v} via the equation

$$q = \frac{p_{\mathrm{v}}\,M}{R_G\,(T+273.15)} \tag{2.39}$$

where $M = 18.02$ g mol^{-1} is the molar weight of water and $R_G = 8.3144621 \times 10^{-2}$ mbar m^3 mol^{-1} K^{-1} is the gas constant.

Most modern weather stations measure RH directly. This is achieved by measuring changing electrical properties (capacity or resistance) of a hygroscopic sensor. Since microwave attenuation and phase delay are directly related to the actual water vapor content in the atmosphere, which is represented by the absolute humidity, RH has to be transformed to q. For a given air temperature T this is achieved by calculating the absolute humidity at saturation level q_{sat} using equation (2.39) and (2.38), which then can be scaled with RH in % via

$$q = \frac{RH}{100}\,q_{\mathrm{sat}}. \tag{2.40}$$

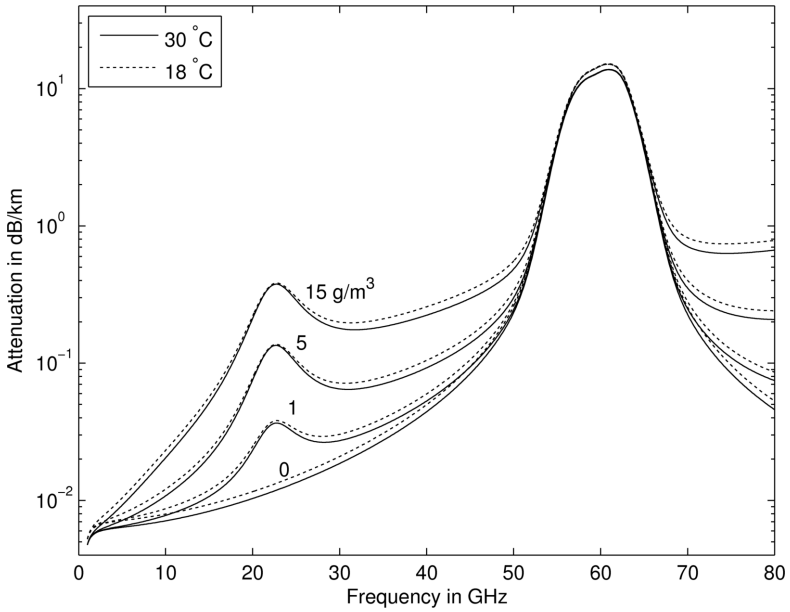

Figure 2.14 – Frequency dependence of microwave attenuation due to dry air and water vapor for different temperatures and different water vapor contents.

2.2.2 Attenuation by water vapor

The attenuation A_q caused by water vapor in the microwave regime is governed by a water vapor resonance line at 22.235 GHz. The exact values of A_q can be calculated using the semi-empirical formulation for the millimeter wave propagation model (MPM) developed by Liebe et al. [1993]. Results for different values of absolute humidity q over the frequency range from 1 GHz to 80 GHz are shown in figure 2.14. As expected, there is a strong effect of the water vapor concentration at 22.235 GHz. This effect decreases when moving away from 22.235 GHz, but is still present throughout the frequency band in which commercial microwave links operate (10 GHz to 40 GHz). Since MPM also considers the attenuating effect of the dry atmosphere, which is dominated by the oxygen resonance lines around 60 GHz, there is a prominent peak unaffected by water vapor in this frequency range. The overall temperature dependence of the attenuation caused by wet and dry air is low.

The low temperature dependence and the dependence on air pressure are shown in figure 2.15 in more detail for the two frequencies that are used in the transmission experiment in chapter 3. Interestingly, increasing the pressure has opposite effects at the two frequencies. At 22.235 GHz is leads to a decrease of the attenuation. At 34.8 GHz the attenuating effect is increased. This is due the pressure broadening of the water vapor absorption line. Increased pressure broadens the absorption peak, hence the increase at 34.8 GHz. But at the same time the peak value exactly at the absorption line frequency decreases.

As expected from figure 2.14 the attenuating effect of water vapor is stronger at 22.235 GHz, approximately twice the effect at 34.8 GHz. It is also almost linear. This makes 22.235 GHz

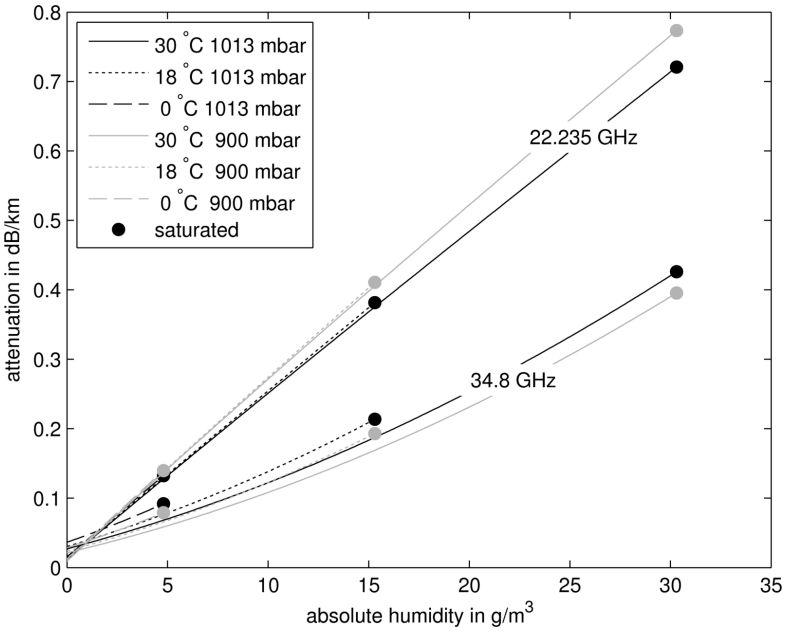

Figure 2.15 – Dependence of the attenuation on water vapor content for the two frequencies used for the experiments in chapter 3 (22.235 GHz and 34.8 GHz). Different combinations of air pressure and air temperature are used. The dots indicate where saturation is reached and relative humidity equals 100%.

the optimal frequency to derive absolute humidity values from attenuation measurements. At this frequency the relation between absolute humidity in g/m^3 and the attenuation A_q in dB/km can be approximated by

$$q = (-1.6 \times 10^{-5} P + 0.0396)^{-1} (A_q - 0.015) \tag{2.41}$$

with P being air pressure in mbar. This approximation was derived by a least square fit of the $q(P, A_q)$ plain and is within 3% deviation of the original relation for values of P ranging from 900 mbar to 1000 mbar and T ranging from -10°C to 30 °C. The approximation neglects any temperature dependency because it is marginal in the region of interest in this work. At a typical pressure P of 950 mbar, which is a good average at the test site of the experiment presented in chapter 3, equation (2.41) results in

$$q \approx \frac{1}{0.024} (A_q - 0.015) \tag{2.42}$$

yielding an attenuation change of 0.024 dB/km for a change of q by 1 g/m^3.

2.2.3 Phase delay due to water vapor

For path length of only few kilometers the attenuation caused by water vapor will be small, i.e. smaller than 1 dB. Thus it could easily be superimposed by fluctuations stemming from other sources (e.g. mechanical deflection of antennas, temperature drifts) or would not

reach the detection limits of measurement systems (determined by the electronics' noise and the quantization of the recorded data). A more sensitive way to retrieve absolute humidity information is to use measurements of phase delay, where available. Phase delay is linearly related to the speed of propagation determined by the refractive index n, which in turn depends mainly on atmospheric pressure, temperature and humidity.

A change of the phase angle $\Delta\phi$ is related to a change of the refractive index Δn by the equation

$$\Delta\phi = \frac{2\pi f r}{c}\Delta n \tag{2.43}$$

with f being the frequency in GHz, r the path length in m, and c the speed of light in vacuum. In case of electromagnetic wave propagation through the atmosphere, deviations of the refractive index from 1 are very small. Hence the refractivity

$$N = (n-1)\times 10^6 \tag{2.44}$$

is defined as a magnification of this deviation, which, using equation (2.43), can be written as

$$N = N_0 + 10^6 \times \frac{\Delta\phi\, c}{2\pi f r} \tag{2.45}$$

with an initial refractivity N_0.

Following Bean and Dutton [1968] effects of atmospheric changes are related to refractivity with

$$N = 77.6\frac{P}{T_k} + 3.73\times 10^5 \frac{e}{T_k^2} \tag{2.46}$$

where P is the pressure in mbar, T_k the temperature in K and e the water vapor pressure in mbar. Using the relation for water vapor pressure

$$e = \frac{q\, T_k\, R_G}{M} \tag{2.47}$$

equation (2.46) can be write as

$$N = 77.6\frac{P}{T_k} + 3.73\times 10^5 \frac{q\, R_G}{T_k\, M} \tag{2.48}$$

with the gas constant $R_G = 8.314\times 10^{-2}\,\mathrm{mbar\,m^3\,mol^{-1}\,K^{-1}}$ and the molar weight of water $M = 18.02\,\mathrm{g\,mol^{-1}}$. The resulting dependence of N on q and T is illustrated in Figure 2.16. Changes in P are not considered in the plot, because they are negligible for the common pressure ranges of 900 to 1000 mbar.

It indicates that the impact of changes in absolute humidity by 1 g/m^3 is around six times larger than the impact of a temperature change by 1°C. It is noted though, that during cold weather, when water vapor saturation is already reached at low absolute humidity values, e.g.

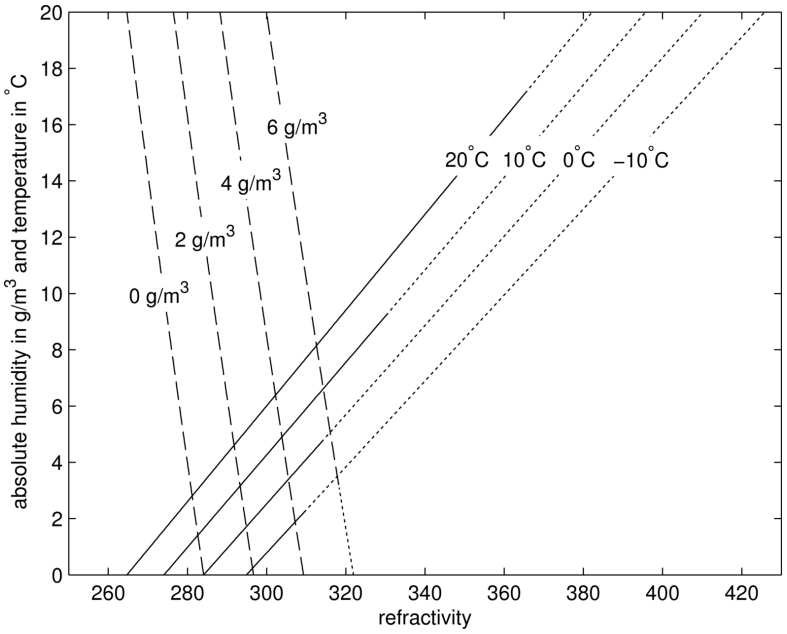

Figure 2.16 – Relation of refractivity N to values of absolute humidity and temperature. The dotted lines indicate where relative humidity exceeds 100 %

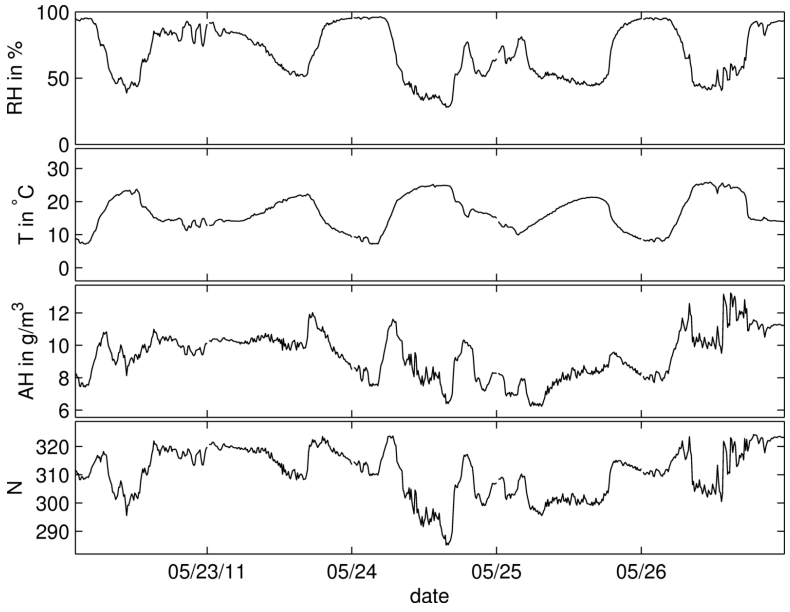

Figure 2.17 – Example of refractivity N time series calculated from temperature T, absolute humidity AH and pressure P (not shown) recorded by the weather station described in section 3.3

≈ 2 g/m^3 at -10°C, the magnitude of temperature changes can easily outreach the changes by absolute humidity. Whereas during warm weather conditions with absolute humidity reaching high values, e.g. $\approx 30 \frac{\mathrm{g}}{\mathrm{m}^3}$ at 30°C, N is mainly governed by absolute humidity.

Figure 2.17 gives an example for warm weather conditions during end of May 2011. The course of the calculated refractivity, in particular the fluctuations on short time scales, mimic the course of the values of absolute humidity. Furthermore , it can also be seen, that temperature is a more continuous quantity than humidity. Accordingly temperature can be assumed to change less over space and time, because its sinks and sources are affected less by the heterogeneity of the ground. Therefore, it can be concluded that it is reasonable to interpolate point measurements of T to correct the calculation of absolute humidity retrieved by means of phase delay measurements along a path of several kilometers.

3 Rainfall and humidity observation using a monostatic microwave transmission experiment

Experience is the past tense of experiment.
— Gregory Alan Elliot

This chapter introduces the monostatic dual frequency dual polarization device which was developed and built up during the course of this PhD thesis. In the following, the basic reasoning behind the chosen concept is presented together with its technical implementation. Finally results from the first operational phase are analyzed.

The chapter is based on the article entitled "A monostatic microwave transmission experiment for line integrated precipitation and humidity remote sensing" that appeared in the special issue *Perspectives of Precipitation Science* of *Atmospheric Research* [Chwala et al., 2014].

3.1 From the basic idea to a feasible concept

Commercial microwave links were not designed to be measurement devices. Hence, even though the exploitation of their attenuation data is a promising new technique for precipitation remote sensing, they are not well suited for studying the underlying effects in detail. This is why a purpose built microwave transmission device should accompany the research with commercial microwave links within the PROCEMA project (section 1.1.4). Its capabilities should, however, not be limited to attenuation measurements, since building up an own experiment from scratch offers the possibility to add further options to study effects that are less or not at all investigated. In the following section the planning process from the basic requirements to a feasible concept is presented.

3.1.1 Requirements

First of all, the experiment's results should be comparable to results obtained with commercial microwave links. Hence the chosen frequency has to lie in the same range, between 15 GHz and 40 GHz. For a better coverage of this wide band and for making a comparisons between different frequencies possible, at least two frequencies are desired.

Furthermore, the experiment should be able to measure attenuation with horizontal and vertical polarization. This enables differential measurements of rain rate, because of the oblate shape of rain drops. Furthermore this offers the potential to study the effect of the DSD on rain rate estimates derived from attenuation measurements (see section 2.1.4).

Besides the attenuation measurements for precipitation estimation the system should provide phase delay measurements to derive humidity information. A high phase stability of the system is hence required, to be able to identify phase variations that stem from changes in the atmosphere.

It should also allow for the experimental study of Doppler induced fluctuations of the transmitted signal, which are also investigated within PROCEMA using electromagnetic simulations. To be able to resolve these fluctuations the sampling frequency has to be a high enough. Since the exact upper limit for the frequency of these fluctuations was not clear from the beginning, it was decided to use the highest sampling frequency that can be easily implemented with standard hardware. That is, the targeted sampling frequency should be in the kHz range.

The path length for which the system should be optimized was also a further crucial parameter. It determines the overall path integrated attenuation that will be caused by a certain rain rate. The longer the path, the larger the attenuation and hence the sensitivity of the system to rain rate. However, a longer path increases the probability of changes in rain rate, DSD or even precipitation type along the path. Choosing the right path length is hence a trade-off. With a desired lower detection limit of 0.1 mm/h, which equals approximately 0.01 dB/km at 25 GHz, it was decided that a minimum of 1 km path length is required to make the detection of the lower rain rates feasible.

Summed up the requirement specifications for the transmission experiment were the following:

- operating at two frequencies between 15 GHz and 40 GHz
- polarization agile
- high phase stability
- sampling frequency in the kHz range
- path length of approximately 1 km

3.1.2 Concept

The selection of the two frequencies can be carried out based on the theoretical relations between microwave radiation, precipitation and humidity as described in chapter 2. With the higher frequencies being more sensitive to rain induced attenuation and a nearly linear A-R relation (see section 2.1.3) around 30 GHz, one frequency is chosen to be at 35 GHz. The second frequency is located at 22.235 GHz, where the attenuation from water vapor is large due to the water vapor absorption line (see section 2.2.2).

To keep the instrument as compact as possible it was decided that only one antenna should be used for both polarizations. A ferrite polarizer attached to the antenna would then provide the opportunity to switch between horizontal and vertical polarization. To further simplify the design, it was planed to supply the HF hardware for both frequencies from one source

and operate them simultaneously. Cross-talk could be assumed to be very low because the frequencies are separated by several GHz and the receiver stages would have narrow enough filters.

The requirement that turned out to be most critical was the high phase stability. Usual microwave transmission setups have transmitter and receiver separated spatially. As consequence they have two separated frequency sources which serve as reference for the high frequency hardware. Both references are subject to drifts, hence the phase between transmitter and receiver is also constantly drifting. Synchronization of the two references would have been technically possible - using fiber optics or a transmitted synchronization beacon - but very expensive. Fortunately, different to common microwave transmission setups which have to transmit information, our system has the sole purpose of studying the atmospheric impacts on microwave propagation. Thus it does not necessarily need to have a bistatic configuration with transmitter and receiver at two separate locations. A monostatic setup (see figure 3.1), where transmitter and receiver are at the same location and share the same signal source, is hence also an option.

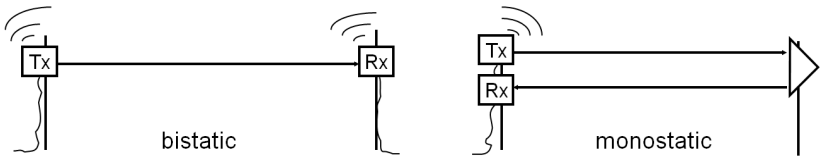

Figure 3.1 – Schematic of a monostatic and bistatic configuration illustrating the need for power supply and internet connectivity of the active elements (transmitter = Tx and receiver = Rx)

The monostatic setup uses a trihedral corner reflector to scatter back the transmitted radiation. This way the problem with the phase stability due to the two drifting references could be solved and in addition distribution in the field gets easier because there is only one active element which needs power supply and internet connection. But new problems arise with the choice of a monostatic configuration.

As already observed by Ruf et al. [1996] the backscatter from a rain field into the receiver stage superimposes the backscatter from the trihedral reflector. But only the later is the desired transmitted signal over the whole path length. To overcome this problem, the transmitter and receiver were equipped with switches to allow for a pulsed operation. The receiver only opens when the transmitted pulse arrives back from the reflector after its round trip time. With our planed one way path length of around one kilometer this round trip time is at most 7 μs. The so called two way echo, the backscatter from the place at exactly twice the distance than the reflector, then has a round trip time of 14 μs. That marks the upper limit of the pulse repetition rate (PRF) because it is recommended to wait with transmitting the next pulse till the two way echo has passed the receiver.

The maximum PRF of $\frac{1}{14\mu s}$ = 70 kHz also sets the limit of maximum sampling rate of the system. To answer the question if this is enough, a rough estimation of the noise bandwidth can be done by looking at the expected Doppler frequencies. A rain drop falling at 10 m/s will

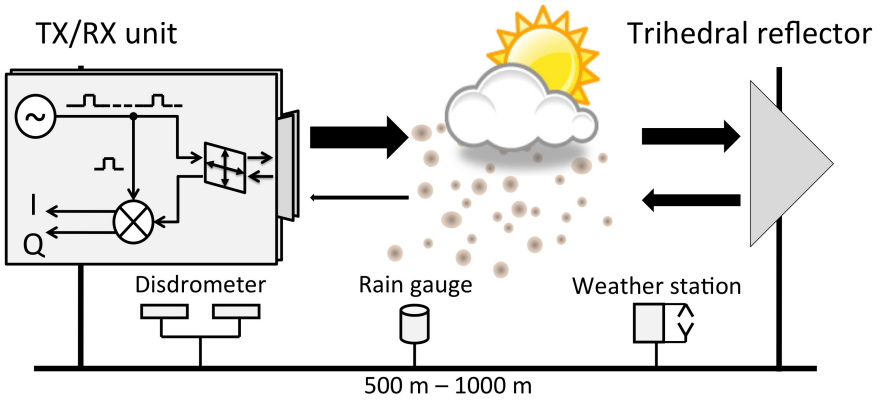

Figure 3.2 – A schematic of the final concept for the transmission experiment.

cause a Doppler shift of approximately 1.2 kHz for a 35 GHz wave. Hence, even if the drops are moved horizontally by very strong winds (> 50 m/s) a bandwidth of 10 kHz will be more than sufficient.

The final concept, that was agreed upon after all discussions with experts from the *Institute for High-Frequency Engineering* of the *Technische Universität München* and the high frequency component suppliers, is shown in Figure 3.2. Its main features consisted of the following points:

- a monostatic setup using a trihedral reflector at 500 m to 1000 m distance (two-way path length between 1000 m and 2000 m)
- two simultaneously operating systems with frequencies (35 GHz and 22.235 GHz)
- one antenna for each frequency
- one ferrite polarizer for each frequency
- a pulsed transmitter and receiver for range gating
- a sampling rate of 10 kHz for each polarization
- a PRF at the sampling rate

3.1.3 Power budget planning

After setting the main parameters, frequency and path length, the next step is to plan the power budget which determines the choice of the high frequency components.

The most important factor is the desired received power P_r of the system during clear sky conditions, which depends on the system's noise floor and the desired dynamic range. The noise floor is determined by the thermal noise, inherent to all electronic systems, and the system noise figure, which is the sum of the noise all the installed electronic components exhibit. With a sampling rate and hence a bandwidth B of 10×10^3 Hz, the system thermal noise

$$P_{\text{thermalnoise}} = k_b T_k B \tag{3.1}$$

equals $P_{\text{thermalnoise}}$=-133 dBm for a temperature of T_k=300 K, with $k_b = 1.381 \times 10^{-23}$ being

the Boltzmann constant in J/K. The desired dynamic range is set to 40 dB, the approximate attenuation which is caused by a rain rate of 100 mm/h over a path of 2 km length at a frequency of 35 GHz (see Figure 2.8). With an assumed system noise figure of NF=10 dB, this yields a required minimum received power of P_r= -80 dBm in clear sky conditions.

Based on the required P_r= -80 dBm = 1×10^{-8} mW the remaining system parameters can be defined according to the monostatic radar equation

$$P_r = \frac{P_t G^2 \lambda^2 \sigma}{(4\pi)^3 r^4 L} \tag{3.2}$$

where P_t is the transmission power in mW, G is the antenna gain, λ is the wavelength in m, σ is the radar cross section of the trihedral reflector in m^2, r is the one-way path length in m and L is the system loss. With the trihedral radar cross section

$$\sigma = \frac{4\pi l^4}{3\lambda^2} \tag{3.3}$$

equation (3.2) can be written as

$$P_r = \frac{P_t G^2 l^4}{3(4\pi)^2 r^4 L} \tag{3.4}$$

where l is the inner length of the trihedral reflector in m. A schematic of the power budget according to the monostatic radar equation is shown in Figure 3.3.

Hitherto the requirements fix only three parameters, i.e. the received signal level in clear sky $P_r = 1 \times 10^{-8}$ mW, the maximum range r = 1000 m and an assumed system loss factor of L = 10. That is, there is an unlimited combination for P_t, G and l that satisfy equation (3.4). Availability, price and mechanical stability do however constrain these combinations. Typically P_t is in the range of 100 mW for of the shelf amplifiers. Antenna gain G increases with the antenna size and with decreasing wavelength. In the desired frequency range of around 30 GHz and maximum antenna diameter of 25 cm, G is at maximum 1×10^4. Furthermore, the maximum size of a trihedral reflector that could be built in the mechanical workshop of the *Institute for High-Frequency Engineering* at the *Technische Universität München*, was l = 0.7.

Bringing all this constraints together, equation (3.4) yields $P_r \approx$ -75 dBm for P_t = 100 mW, $G = 2 \times 10^3$ and l = 0.7 m. That is, with this choice of feasible parameters, there is even a small safety margin of 5 dB compared to the minimal desired signal level in clear sky P_r = 80 dBm.

3.1.4 Site identification and construction work

With the concept finished, the next step is the search for an appropriate test site which would allow a 500 m to 1000 m one-way path length and which would provide power supply and internet at least at one end of the path. The search was focused on the Ammer catchment in southern Bavaria, since it is one of the major test regions for the research carried out at the *Institute of Meteorology and Climate Research, IMK-IFU*. A further constraint is the complexity of the terrain and vegetation. For the first installation of the experiment, a flat test site with low vegetation was desired.

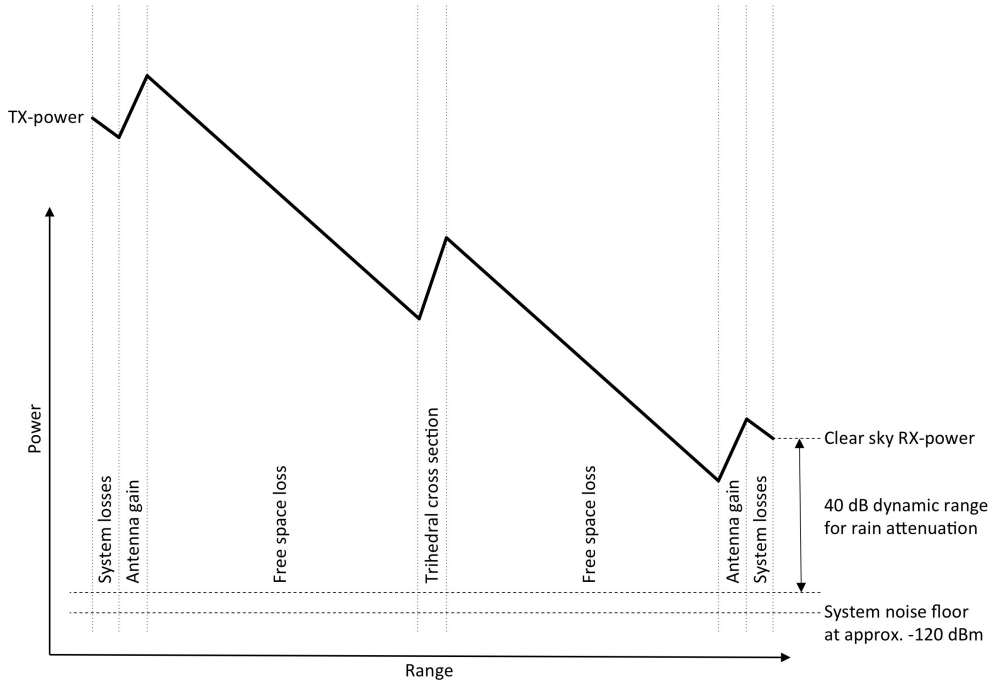

Figure 3.3 – Illustration of the power margin planing. Note that the axes are not true to scale and are both logarithmic.

After several examinations of potential test sites the challenge was not to find a flat meadow of around 1 km extent, but to find a farmer who is willing to let one build concrete baseplates for the two towers on his land and who does not care about a radiating microwave device on his property. Eventually, after an attempt at the *DLR* ground stations *Lichtenau* which failed due to concerns of interference of the experiment with the X- and Ku-band satellite communication, an appropriate test site was found at an discontinued glider airfield at *Fendt* near the cities of Weilheim and Peissenberg.

For the operation of the experiment two 10 m towers were installed at the test site. The concrete baseplate was built by an engineering company while the set up of the towers was carried out jointly with colleagues and a small crane, shown in Figure 3.4. The necessary power supply and internet connection was organized together with the institutes IT department. Fortunately, almost immediately after discovering the Fendt test site, it was expanded to a TERENO test site, which brought with it the advantage of a much larger data traffic and power supply capacity. The details of the installed equipment will be explained in section 3.3.

3.2 Final system details

According to the final concept (section 3.1.2) and the power budget planing (section 3.1.3) the exact layout of the HF hardware was defined together with the HF hardware supplier *PARZICH GmbH Mikrowellen-Technik* and *Innovative Technical Systems, Inc.*. In the following the resulting HF system together with its data acquisition and controls system are presented.

Figure 3.4 – Picture of installation work at the TERENO test site *Fendt*.

3.2.1 High frequency system

The layout of the HF system are similar for both frequencies. They share the a 100MHz crystal oscillator as reference source and operate simultaneously. The reference synchronizes a phase locked oscillator (PLO), whose output is converted up and split into the upper and lower sideband. These are then multiplied to provide the HF output and the reference signal for down conversion in the receiver stage. The multiplier provides an output power of ≈ 20 dBm. The PIN switch used for pulse generation is situated before the multipliers to preserve better isolation. To keep the system as compact as possible only one horn lens antenna per frequency, each with an aperture of 23 cm, is used for both transmission and reception. Polarization is altered by a ferrite polarizer. The transmitter (Tx) and receiver (Rx) chain are connected via a ferrite circulator and two additional PIN-switches to the antenna to optimize isolation of the Tx from the Rx unit. The aforementioned lower sideband is used in Rx to down convert the output of the receiver low-noise amplifier (LNA), which is subsequently downconverted by an I/Q mixer to provide the baseband I/Q outputs. Figure 3.5 shows a simplified block diagram

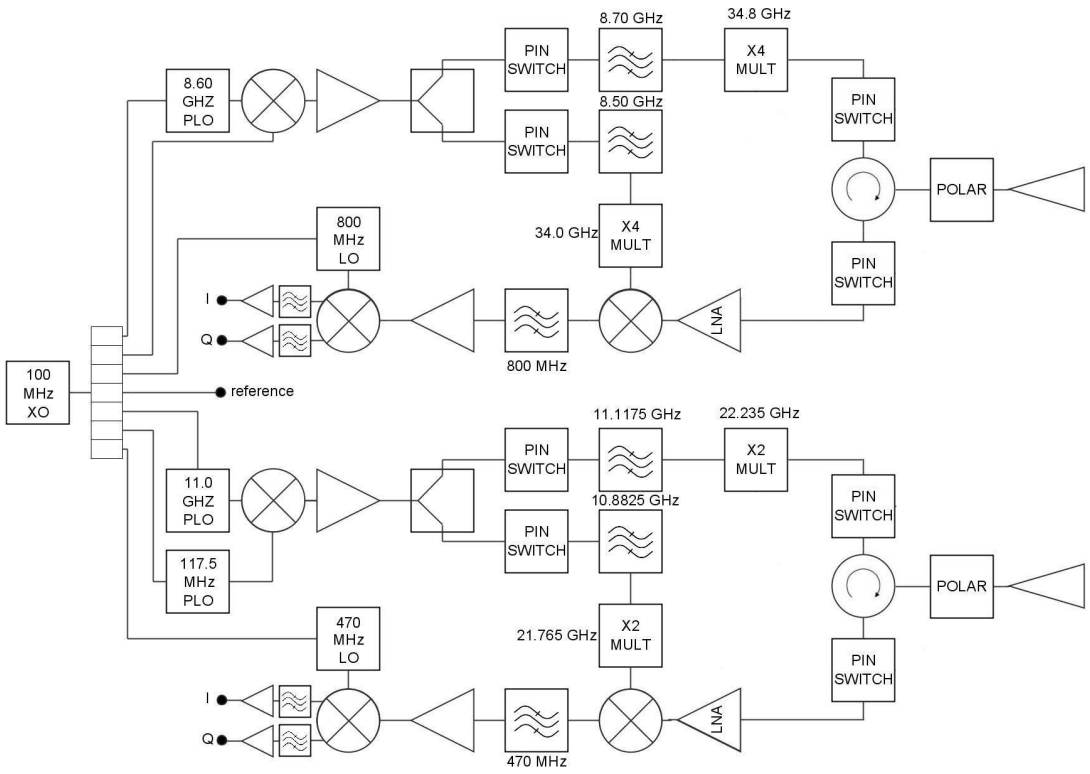

Figure 3.5 – Block diagram of the HF components

for the complete microwave system.

The system's pulse repetition frequency (PRF) is fundamentally determined by the total path length. To exclude two way echoes, the pulse repetition time (PRT) should to be at least twice the round trip time of a pulse reflected by the reflector. With the trihedral reflector at a distance of 660m we thus have to use a PRF < 100kHz. A further constraint of the system's PRF is the settling time of the ferrite polarizers. It is of importance, because the system operates with alternating polarizations to perform quasi-simultaneous measurements for both polarizations. The high inductance of the polarizer coils of several mH results in a settling time between 20 µs and 35 µs until reaching a stable cross-polarization state (time may differ depending on polarizer and polarization state). A save PRT thus is 40 µs. Hence, the system's standard PRF is set to 25 kHz. An overview of the basic system operating characteristics is given in Table 3.1.

3.2.2 Data acquisition and control system

To keep the instrument enclosure as small as possible the timing generator and data acquisition (DAQ) system were tailored to the needs of the experiment. The basic concept is depicted in Figure 3.6.

An embedded Linux operating system running on a small singleboard computer (SBC)

	34.8 GHz	22.235 GHz
Antenna gain	36 dBi	32 dBi
3 dB beam width	2.4	4.2
Trihedral RCS	41 dBsm	36 dBsm
Tx power	18 dBm	16 dBm
Noise figure	10 dB	8 dB
PRF	25 kHz	25 kHz
Polarizer settling time	35 µs	35 µs
Pulse width	min 100 ns	min 100 ns
Two-way path length	1320 m	1320 m

Table 3.1 – System operating characteristics

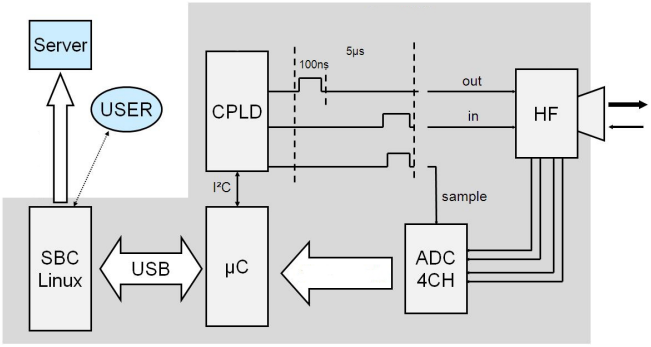

Figure 3.6 – Schematic of the data acquisition and control system.

provides a user interface via SSH remote login and also handles the data transfer to a database server. Via High Speed USB, the SBC connects to a micro-controller (µC) on a printed circuit board (PCB) holding all other components of the control-system.

On the PCB, the µC interfaces an ADC via a parallel bus and has an I2C-bus (a two wire serial bus) to connect to thermostats for the heating control and a complex programmable logic device (CPLD) which generates the pulses controlling the Tx and Rx switches. The ADC simultaneously samples four channels (I and Q for both frequencies) with a 12 bit resolution and passes the data on to the µC which continuously streams it to the SBC with a transfer rate of 1.2 MBit/s for a PRF of 25 kHz. The track & hold of the ADC is triggered by the pulse generator running on the CPLD controlling the switches of the HF system. Pulse width, delay for the receiver stage and PRF can be chosen and altered in 10 ns steps. The minimal values for pulse width, however, are determined by the rise and fall time of the switches.

The PCB is an own design, shown in Figure 3.7. Etching was done by a specialized company, but all soldering and component placement was done by self-dependent. The software running on the SBC, the µC and the CLPD are also own developments.

The timing control system allows different modes of operation. All data used in this work was acquired using the averaging mode with a pulse width of 200 ns. The averaging mode takes 32 continuous samples of the raw I and Q data sampled at 25 kHz and stores their average. This is done continuously each 50 ms, resulting in a sampling rate of 20 Hz. In this mode

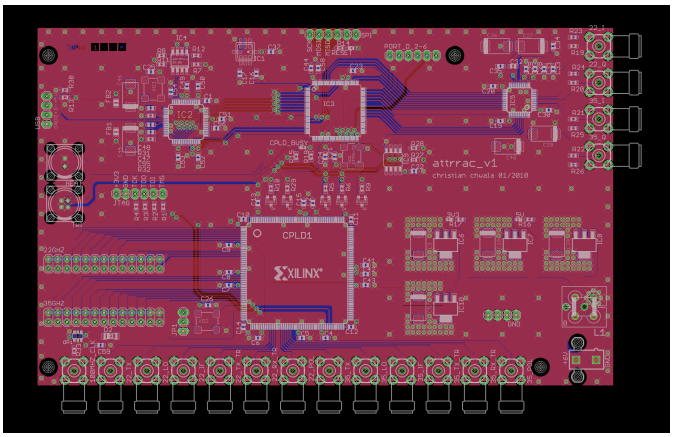

Figure 3.7 – The PCB layout of the DAQ system showing top layer (red), bottom layer (blue) and all ICs, vias, resistors and capacitors. The power supply and ground layer are not shown.

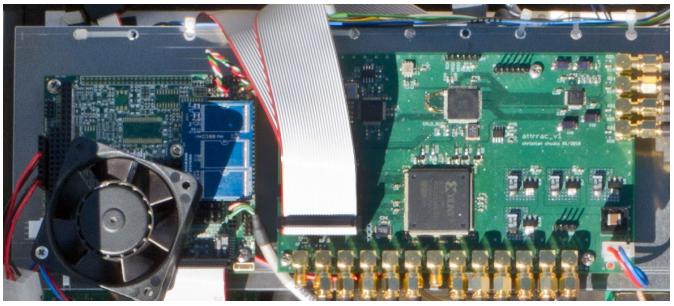

Figure 3.8 – Photo of the final data acquisition system consisting of the single-board computer (on the left side, half covered by the fan) and the custom PCB generating the pulses for controlling transmitter and receiver and recording the I and Q outputs of the high frequency system.

the accuracy of the received signal amplitude measurements is 0.1 dB for both frequencies and both polarization. However, attenuation measurements in the field are subject to larger fluctuations (up to 1 dB) due to tower movement and changing ground reflection properties.

3.3 Test site setup

The system is installed at the TERENO pre-alpine hydrometeorological test site in Fendt (47°49'59"N, 11°03'40"E, 600 m a.s.l.), about 50 km south of Munich, Germany. The mean annual precipitation is approximately 1100 mm, with a maximum of 200 mm per month observed in June and July. Mean annual temperature is around 8°C, with high likeliness of snow fall during the winter months. An overview of the test site with detailed locations of all devices is displayed in Figure 3.9.

3.3.1 Laser Disdrometer

At the site, a *Thies* Laser Disdrometer mounted at the Tx/Rx tower 10 m above the ground provides minute resolution drop diameter and drop velocity data. To discriminate the different

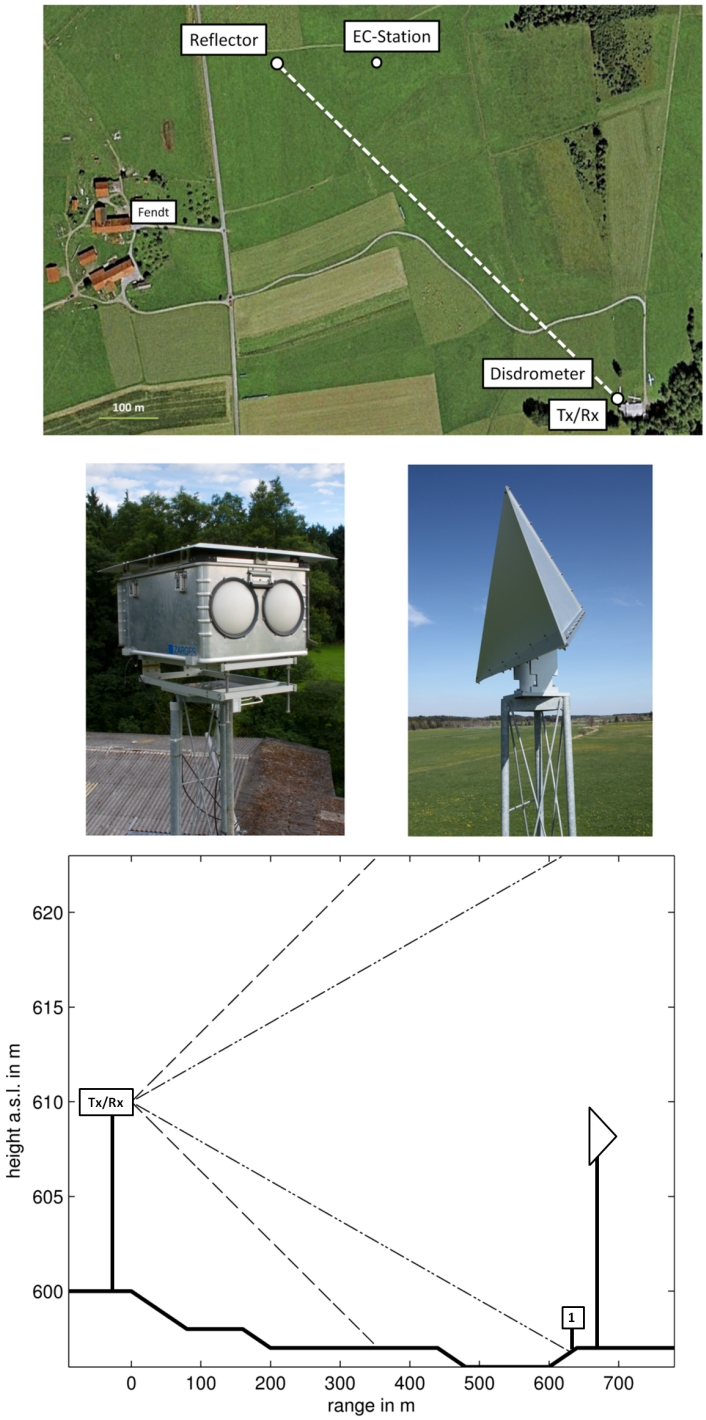

Figure 3.9 – An overview of the TERENO test site in Fendt with the locations of the Tx/Rx towers and the EC-station. In the middle, pictures of the Tx/Rx box and of the reflector in the field are given. In the height profile the 3dB beam width of the 22 GHz system (dashed line) and the 35 GHz system (dash-dotted line) is depicted. The WXT520 weather station is located at the EC-station, shown as (1) in the height profile plot.

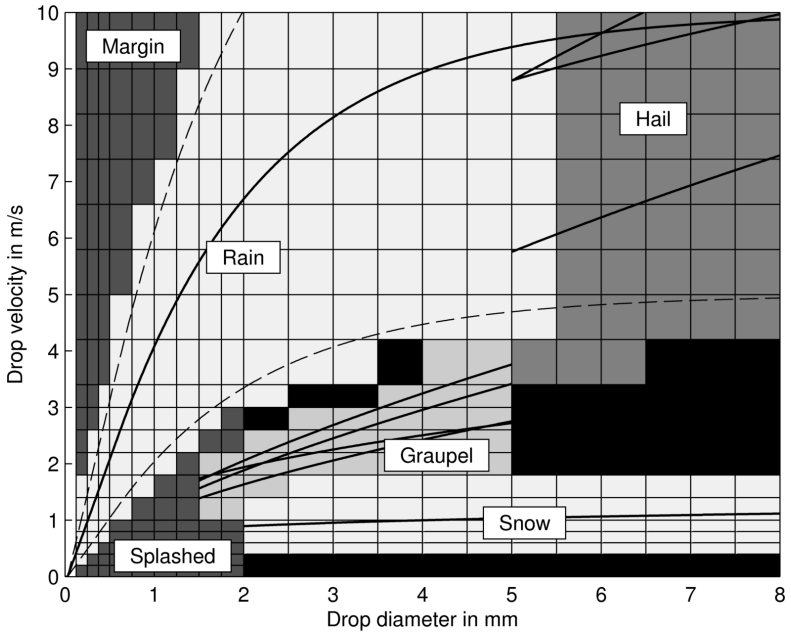

Figure 3.10 – The mask used to discriminate the different precipitation types in the raw drop and velocity data recorded by the Disdrometer. The black lines give theoretical terminal velocities for the different precipitation types. The dashed line is the 50% error margin used to define the corridor for the drops classified as rain. For details please refer to Friedrich et al. [2012]

precipitation types (rain, hail, graupel, snow) and false detections by the disdrometer (margin fallers and splashed drops) in this data, the approach presented by Friedrich et al. [2012] is adopted. It uses the theoretical terminal velocities for the different precipitation types with corresponding error margins to classify precipitation types for each diameter-velocity combination. For their data, recorded by a PARSIVEL disdrometer, they used a 60% error margin for the terminal velocity of rain drops. The successful use of a 40% margin is also reported, though. For the data of the *Thies* Laser Disdrometer a 50% margin for the terminal velocity of rain drops is used, resulting in less than 5% of rain amount being removed due to excluded drops (margin fallers, splashed drops, uncategorized). The mask applied for classification is shown in Figure 3.10.

3.3.2 Weather station

In the vicinity of the reflector tower, a Vaisala WXT520 weather station is installed at an Eddy-Correlation (EC) flux measurement tower at 2 m above the ground. It provides ten minute averages of temperature, humidity, pressure and rain rate.

Absolute humidity values q are calculated from the measured temperature T_k in Kelvin and relative humidity (RH) in % using equation 2.36 and 2.40.

3.3.3 Transmission experiment setup

Both the transmit/receive box and the thrihedral reflector are installed on top of 10 m towers. The 660 m path between the towers leads over flat grassland with an unobstructed first Fresnel zone. As can be seen from Figure 3.9 the 3 dB beam width of the 22 GHz system however hits the ground half way to the reflector, resulting in potential fluctuations due to multipath propagation. The 35 GHz system with its narrower beam is less prone to this effect.

3.4 Results

3.4.1 Precipitation estimation and DSD dependence

Rain event May 2nd 2011

As a first case study a strong isolated rain event on May 2nd 2011 is chosen. The duration of 20 minutes and the intensity with rain rates up to 30 mm/h indicate a typical convective type of rain event. The disdrometer measurements shown in Figure 3.11-b1 also indicate that a significant part of the precipitation particles has been classified as snow and hail. For the following analysis we neglect the contribution of hail since only little can be known about the actual shape, density and the water coating of the hail stones from the disdrometer measurements. These parameters however, are necessary to model their scattering characteristics [Borowska et al., 2011]. The snow particles are also neglected since attenuation by snowflakes (assumed that they are not coated with water) is very low.

Data from the experiment which is recorded at 20 Hz is averaged to 1 Hz and shown in the left column of Figure 3.11. As expected, the received signal level (RSL) displayed in Figure 3.11-a1 mimics the time course of the rain event recorded by the disdrometer (shown in Figure 3.11b1). Due to the higher sampling rate (1 Hz for the RSL compared to 1 record every minute for the disdrometer) the RSL data reveals in much more detail the rain intensity fluctuations on short time scales.

For the RSL based calculation of rain rates, attenuation values are necessary, for which a reference baseline value has to be assumed. Here, the mean value of RSL before the rain event is chosen. For continuous operation, dynamic baseline algorithms are more appropriate. They cope with the long term drift and fluctuations of RSL [Chwala et al., 2012, Goldshtein et al., 2009, Overeem et al., 2011, Rahimi et al., 2003, Schleiss and Berne, 2010].

When comparing measured A and ΔA to the values calculated from the DSD recorded by the disdrometer (Figure 3.11-b2 and 3.11-b3) and to values calculated for a Marshall-Palmer DSD based on R as measured by the disdrometer (Figure 3.11-c2 and 3.11-c3), deviations can be observed. In particular the behavior of $A_{22,h}$ and hence ΔA_{22} can not be reproduced when using a fixed DSD. This can also be seen in row 4 of Figure 3.11 where the ratio $\Delta A/A_h$ is shown. Comparison with the median volume diameter D_0 of the measured DSD, shown in Figure 3.11-c1, suggests a dependence of $\Delta A/A_h$ on D_0. This can be explained by the fact that the same attenuation level can be generated by different DSDs. With increasing D_0, ΔA will however increase due to the more pronounced asymmetry of the larger drops. As was shown in section 2.1.2 and Figure 2.5, in particular $C_{ext,22,h}$ increases in the presence of large drops ($D > 4$ mm).

For a direct comparison of measured and calculated A and ΔA, the first two rows in the

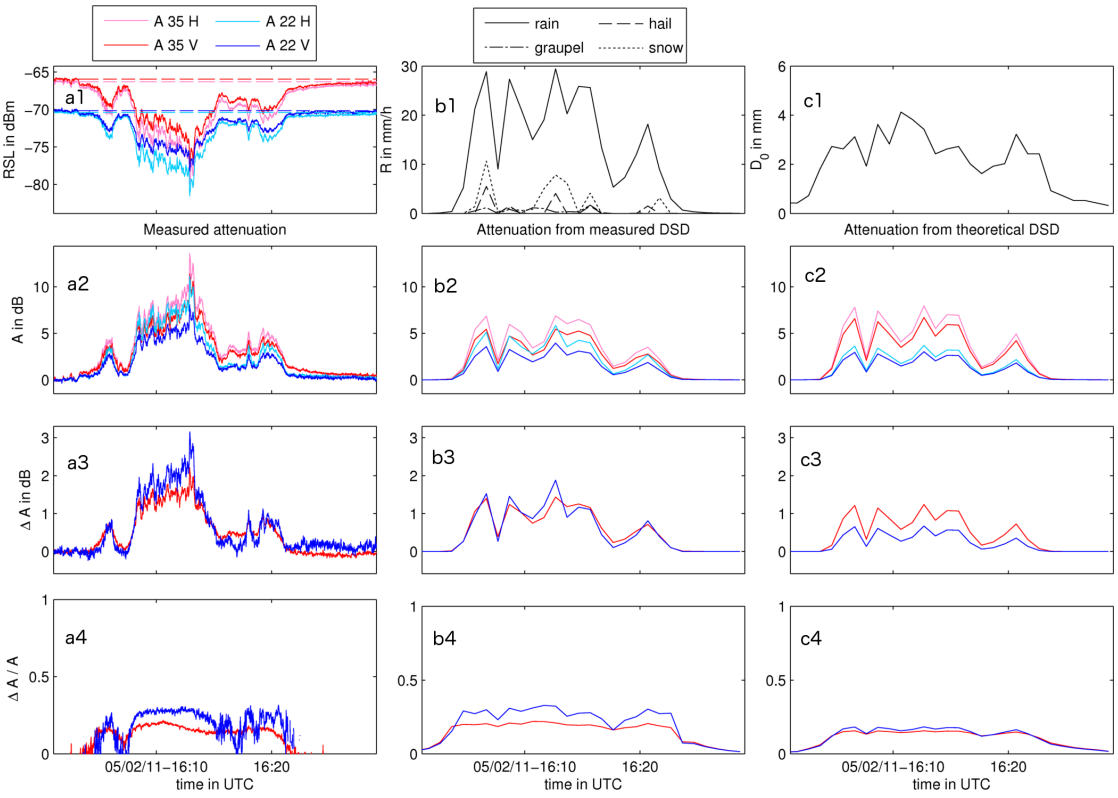

Figure 3.11 – Time series for rain event on May 2nd 2011. Data from the transmission experiment is sampled at 1 Hz. Disdrometer data has minute resolution. Plot (a1) shows the received signal level (RSL). Plot (b1) shows the rain rates for different precipitation types derived from the disdrometer raw data employing the mask shown in Figure 3.10. Plot (c1) shows the median volume drop diameter for rain. Plots in row 2, 3 and 4 show the derived attenuation A, differential attenuation ΔA and $\Delta A/A$ derived from the RSL (plots in column a), from the DSD measured by the disdrometer (plots in column b) and from a Marshall-Palmer DSD according to the rain rate measured by the disdrometer. Note that values for $A < 0.5$ dB are not shown in plot (a4) since the fraction diverges when A approaches 0.

plot matrix in Figure 3.12 show the minute averages of data from the experiment and the disdrometer. The black lines give values calculated for the different theoretical DSDs from Table 2.1. The thick dashed black line uses the power law relation given in equation 2.34 with values of a and b according to Table 3.2. As expected from the findings in section 2.1.2 and section 2.1.4 (see in particular Figure 2.12) the spread, and hence the dependence on the choice of the theoretical DSD, is smaller for 35 GHz than for 22 GHz. The measured data also exhibits this behavior.

In general the disdrometer data seems to have larger values of $\Delta A/A$. This can be explained by two effects.

First, the DSD used for the calculation of A and ΔA only contains drops classified as rain. Hail is neglected. For the attenuation measurements however, hail contributes to A and ΔA. If this contribution would be removed, A and ΔA would change. Since the axial asymmetry

Frequency in GHz	a_h	a_v	a_Δ	b_h	b_v	b_Δ
34.8	0.260	0.230	0.031	0.981	0.964	1.070
22.235	0.096	0.088	0.010	1.081	1.048	1.240

Table 3.2 – The values of a and b used in the A-R power law relation (see equation (2.34). The indices h, v and Δ denote horizontal polarization, vertical polarization and differential measurements, respectively. Values for A-R are taken from ITU [2003]. Values for ΔA-R were derived by using the recommend a and b values for horizontal and vertical polarization and performing a power law fit of equation (2.35)

of hail stones is smaller than that of large rain drops [Knight, 1986], removing hail from the signal would decrease A while $\Delta A/A$ increases. This would result in an better alignment of the data from the experiment and the data from the disdrometer.

Second, the effect of wet antenna can lead to an overestimation of A measured by the experiment. The values for low $\Delta A/A$ in Figure 3.12-a2 and 3.12-b2 indicate that the antenna must have been wet, since, $\Delta A = 0$ indicates that no rain is present. If A is still significantly larger than zero, this attenuation is likely to stem from the water remaining on the slowly drying antenna. Future research will show if the resulting deviations from the theoretical curves can be used to detect wet antenna attenuation and remove it in post-processing.

If no DSD data is available, rain rates have to be derived from measured attenuation using the A-R power law relation given in equation (2.34). This relation assumes a fixed DSD for each rain rate. Deviations of that DSD will thus lead to errors in the derived rain rate. This effect of a changing DSD is studied by comparing observed attenuation A_{obs} from the experiment to attenuation A_{calc} calculated from the measured DSD provided by the disdrometer. From A_{obs} a rain rate R_{calc} is calculated using the power law from equation (2.34) with the values from Table 3.2. R_{calc} is then compared to the rain rate R_{obs} derived from the disdrometer DSD data. When comparing the correlation between A_{obs} and A_{calc} to the correlation between R_{calc} and R_{obs}, a decrease should be observable, which should be more pronounced if the the dependence of the A-R relation on the DSD is higher.

The plots in rows 3 to 6 of Figure 3.12 show this comparison for A and ΔA. The Pearson correlation coefficient confirms the above mentioned expectation. It decreases when rain rates are derived from measured attenuation with a fixed A-R power law.

Rain event March 30$^{\text{th}}$ 2011

As second example a medium rain event on March 30$^{\text{th}}$ 2011 is chosen. Even though it is less intense than the event studied in the last section its isolated nature and short duration indicate a convective type rainfall. The large median volume diameter D_0, shown in Figure 3.13, at the onset confirms this indication. Similar to the analysis in Figure 3.11, the large D_0 is reflected in the differential signals, in particular in ΔA_{22}. The fixed Marshall-Palmer DSD cannot reproduce that.

In the scatter plots in row 1 and 2 of Figure 3.14 both, the measured attenuation values and the ones calculated from the disdrometer, indicate a significant deviation from the theoretical

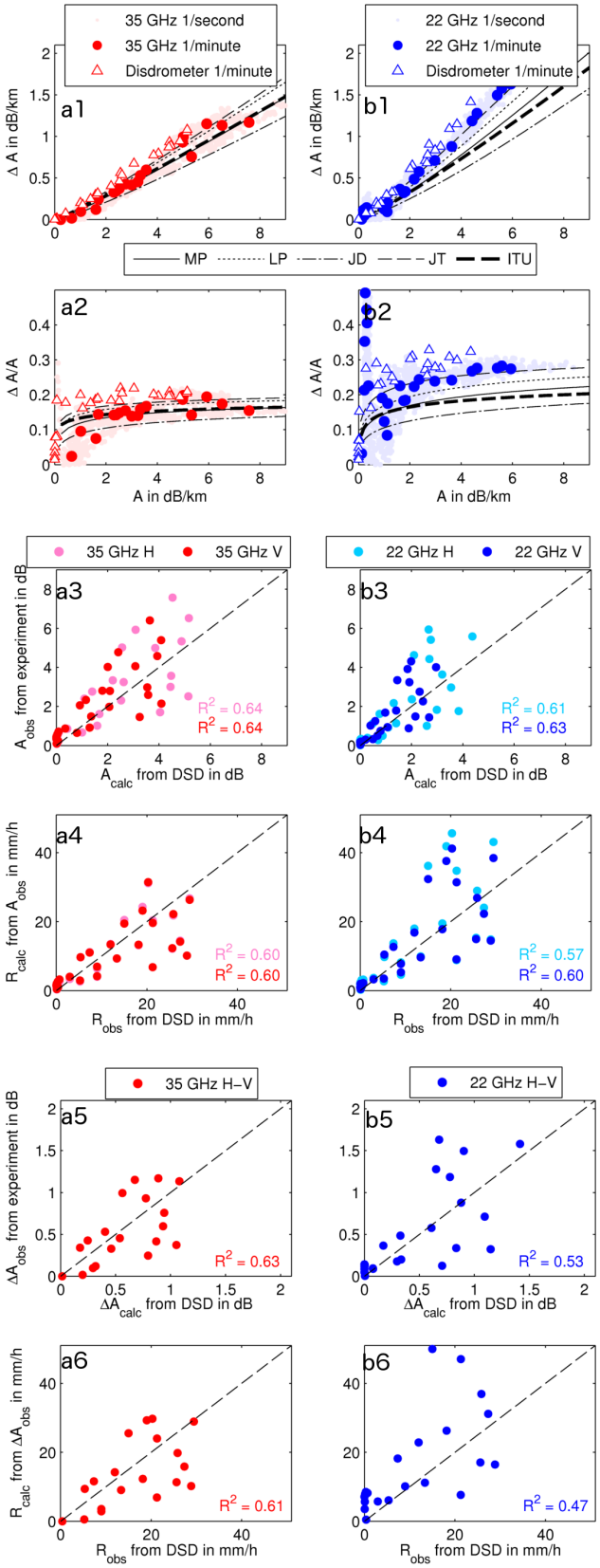

Figure 3.12 – Scatter plots of the data from the rain event on May 2nd 2011 shown in Figure 3.11. Plot (a1) shows the values of attenuation A and differential attenuation ΔA, from 1 Hz attenuation measurements of the 35 GHz system, from minute averages of this 1 Hz data and the attenuation values calculated from DSDs measured by the disdrometer. Plot (a2) shows the same data in a different representation. Plot (a3) shows A_{obs} observed by the experiment and A_{calc} calculated from the DSD. In plot (a4) R_{calc} is the rain rate calculate from A_{obs} employing the power law relation given in equation (2.34). R_{obs} is derived from the DSD. Plots (a5) and (a6) are similar to (a3) and (a4) showing values for ΔA. Plots in column (b) refer to data from the 22 GHz system. Note that the divergence of $\Delta A/A$ in plot (b2) is due to the fluctuations of A close to zero.

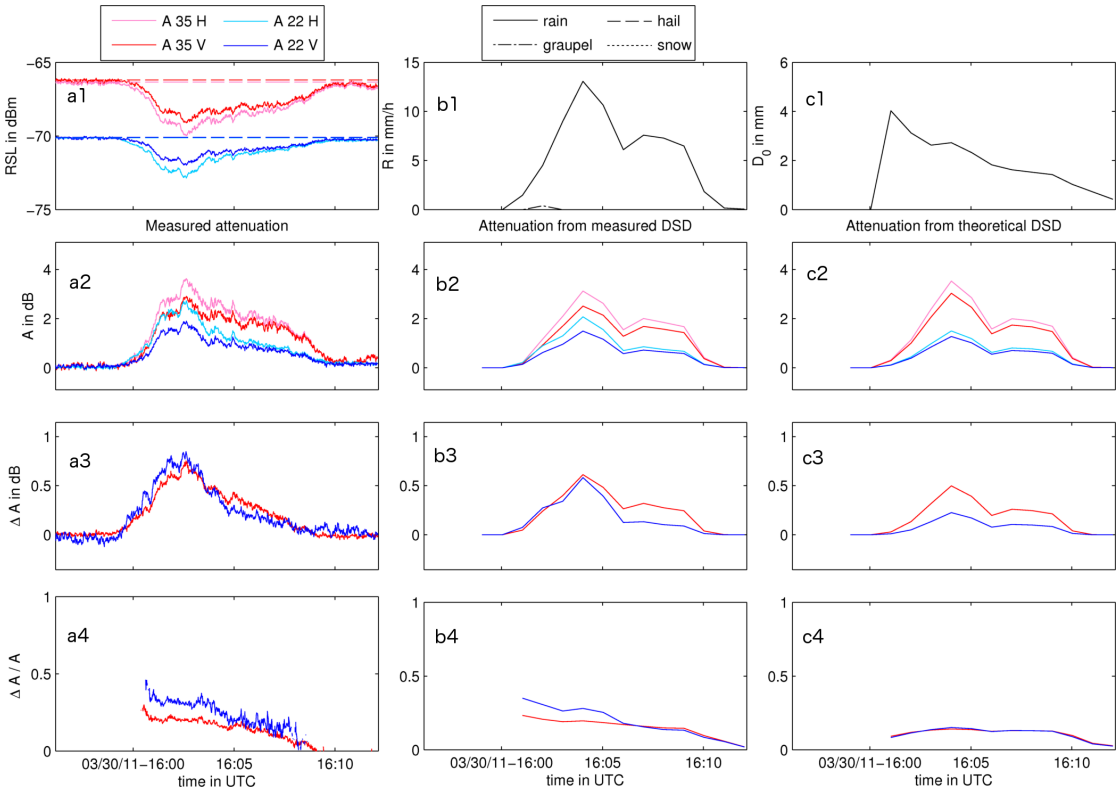

Figure 3.13 – Same as Figure 3.11 for a rain event on March 30th 2011. DSD data from the disdrometer before 15:59 UTC is missing because the exported raw data was corrupted. Precipitation intensity values given by the disdrometer's internal processing yielded $R = 0$ mm/h for this time period, though.

DSDs towards large rain drops. Again, wet antenna attenuation and its slow recovery can be observed, most pronounced in Figure 3.14-a2. The presence of comparatively large drops for the given rain rates also explains the results of the correlation analysis presented in the scatter plots in rows 3 to 6 of Figure 3.14. Similar to the result shown in Figure 3.12, the correlation decreases when going from the comparison of A to the comparison of R. In this case however, the decrease for $A_{22,h}$ and ΔA_{22} is significant. An explanation might be the strong deviation of the present DSD from the theoretical ones, as indicated in Figure 3.14-a2 and 3.14-b2.

Concluding from the results shown in Figure 3.11 and Figure 3.13 the measured data is consistent with the theoretical findings from section 2.1.2 and section 2.1.4. The almost linear relation between the integrands of A and R (see equation 2.25 and 2.1) at 35 GHz results in a low dependence of the A-R relation on the DSD, in particular for smaller rain rates $R < 15$ mm/h. This relation can be approximated well by the power law from equation (2.34) using the ITU values given in table 3.2. At 22 GHz and horizontal polarization or when using data from differential measurements, the ITU power law seems not to be able to reproduce the correct attenuation values.

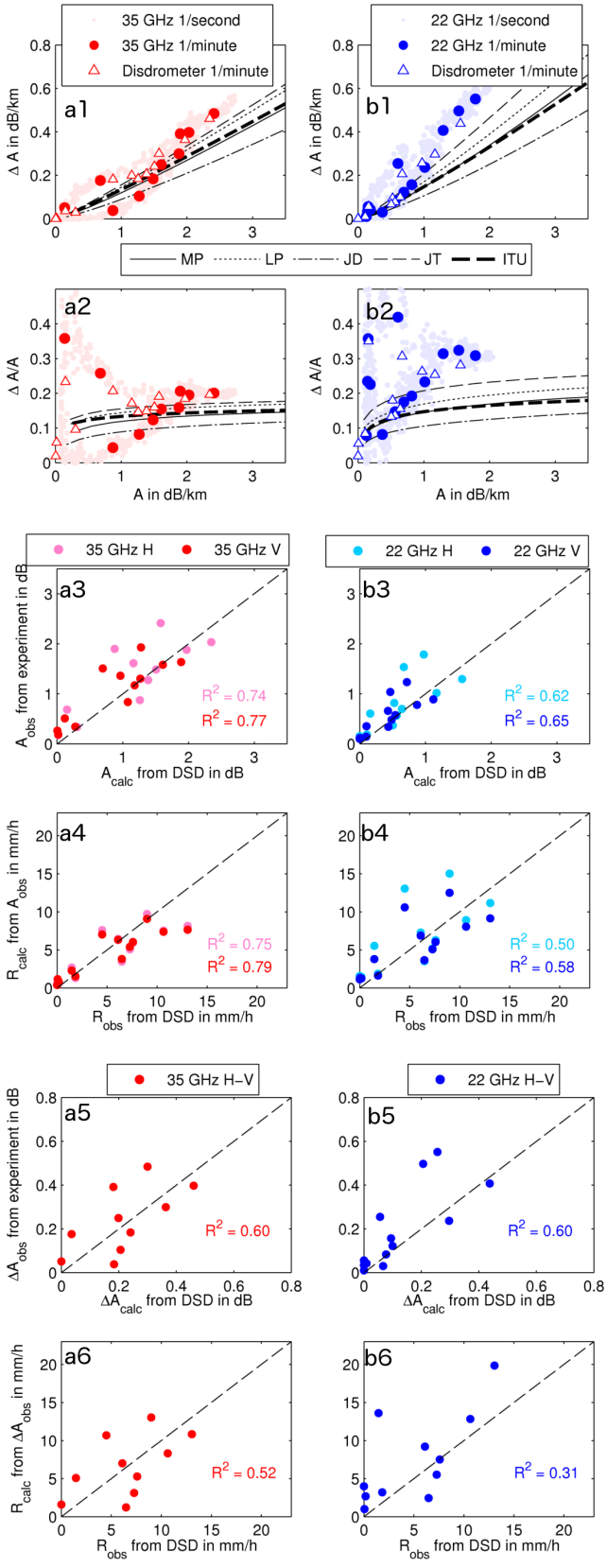

Figure 3.14 – Scatter plots of the data from the rain event on March 30th 2011. Plot structure is the same as in Figure 3.12. The divergence of $\Delta A/A$ in plot (b2) is due to the fluctuations of A close to zero.

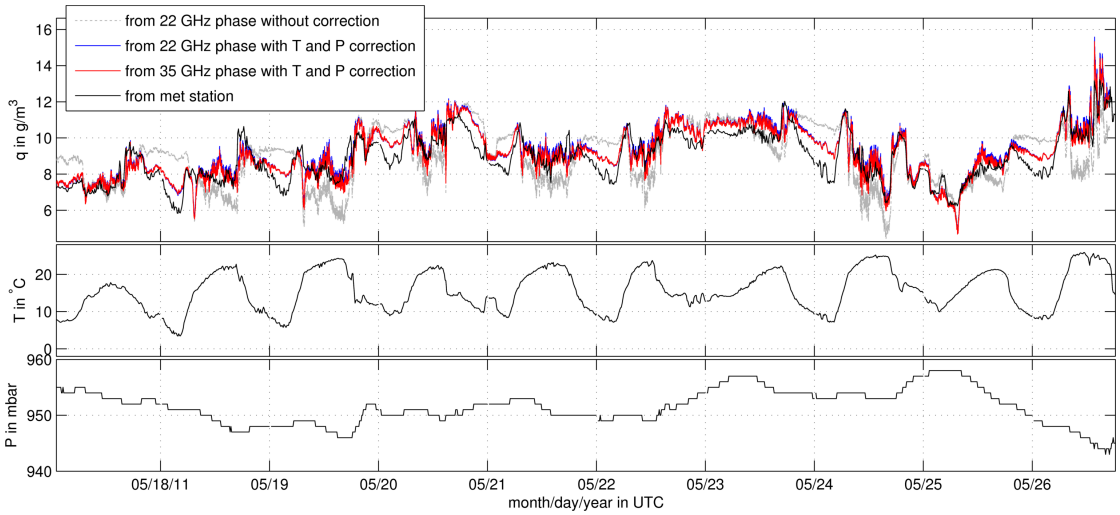

Figure 3.15 – Time series of absolute humidity derived from phase measurements of the 22 GHz and 35 GHz system. The 22 GHz data is shown with and without correcting the results using temperature T and pressure P from the meteorological station in the vicinity. The uncorrected data for the 35 GHz system would be similar and is not shown here.

3.4.2 Humidity estimation

To study the relation between the measured phase delay and the absolute humidity a period of warm weather conditions in May 2011 is selected. Phase information is taken from the 22 GHz and 35 GHz system, running at 20 Hz sampling rate. Prior to averaging to 1 Hz data, the phase skipping over every 2π, has to be unwrapped. Strong wind causes tower oscillations at 4 Hz which tend to corrupt unwrapping at lower sampling rates.

From the unwrapped phase, refractivity is calculated using equation (2.45) with the offset N_0 calculated from weather station data at noon of the starting day of the phase time series. Using equation (2.48) with temperature and pressure data from the weather station interpolated to 1 Hz, absolute humidity values are derived. The resulting time series, together with an uncorrected time series using fixed values T = 15°C and P = 953 mbar, is shown in Figure 3.15. As mentioned in section 2.2.3 and also observable here, temperature and pressure are changing on a slower temporal scale than humidity. However, comparing the corrected with uncorrected data for a longer time interval, e.g. during the course of a day, the influence particularly of the high diurnal temperature variations on the derived absolute humidity is visible. The corrected data align well with the station data. This is also confirmed by the scatter plots in Figure 3.16 and the reasonable Pearson correlation coefficient of R^2 = 0.77 and R^2 = 0.79 for both the 35 GHz and 22 GHz system. The observable deviations seem to follow a pattern. On several days (e.g. on May 19th at around 06:00 UTC) sharp decreases with sudden recoveries occur in the morning hours. Cross-checking of these incidents with radiation data (not shown here) from the weather station at the eddy correlation tower indicates that they are appearing only during days with high solar radiation. It is thus very likely that the fast decreases with subsequent recovery stem from mechanical deflection of the towers caused by one-sided heating due to solar radiation at sunrise and sunset. During night time the

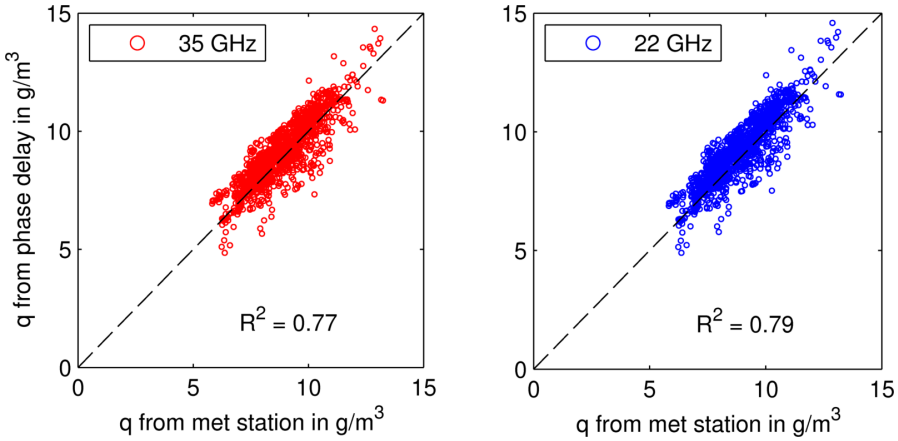

Figure 3.16 – Scatter plot of the time series shown in Figure 3.15. Here 10 minute averages of phase derived humidity values are used to be comparable to the 10 minute averages provided by the met station.

phase derived humidity is often overestimated. This might be explained by the location of the test site. It is situated in a wide flat valley, where the high soil moisture of the meadows often leads to fog when the atmosphere is stable. Thus a temperature and moisture gradient could lead to considerable differences between the met station measurements at 2 m and the measurements of the phase delay 10 m above the ground.

The deviations occurring on an smaller (sub-minute) temporal scale, and with pronounced fluctuations during daytime and maximum amplitudes around noon, originate from fluctuations of the refractive index caused by evaporation. This is an effect that is exploited in remote sensing the latent heat flux using microwave and optical scintillometers [Leijnse et al., 2007a, Meijninger et al., 2006]. With these instruments, amplitude fluctuations are evaluated. With the additional phase derived humidity measurements shown here, new insight into boundary layer processes may be possible.

3.5 Conclusion

3.5.1 Summary

A monostatic dual frequency dual polarization experiment was successfully planned, assembled and deployed in the field.

Six different attenuation measures (horizontal and vertical polarization, 34.8 GHz and 22.235 GHz, and the differential attenuation between horizontal and vertical polarization) were analyzed. Due to the relatively short path length, noise can mask the signal attenuation for weak rain events. This is in particular true for measurements of differential attenuation, which are less sensitive than measurements of specific attenuation. The analysis was hence focused on stronger convective events. The ratio of attenuation to differential attenuation $\Delta A/A$ was found to be sensitive to changes of the median volume diameter. Comparison with DSD data simultaneously obtained by a disdrometer at the test site showed reasonable agreement.

Using the disdrometer data, the effect of a variable DSD on the performance of the A-R power law fit was studied. It was shown that, as described by theory, the effect is low at 35 GHz and increases for 22 GHz and the differential measurements.

Phase delay measurements were used to derive refractivity values. Transformed to absolute humidity these data were consistent with data obtained at the weather station in the vicinity. The scale investigated by the experiment is in the same order of magnitude as the resolution of recent atmospheric models. In the future this may provide a new possibility to initialize and validate these models.

3.5.2 Outlook

Further examination of the spatial variability of humidity and its impact on the line integrated measurement is mandatory to check the accuracy of the phase derived humidity. Therefore installing additional humidity loggers as supplemental ground truth will be considered.

For the analysis of precipitation, it is also planned to install rain gauges or disdrometers for ground truthing along the path. A first next step in evaluating the attenuation data might be the implementation of the methods proposed for line integrated DSD retrieval, using two frequencies or two polarizations [Berne and Schleiss, 2009, Rincon and Lang, 2002]. Having both, two frequencies and two polarizations available, may offer an even more detailed analysis of the DSD. In addition, measurements of the differential propagation phase, which is a further independent quantity sensitive to precipitation, could add to the robustness of the DSD estimation.

Furthermore, the 25 KHz raw data sampling mode could be used to study Doppler spectra, both in transmission and reflection configuration. This would serve as the empirical complement to the numerical study done by Hipp et al. [2011] who simulated microwave propagation through rain fall explicitly considering the contribution of each single drop.

4 Rain rate estimation using commercial microwave link networks

One man's rubbish may be another man's treasure

— Proverb

This chapter introduces the idea to use attenuation data from commercial microwave link networks for precipitation observations. It presents the first application of this technique in an alpine/pre-alpine environment in southern Germany. Furthermore a new algorithm for rain event detection in the received signal time series is presented together with results of five month of application.

The chapter is based on the article "Precipitation observation using microwave backhaul links in the alpine and pre-alpine region of Southern Germany" published in *Hydrology and Earth System Sciences* [Chwala et al., 2012].

4.1 Introduction to commercial microwave link networks

A microwave link is a communication link based on microwave transmission between two locations along a line of sight radio path (exceptions are the few links for over-horizon communication using tropospheric scatter).

As with many communication technologies, they first appeared in military applications, but were soon employed in commercial applications. The first commercial microwave links were used for the transmission of long distance telephone calls. A prominent example is the communication between West-Berlin and Western Germany which was established in 1950 using an over-horizon microwave link with a length of 130 km. Until the German reunification in 1990 this important communication link was renewed several times, in particular by using higher towers. From 1978 on, a line of sight connection was possible. It was operated at around 6 GHz and provided enough bandwidth for 11.700 simultaneous long distance calls.

While the long distance communication link from West-Berlin to Western Germany was redundant from 1990 on, a new form of communication at the same time called for an increasing number of new microwave communication links. The advent of cell phones and the introduction of the GSM standard for digital cellular networks in the 1990's resulted in a rapidly growing network of cell phone base stations which were interconnected via microwave

links. Now, with the constantly rising desire for higher bandwidth for mobile applications, microwave link technology is booming. The existing network of commercial microwave links is experiencing a shift from long range links to shorter links with higher frequencies to provide higher data rates. In addition shorter links are easier, and thus faster, to deploy, since smaller towers are now sufficient to provide line of sight between the sites.

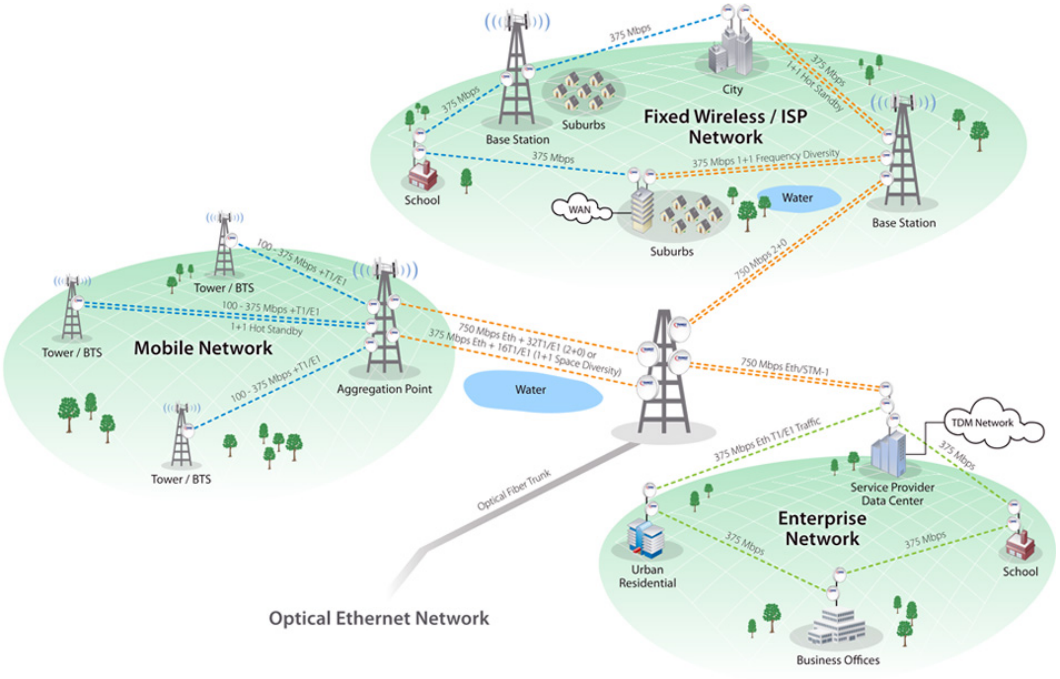

Figure 4.1 – Example of commercial microwave link networks. Common are applications as backhaul networks of the mobile phone network, as enterprise networks to link different sites and as connection nodes of the internet service provider (ISP) networks. All microwave links (dashed lines) are commonly operated in the range between 10 GHz to 40 GHz. (Image source http://www.trangosys.com)

But commercial microwave links are not only used in cell phone networks. They are also commonly used for the integration of remote locations in wide area networks (WAN) of enterprises or research facilities (see Figure 4.1). In general, they are used everywhere where high bandwidth is needed but installing fiber optics is to expensive.

The total number of commercial microwave links in operation can only be estimated roughly. For the Netherlands, with a land area of $\approx 35\,000$ km^2, Leijnse et al. [2007c] give a number of 12 000 links. The reported estimate for Germany, with an area of $\approx 350\,00$ km^2, is 100 000 links. For both countries the density is ≈ 0.3 links per km^2, which hence could serve as a rough estimate for European countries. For less developed or less populated countries the density is assumed to be lower.

4.2 Study region and data sources

4.2.1 Study region

The study region is the area between the cities Weilheim and Garmisch-Partenkirchen located in the southern part of Germany 40 to 90 km south of Munich. An overview of the region with the locations of all used microwave links, rain gauges and the weather radar is given in Figure 4.2. It stretches from the upper Bavarian lowlands in the north at about 600 m a.s.l. to the high alpine area in the south with summits up to 3000 m a.s.l. (Zugspitze 2962 m). Accordingly, the southern part of the study region is characterized by steep topography. Hence, strong gradients in temperature and mean rain rate exist on very short horizontal scales. In contrast to the lower parts of the study region with an annual precipitation of 1100 mm and a mean temperature of 8 °C, the weather station on Zugspitze yields 2000 mm and −4.7 °C. Furthermore, climatic conditions in the study region are characterized by strong seasonal and diurnal variations. The typical wind direction is southwest to northwest.

4.2.2 Microwave links

Data from five links from Ericsson GmbH, which are part of a German mobile phone network, are used. In contrast to other studies with commercial microwave links [Overeem et al., 2011, Schleiss and Berne, 2010, Zinevich et al., 2008], received signal level (RSL) data is not received from the network providers, but rather recorded directly at the towers from a monitoring output of the link systems. This is accomplished with a data logger, described in more detail in section 4.2.5, which sends the data to a database server via GSM. This restricts data acquisition to a smaller number of links, but gives the advantage of a high resolution of the RSL (< 0.05 dB) and a selectable sampling rate.

Of the equipped links, two are located in the pre-alpine area around Mount Hoher Peißenberg where the German Meteorological Service (DWD) operates a meteorological observatory with the C-Band weather radar described in section 4.2.4. The other three links are located in the valley around Garmisch-Partenkirchen. All links have a constant transmission power (in contrast to links that automatically change their transmission power to compensate for additional path attenuation). However, since they were not built as measurement devices, small changes (up to some tenths of dB) due to temperature-dependent drifts of the electronics may be possible. Compared to the expected attenuation along the link path, these changes are fairly small though. Hence, in this study a constant transmission power is assumed.

Details of link length, location, frequency, polarization and altitude difference are summarized in Table 4.1.

4.2.3 Rain gauges

For comparison with the link-derived rainfall rate, data from six rain gauges in the test area are used. Three gauges are operated by the DWD which provide hourly rain rate data with 0.1 mm resolution.

In addition to these, three rain gauges were operated at the slope beneath the steepest link connecting the center of Garmisch-Partenkirchen (700 m a.s.l.) and the summit of Mount Wank (1780 m a.s.l.) to better capture the inhomogeneity of precipitation caused by the

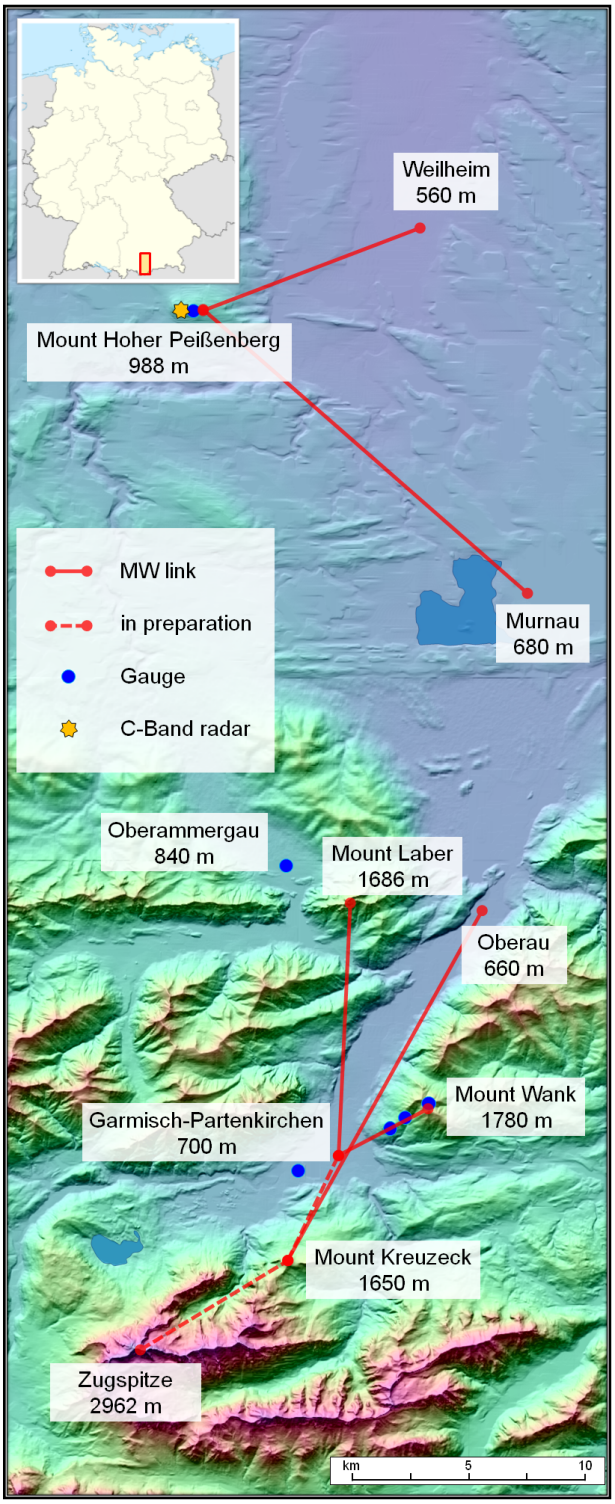

Figure 4.2 – Overview of the study region in Southern Germany showing the location of the DWD C-band radar, all microwave links and all rain gauges used in this study.

Name	From	To	Length	Altitude difference	Frequency	Polarization
hop2-murn1	Mount Hoher Peißenberg	Murnau	17.4 km	300 m	15.0 GHz	vertical
hop2-wh0	Mount Hoher Peißenberg	Weilheim	10.2 km	420 m	18.7 GHz	vertical
gap0-gap4	Garmisch-Partenkirchen	Mount Wank	4.0 km	1050 m	18.7 GHz	horizontal
gap3-oau4	Mount Kreuzeck	Oberau	17.1 km	950 m	15.0 GHz	vertical
gap0-oagau1	Garmisch-Partenkirchen	Mount Laber	10.4 km	940 m	23.0 GHz	vertical

Table 4.1 – Table of all links used in this study.

Name	Location	Altitude	Accuracy
gap	Garmisch-Partenkirchen	720 m	0.1 mm h^{-1}
oagau	Oberammergau	840 m	0.1 mm h^{-1}
hop	Hoher Peißenberg	960 m	0.1 mm h^{-1}
wank900	Mount Wank	930 m	0.2 mm h^{-1}
wank1300	Mount Wank	1340 m	0.2 mm h^{-1}
wank1750	Mount Wank	1750 m	0.2 mm h^{-1}

Table 4.2 – Table of rain gauges used in this study.

orography. The gauges are tipping buckets with 0.2 mm resolution and are placed at 930 m, 1340 m and 1750 m a.s.l. Because all locations are on the steep forest-covered windward side of the mountain, the accuracy of the absolute values of rainfall amount is affected by large uncertainties. Qualitative information on the occurrence of rain events in general can nonetheless be deduced. A summary of all gauges can be found in Table 4.2.

4.2.4 Weather radar

Radar data are obtained by the DWD C-band weather radar at Mount Hoher Peißenberg. It is not part of the operational radar network, which comprises 16 radar systems covering the whole area of Germany, but rather serves as a research testbed for innovations that could be introduced to the next generation of the operational network. Because of this, data are not always continuously available as soft- and hardware are being upgraded from time to time. Nevertheless, it is the preferred source of radar data because of its vicinity to the microwave links and to the Alps in general.

The radar covers a circular area with a radius of 256 km and generates a precipitation scan every five minutes. Here, the reflectivity data of those five minute precipitation scans (the so-called DX product) are used. They are provided with an angular resolution of 1° and a range resolution of 1 km. The DX product is already clutter-corrected by means of a statistical and a

dBZ shower index	< 36.5			36.5–44	> 44
	< 3.5	3.5–7.5	> 7.5		
a	125	200	320	200	77
b	1.4	1.6	1.4	1.6	1.9

Table 4.3 – Table containing the values of a and b used for the conversion of radar reflectivity Z to rain rate R with $R = aZ^b$ according to findings of the RADOLAN project. Overestimation of convective precipitation and underestimation of stratiform precipitation shall be avoided by distinguishing precipitation types from the reflectivity values (in dBZ) and a shower index for each pixel. The later is the mean value of the absolute differences in reflectivity of the neighboring pixels [Bartels et al., 2004].

Doppler clutter filter. However, for the two links in the vicinity of the radar, ground clutter is already reduced by the elevated radar location on Mount Hoher Peißenberg approximately 300 m above the surrounding area. The radar beam elevation angle is 0.5°. Hence, the area around Garmisch-Partenkirchen is blocked by the mountains in between, making radar data unavailable for the three links in the southern part of the test region.

To derive rain rates from the radar reflectivity, the multi part Z-R-relation developed by the DWD within the RADOLAN project [Bartels et al., 2004] is used. Details are given in Table 4.3. The resulting rain rates are then projected from polar coordinates to a 100 × 100 km Cartesian grid with a grid size of 1 × 1 km.

4.2.5 Data acquisition and data management

Data logger

To acquire RSL data from the microwave links, *Cinterion TC65i* modules are used as data loggers at the link sites. The modules combine a GSM modem, two ADC (analog-to-digital converter) channels and a Java virtual machine to run the custom logging program. The module's ADC input is connected to the RSL monitoring voltage output of the link. If a second link is available at the same location, its RSL output can be connected to the second ADC, which will help save costs when installing loggers at nodes where usually several links are located.

The RSL monitoring voltage is sampled every three seconds and stored as a minute average. Via the GSM module, the recorded data are then transferred to the FTP port of a server. Since the minimal java virtual machine installed ex factory does not implement FTP, the free FTP library Ftp2Me [László, 2011] is used. With a conversion factor distinct for each link system, the recorded voltage can then be converted to RSL in the next processing step. The conversion factors are provided by Ericsson GmbH. To assure good data consistency, the logger requests the current time via time protocol from the *Physikalisch-Technische Bundesanstalt* (PTB) in Germany to update its system time used to timestamp the data. Each logger also has a unique *International Mobile Station Equipment Identity* (IMEI) number which is used to organize the raw data storage at the server so that distinguishing data from different loggers is straightforward. The cryptic IMEI is then resolved to the real microwave link name in the

database.

If RSL data are not directly available from the backhaul network providers or if higher resolution data are required for research, the developed data logger can offer a simple and cheap alternative. Given that permission from the provider is obtained, installation is possible wherever the used microwave link hardware provides an analog RSL voltage monitoring output.

Data base

To ease analysis, processing and storage organization of the daily increasing amount of RSL records, a database system is used. The framework consists of a MySQL backbone, containing the tables for all data, and python scripts for parsing and exporting data to and from the database. Besides RSL data, it also contains all important information on the specific microwave links (locations, frequency, polarization, etc.), rain gauge data and additional meteorological data from the institute's own met station on the summit of Mount Wank. It is easily expandable for new data sources. Export for automatic processing and research work can be done via a command line tool to CSV(comma-separated values) files or binary matlab structures.

4.3 Data processing: Wet/dry classification

4.3.1 Background

As shown in section 2.1.2, the attenuation of microwave radiation strongly depends on the amount of precipitation along its path of propagation. Hydrometeors are however not the only source of disturbance. All other atmospheric parameters like gas concentrations, pressure, humidity, temperature (see section 2.2.2) and even aerosols [Liebe, 1989] or dust particles [Ho et al., 2004] can cause signal impairment. Small changes of the transmission power due to drifts of the link electronics may also alter the RSL. However, compared with the impact of precipitation, these effects are minor. But even during clear sky conditions, the RSL level is always fluctuating, because the atmospheric conditions are constantly changing. For special layering of the atmosphere, so-called ducting, where gradients of the refractive index cause the direction of wave propagation to bend, losses of several dB are possible [Valtr et al., 2011]. Thus, to derive meaningful precipitation information from microwave link data, the fluctuations of the RSL have to be distinguished between those caused by precipitation and those caused by other effects. As there is usually no reliable information on the atmospheric conditions along the links available, discounting their impairment on the signal is not feasible. In order to still derive meaningful rain rates from microwave link data, two directions can be taken.

First, the differential polarization signal from a dual polarization-link cancels out the unwanted fluctuations [Ruf et al., 1996]. This is because the differential signal is only affected by the unequal raindrop diameters in the horizontal and vertical direction depending on the drop sizes, which in turn depends on the rain rate.

The second way is to determine in which periods rain events occurred (wet period) and which were dry (dry periods). The attenuation during a rain event could then be calculated from a baseline, which is derived from the dry period before it, assuming that the baseline does

not significantly change during the rain event. This was first shown by Rahimi et al. [2003] who analyzed the correlation between RSL time series for different frequencies recorded with purpose built dual-frequency links. Wet events could be distinguished from dry ones by significantly higher correlation values. The same approach was taken by Goldshtein et al. [2009] using the correlation between bidirectional signals of commercial links. An extension to this method was presented by Rayitsfeld et al. [2012] using a hidden Markov model. Overeem et al. [2011] also analyzed correlation between different links to detect wet periods. They compared RSL levels of several links (not further than 10 km away from each other) from a dense network of microwave links in an urban area.

In commercial microwave link networks, usually only one polarization and one frequency are available along a certain link path. Density of the network also varies considerably between rural and urban areas. Hence, the above-mentioned methods are not always applicable. Nevertheless, a determination of wet and dry periods is possible using time series analysis tools. Schleiss and Berne [2010] showed that a windowed standard deviation sliding along a RSL record from commercial links accomplished this task quite robustly. Applying this method to the specific data recorded with the modules directly at the towers (i.e. specific data resolution, link topography and alpine/pre-alpine terrain), some limitations were encountered though. Distinguishing between light rain events and dry fluctuations was not always successful. Thus, a new analysis tool was developed which uses short-time Fourier transform (STFT), a sliding windowed fast Fourier transform (FFT).

4.3.2 Algorithm

The problem to distinguish wet and dry periods in the RSL data records can be viewed as a problem of pattern recognition in time series. A human observer, who has experience in comparing RSL data with rain gauge records, can very often easily detect even weak rain events by looking at the course of the RSL time series. For larger data sets, this is of course not feasible and scientifically not satisfying. Thus, the main task is to find features defining "the look" of a rain event that are easily extractable from the time series by means of a computer algorithm.

This task is approached by analyzing spectra of short snippets of the RSL time series R_i with $i \in \{1,\ldots,N\}$, N being the length of the time series. For each time step t, a short section of the RSL data is taken:

$$\vec{R}(t) = \{R_k | k \in \{t-L, ..., t+L\}\} \tag{4.1}$$

with length $2L$ (a length of 256 points was found to perform best and is used for all following analysis), windowed by a Hamming window ω, from which the Fourier transform is calculated:

$$\mathscr{F}(f,t) = \mathrm{FFT}(\omega\vec{R}(t)) \tag{4.2}$$

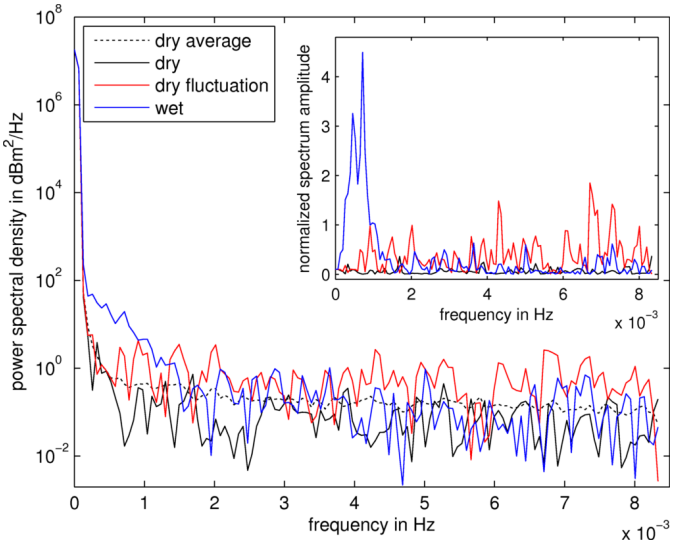

Figure 4.3 – Typical spectra for 256 min snippet (with a Hamming window) from a RSL time series for different atmospheric conditions. The inset shows the spectra normalized with the average dry spectrum by division. Deviation from the mean dry spectrum is largest for the low frequency part of the *wet*-spectrum. Note that for the *dry fluctuation*-spectrum the observable deviation is highest in the high frequency part.

via FFT. As only the spectrum of the amplitudes are of interest, the power spectral density

$$P(f,t) = \frac{2\,|\mathscr{F}(f,t)|^2}{F_\mathrm{s}\,\sum_0^L \omega^2} \tag{4.3}$$

is used for further analysis. The normalization factors used are the sampling rate F_s and the sum over all Hamming window weights. The received spectrum is just a different representation of the short time series section around t, only in the frequency domain. Effects that occur at a certain frequency or in a certain frequency range are thus more easily observable. Figure 4.3 shows example spectra for three points in time of a RSL record with different atmospheric conditions: a rain event, a dry period and a dry period that causes strong signal fluctuations.

The raw spectra all exhibit a similar $1/f$-like shape with increasing amplitudes towards low frequencies. To ease the analysis of the amplitude deviations during rainy periods compared to dry periods, a normalization of the spectra has to be applied. Using a general spectrum (e.g. $1/f^\alpha$ with $\alpha \in [0.5, 1]$) for the normalization of all links did not yield satisfying results. This is due to the fact that the link spectra deviate from $1/f^\alpha$ in the low frequency regime. The deviations also differ for each link.

Thus, for each point in time t, the normalized spectrum

$$P_\mathrm{norm}(f,t) = \frac{P(f,t)}{P_\mathrm{mean\ dry}(f)} \tag{4.4}$$

is calculated by division through a mean dry spectrum $P_{\text{mean dry}}$. In this study, the dry period used to determine $P_{\text{mean dry}}$ was chosen by visual inspection of the RSL time series. The duration of the averaging period was approximately 48 h for each link. However, since this step has to be performed only once for each link, the dry period could be chosen by selecting a time of stable dry weather from reanalysis or gauge data. Using this approach, a determination of $P_{\text{mean dry}}$ would also be feasible for a larger number of links.

The inset in Figure 4.3 shows the three spectra for the three different atmospheric conditions in normalized form. Besides the obvious strong deviation at low frequencies for the wet period, the dry period with strong fluctuations also shows considerable differences from the dry mean. Contrary to the wet period, its deviation spreads over the whole frequency range with the highest amplitudes towards high frequencies. That is, not only can the wet periods be identified by the strong deviation at low frequencies, but they can also be distinguished from dry periods by the uneven distribution of the deviations. Hence, the difference

$$P_{\text{sum diff}}(t) = P_{\text{sum low}}(t) - P_{\text{sum high}}(t) \tag{4.5}$$

of the sums of the normalized low and high frequency amplitudes is used as indicator, where

$$P_{\text{sum low}}(t) = \sum_{f \le f_{\text{divide}}} \frac{P_{\text{norm}}(f,t)}{N_{\text{low}}} \tag{4.6}$$

$$P_{\text{sum high}}(t) = \sum_{f > f_{\text{divide}}} \frac{P_{\text{norm}}(f,t)}{N_{\text{high}}} \tag{4.7}$$

with f_{divide} defining the frequency at which the spectrum is divided and N_{low}, N_{high} being the number of frequencies used in each sum.

If the difference $P_{\text{sum diff}}$ exceeds a certain threshold σ, the corresponding period is marked as wet. Hence, for each point in time t, the following decision rule can be defined:

$$t = \begin{cases} \text{wet if } P_{\text{sum diff}}(t) > \sigma \\ \text{dry if } P_{\text{sum diff}}(t) \le \sigma. \end{cases} \tag{4.8}$$

During wet periods, the baseline R_{base} of the RSL is kept constant at the level of the last value t_{lastdry} of the last dry period. For the dry period, the baseline always follows the RSL level. That is

$$R_{\text{base}}(t) = \begin{cases} R(t_{\text{lastdry}}) & \text{if wet} \\ R(t) & \text{if dry.} \end{cases} \tag{4.9}$$

The attenuation is then

$$A(t) = R_{\text{base}}(t) - R(t) \tag{4.10}$$

which is always zero for the dry periods. If the attenuation (and thus the rain rate) becomes

negative, the rain rate is set to zero. This sometimes happens at the end of a rain event when the baseline was set too low at the beginning.

4.3.3 Example

For the following exemplary application of the algorithm presented in the last section, the threshold $\sigma = 2.5$ and the spectrum division frequency $f_{\text{divide}} = 4.3 \times 10^{-3}$ Hz have been chosen by hand. Section 4.3.4 will deal with the optimization of these two parameters to get optimal wet and dry detection performance.

The example of the application of the wet/dry classification algorithm is shown in Figure 4.4. It is applied to a 18-day time series of RSL data recorded in summer 2010 at the link *gap0-oagau1* from Garmisch-Partenkirchen to Mount Laber near the city of Oberammergau. The topmost plot (Figure 4.4a) shows the minute resolution RSL time series recorded by the data logger. Within the 18 days, several rain showers passed the link. The slight attenuation events around the 19 and 20 June indicate a long lasting stratiform rain event. On the 22 and 30, three weak and short events occurred. The last days of the time series around the 4th and 5th July are dominated by sharp attenuation events, which can be assumed to stem from more convective showers.

In Figure 4.4b, a spectrogram of this time series is shown that comprises the normalized spectra $P_{\text{norm}}(t)$ for each minute, with the frequency along the y-axis and the amplitude color coded. A window length of 256 points was used. The uneven distribution of the normalized amplitudes during rain events (which was already shown in Figure 4.3) is also visible in this representation of the time series. During the dry period from the 23 to the 29 June, a daily periodicity is revealed with stronger fluctuations (higher amplitudes) in the morning hours.

To visualize the decision of whether a period is wet or dry, P_{sumdiff} and the threshold σ are plotted in Figure 4.4c. Following the decision rule in equation (4.8), a shaded area is added to indicate a wet period where $P_{\text{sumdiff}} > \sigma = 2.5$. The baseline, shown in the Figure 4.4d, is then set according to equation (4.9). With the magnified y-axis compared to the topmost plot, the fluctuations during dry periods are now clearly visible.

With the baseline set, it is now straightforward to calculate the rain rate with the power law from equation (2.34) and the a- and b-values taken from the interpolation of the ITU recommendations. Figure 4.4 comprise the calculated hourly rain rates and accumulated sum of rain, respectively. For comparison, data from the two nearest DWD rain gauges are shown. Reasonable agreement can be observed between all three precipitation observations. Deviations are of course likely because the gauges are several kilometers away from the link and thus they do not necessarily collect the same amount of rain.

4.3.4 Adjustment for different links

For the example shown in Figure 4.4, the threshold σ and the frequency f_{divide}, at which the spectrum is divided, were chosen by hand to best fit the event detection by the rain gauge. However, this is not feasible for a larger number of links and a longer time series. To determine the best values for σ and f_{divide} for each of the five links, the algorithm's performance is analyzed for a wide range of values over the period July 2010 to October 2010. Measures of

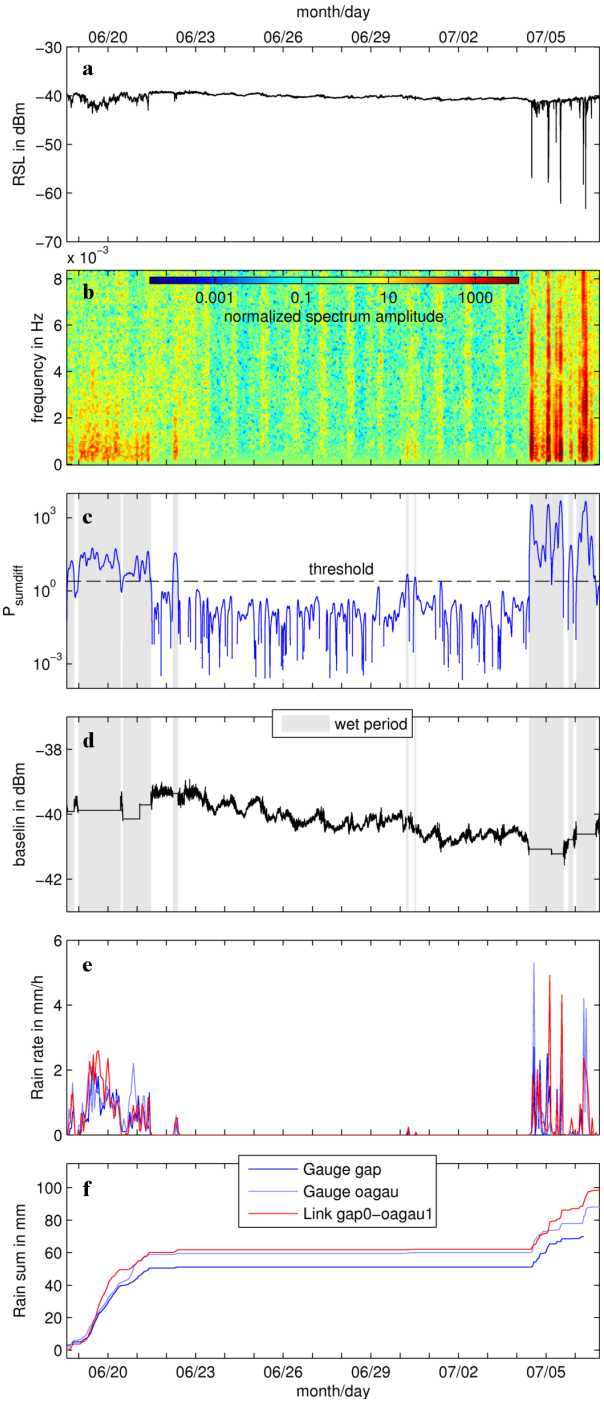

Figure 4.4 – Application of the proposed wet/dry classification algorithm to a 18-day RSL time series in summer 2010 from the link *gap0-oagau1*. The plots from top to bottom show **(a)** the RSL time series, **(b)** its spectrogram, **(c)** the difference of the spectrum amplitude sums P_{sumdiff} (see text for explanation), **(d)** the derived baseline for the RSL time series and **(e)** the calculated rain rates plus **(f)** the accumulated sum, both compared to two nearby rain gauges.

the performance are the error rates of wet and dry detection which are based on the number of wet and dry hours for link and gauge measurements. Important to note is that the hourly classification of the link data is based on the mean hourly rain rate. Only if it is larger than zero, the hour is classified as wet. Hence, it is possible that an hour containing minutes that were classified as wet is not counted as wet in this analysis, if it did only contain negative minutely rain rates which were set to zero during processing. Negative rain rates (or negative attenuation) occur if the RSL baseline is set too low, which may happen for values of σ far below the optimum. In this case, the baseline will be set at an inappropriate moment. It may then remain unchanged for a long time, because, for very low values of σ, most of the periods are classified as wet, since P_{sumdiff} easily exceeds σ. For this reason, the number of hours classified as wet here does not steadily decrease with increasing σ, although the number of minutes classified as wet by the wet/dry classification algorithm does.

Using the number of hours $N_{\text{link\&gauge=wet}}$ and $N_{\text{link\&gauge=dry}}$, where both link and gauge are classified as wet or dry respectively and the number of hours $N_{\text{gauge=wet}}$ and $N_{\text{gauge=dry}}$, where the gauge indicates a wet or dry period, respectively, we define the error rates as

$$\mathscr{E}_{\text{wet}} = 1 - \frac{N_{\text{link\&gauge=wet}}}{N_{\text{gauge=wet}}} \tag{4.11}$$

$$\mathscr{E}_{\text{dry}} = 1 - \frac{N_{\text{link\&gauge=dry}}}{N_{\text{gauge=dry}}} \tag{4.12}$$

which form the weighted mean error rate

$$\mathscr{E}_{w\text{mean}} = w\,\mathscr{E}_{\text{wet}} + (1-w)\mathscr{E}_{\text{dry}} \tag{4.13}$$

with the weighting factor w. Here, $w = 0.6$ is chosen to emphasize the error of wet detection. This is motivated by the fact that a misclassification of a dry period as wet is less severe, since, if the gauge is regarded as truth, it is not raining in this period. Hence, the attenuation (and thus the rain rate derived from the link) is expected to be low [Rahimi et al., 2003]. The dry error of course still has to be taken into account due to the possibility of large fluctuations in absence of rain, which is exactly the reason why a wet/dry classification is necessary.

Besides σ and f_{divide}, the window length, which should be a power of 2 for fast computation of the Fourier transform, is another crucial parameter for the algorithm's performance. 256 points (with the minute-averaged data, i.e. 256 min) was found to perform best. Shorter windows yielded more problems with detecting long lasting, almost constant rain events, for the short window does not see the long-term fluctuation. Longer windows in contrast had drawbacks in detecting small and short events because their contribution to the Fourier spectra is blurred out.

The results of the performance analysis for a window length of 256, with threshold values $-6 \le \sigma \le 6$ and frequency division values $0\,\text{Hz} \le f_{\text{divide}} \le 8.3 \times 10^{-3}\,\text{Hz}$, are given in Figure 4.5. All five links exhibit more or less the same behavior. Apart from the non-continuously rising or falling region at low σ values, a larger σ yields a lower dry detection error rate (because more and more points are classified as dry since P_{sumdiff} is smaller than σ more often) and a higher

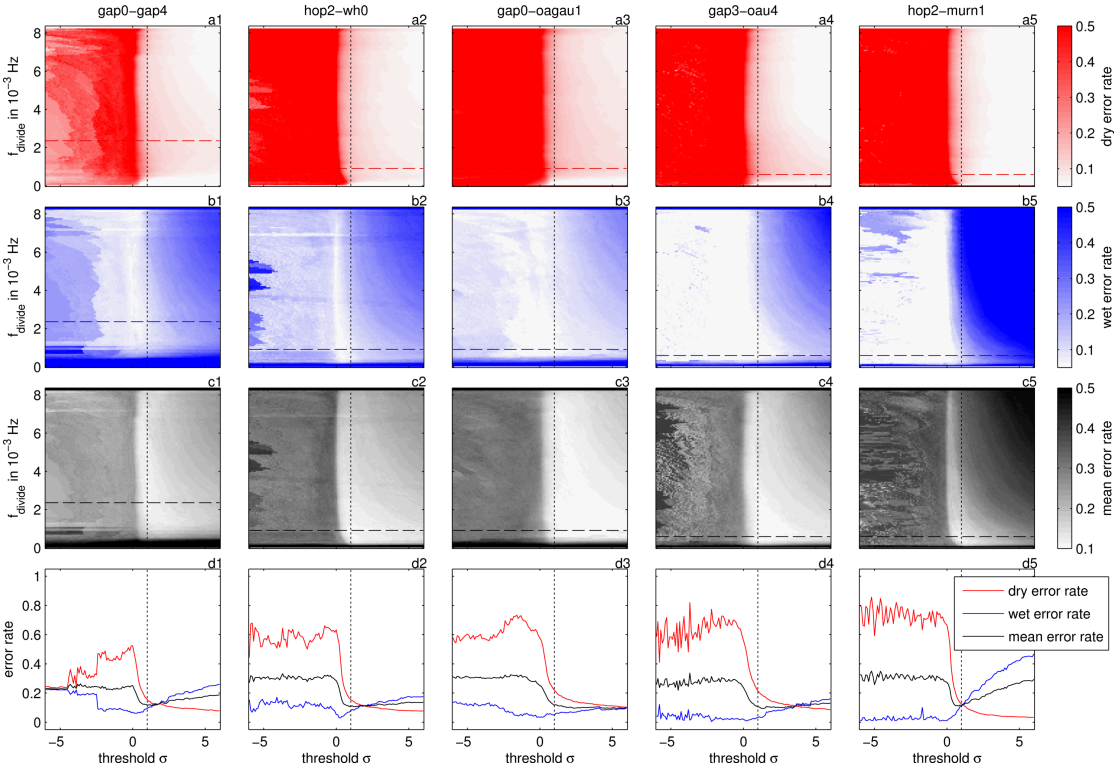

Figure 4.5 – Wet, dry and weighted mean detection error rates for the five links depending on the threshold σ and the frequency of spectrum division f_{divide}. A window length of 256 was used. The bottommost plots (d1 to d5) show the evolution of the error rates for different σ at a certain f_{divide} indicated by the dashed lines in plots a,b and c. The chosen values for f_{divide} are proportional to the reciprocal of the link length (detail see text). The links are sorted from left to right with increasing length.

wet detection error rate (because fewer and fewer points are classified as wet). Above a certain threshold value $\sigma \approx 0$, the dry detection error rate of all links rapidly decreases, converging to zero for increasing σ. The increase of the wet detection error rates also starts at $\sigma \approx 0$. Except for *hop2-murn1* (see Figure 4.5-b5), this increase is small compared to the decrease of the dry detection rate. The cause for the peculiar behavior of *hop2-murn1* is not yet clear.

Figure 4.5-b1 to 4.5-b5 also reveal the influence of the value of f_{divide} on the error rate. With lower f_{divide}, the increase of $\mathscr{E}_{\text{wet}}$ towards higher threshold values σ is slowed down, resulting in a wider range of good σ values. There is a lower boundary for optimal f_{divide} values though. If f_{divide} is set too low, the effect of rain events on the spectrum amplitudes (the increased amplitudes in the low frequency regime) is not contained in P_{sumlow} anymore. Thus, P_{sumdiff} stays small and does not exceed σ. Hence, less or no periods are classified as wet. This lower boundary of f_{divide} is dependent on the link length (note that the links in Figure 4.5 are sorted by link length, increasing from left to right). The longer the link, the more averaging occurs. Thus, the time scales on which changes in the RSL happen become longer [Leijnse et al., 2008]. That is, the frequencies at which rain events impact the RSL time series should decrease with

Link name	Length in km	Optimum			Near optimum				
		f_{divide} in 10^{-3} Hz	σ	$\mathcal{E}_{\text{wmean}}$	f_{divide} in 10^{-3} Hz	f_{divide}^{-1} in 10^{3} s	σ	$\mathcal{E}_{\text{wmean}}$	R^2
gap0-gap4	4.0	2.60	1.1	0.110	2.40	0.42	1.0	0.119	0.61
hop2-wh0	10.2	0.85	1.0	0.102	0.92	1.09	1.0	0.110	0.81
gap0-oagau1	10.4	0.72	3.9	0.090	0.92	1.09	1.0	0.117	0.75
gap3-oau4	17.1	0.79	1.9	0.088	0.59	1.67	1.0	0.106	0.74
hop2-murn1	17.4	0.39	1.0	0.111	0.59	1.67	1.0	0.114	0.61

Table 4.4 – Resulting mean error rate $\mathcal{E}_{\text{mean}}$ of the wet dry classification algorithm with the corresponding optimum values (also depicted in Figure 4.5) of σ and f_{divide}. Also listed are the near optimum values for which f_{divide} follows the reciprocal of the link length (see text for details) and $\sigma = 1$. For comparison with the link length, the reciprocal of f_{divide} is given. The correlation coefficients R^2 stem from the comparison of the link-derived rain rates with rain gauge data in section 4.4 using the near optimum values. A window length of 256 min was used in the underlying analysis.

increasing link length.

All the described effects on the dry and wet detection error rates determine the optimal values of σ and f_{divide} for the mean error rates $\mathcal{E}_{\text{mean}}$ shown in Figure 4.5-c1 to c5. The minimum of $\mathcal{E}_{\text{mean}}$ lies where $\mathcal{E}_{\text{dry}}$ just declined and $\mathcal{E}_{\text{wet}}$ starts to rise ($\sigma \approx 1$) with a bias towards low f_{divide} depending somehow on the link length. The optimal values of σ and f_{divide} for minimal $\mathcal{E}_{\text{mean}}$ are listed in Table 4.4.

Following the idea of a dependence of f_{divide} on the link length l, a suitable value for f_{divide} can be estimated. We assume a maximum propagation speed of near surface rain fields of $v = 10\,\text{m}\,\text{s}^{-1}$ and a propagation along the link direction. The time needed for traveling along the link length is then $t = l/v$. This can be thought of as a convolution of the rain field and a rectangular function (the line integral along the link) of length t. The resulting spectrum is then the spectrum of the rain field multiplied with a sinc function (Fourier transform of a rectangular function), which has its first zero at $f_0 = 1/t$. That is, whatever the shape and hence the spectrum of the rain field is, most of the effect on the RSL spectrum should be contained below $f_0 = 1/t = v/l = 1/l \times 10^{-2}$ Hz with l in kilometers. This of course will in reality depend on the prevailing wind direction, which changes the effective length of the link seen by the passing rain field. Nevertheless, as can be observed in Figure 4.5 (the dashed lines indicate $f_{\text{divide}} = 1/l \times 10^{-2}$ Hz) and seen from the resulting error rates in Table 4.4, the performance with a constant $\sigma = 1$ (indicated by the dotted lines in Figure 4.5) is very close to the absolute optimum.

To strengthen these findings, further research will be needed in particular with a larger number of links at an ideally wide range of lengths also taking into consideration link orientation and wind directions, which can be highly variable in the alpine region of this study. Nevertheless, the results shown here give a strong indication that this method could be applied without calibration, setting $\sigma = 1$ and $f_{\text{divide}} \approx 1/l \times 10^{-2}$ Hz. For the derivation of the rain rates from the RSL in section 4.4, these values will be used.

The same analysis as shown in Figure 4.5 was also conducted with radar data as reference for the performance of the wet/dry classification algorithm. Using radar rainfall as criteria for wet/dry classification is not straightforward though. Radar rain rates are derived from radar reflectivity (as described in section 4.2.4) which can result in very small rain rates for the smallest reflectivity values just above the radar system's detection limit. These small rain rates do not necessarily correspond to real rainfall. Hence, usually a threshold of 0.1 mm h^{-1} is introduced and lower rain rates are set to zero. However, the radar data showed artifacts (identified by careful analysis of the temporal evolution of the spatial radar reflectivity) resulting in rain rates of up to 0.3 mm h^{-1}. For the wet/dry classification performance analysis, thus a compromise between reducing the artifacts (false wet periods) and accidentally neglecting small real rain events had to be found. A threshold of 0.1 mm h^{-1} for the 5 minute radar data was used. Hours were classified as wet if the hourly radar rain rate averaged along the corresponding link was larger than 0.2 mm h^{-1}. The optimal values for σ and f_{divide} yielded by this analysis were close to the ones found using gauge data, resulting in minimum mean error rates of $\mathscr{E}_{\text{mean}} = 0.120$ and $\mathscr{E}_{\text{mean}} = 0.098$ for the links *hop2-murn1* and *hop2-wh0*. As mentioned in section 4.2.4, radar data were not available for the three links around Garmisch-Partenkirchen because of beam blockage due to the mountains.

Because of the higher spatial representativeness of the radar compared to the rain gauge (explained in section 4.3.5), a better performance using radar data was expected. For the link *hop2-wh0*, this proved to be true, although with a marginal improvement from $\mathscr{E}_{\text{mean}} = 0.102$ to $\mathscr{E}_{\text{mean}} = 0.098$. For the link *hop2-murn1*, however, performance decreased slightly from $\mathscr{E}_{\text{mean}} = 0.111$ to $\mathscr{E}_{\text{mean}} = 0.120$. Most likely the mentioned artifacts and the errors introduced by neglecting small rain rates lead to this result.

4.3.5 Limitations

As can be seen from the error rates in Figure 4.5 and Table 4.4, there still remains an amount of misclassifications of wet and dry periods. Some are due to the inability of the algorithm itself, others to the more general problem of precipitation ground truthing.

The rain gauge locations and the farthest point of some links are separated by more than 10 km and up to 1000 m of altitude difference. That is, a rain gauge indicating a dry period does not necessarily mean that there was no rain along the link at all. As mentioned in section 4.3.4, the available radar data, which in principle could serve to overcome this problem, contain small rain rate artifacts and are thus not usable for this task.

Figure 4.6 gives an example of a situation like this where the gauge misses a rain event. The RSL data show three distinct attenuation events: at 06:00, 11:30 and 13:00 UTC. Judging by the course of the RSL, all three stem from precipitation. The rain gauge, however, seems to miss the second event and parts of the third one. Hence, a dry detection error is counted where the algorithm in fact was correct. Unfortunately, a comparison with radar data, which would offer an improved more localized event detection, is not possible for the three links around Garmisch-Partenkirchen because no radar data are available for the test period in summer 2010. The cause for this was a new scan strategy that set the elevation angle of the radar lower for the precipitation scan. Hence, the beam is blocked by the mountain range

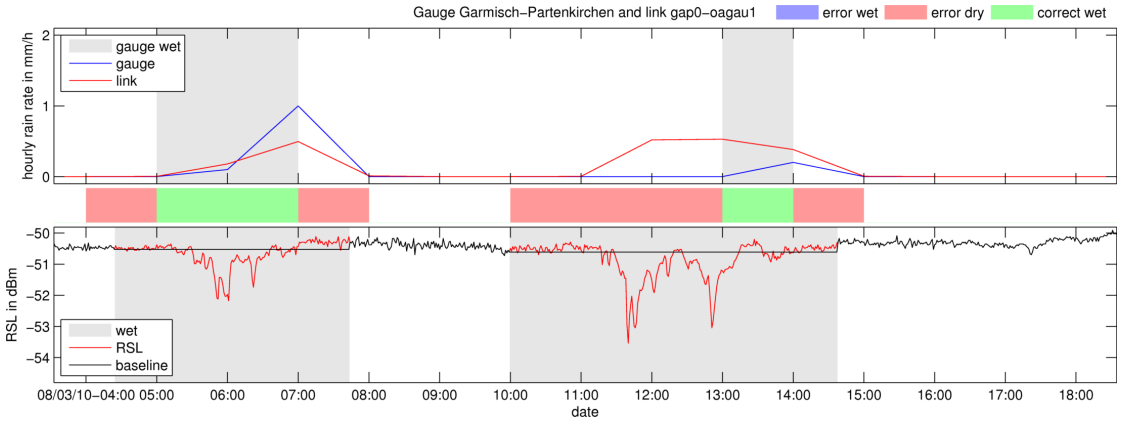

Figure 4.6 – Example of the limitations of the proposed wet/dry classification algorithm. Shown are time series of the minute resolution RSL data from the link *gap0-gap4* (bottom plot in red), the hourly link-derived rain rate (top plot in red) and the hourly rain rate from the gauge Garmisch-Partenkirchen. Note: the hourly data are derived according to the DWD standard (e.g. 12:00 UTC mean value is averaged from 10:50 to 11:50 UTC) and the classification of a period as wet or dry applies for the whole hour before the value's timestamp (e.g. from 11:00 to 12:00 UTC for the 12:00 UTC value). The colors indicating the errors correspond to the hourly data.

north of Garmisch-Partenkirchen.

Besides the problem with the spatial representativeness of rain gauges, Figure 4.6 also shows a detection limitation of the algorithm itself. For both the events at 06:00 and 11:30 UTC, a wet period is detected already one hour before and after the actual attenuation event. The cause for this broadening of the wet detection period is that the 256 min sliding window used for the spectra calculation sees large attenuation peaks 128 points (i.e. 128 min) before and after the period it classifies. The effect is mitigated by the use of the Hamming window weakening the influence from the points at the window edges, but not enough. Remedy could be found by shortening the window length, but as discussed in section 4.3.4 this would implicate other drawbacks. Although the derived rain rates for the wrongly classified period are negligible because there is almost no attenuation, this still increases the error rate. The obvious solution, weighting the detection errors with the derived rain rates to emphasize errors leading to high rain rates, is problematic. It would emphasize those dry detection errors mentioned in the previous paragraph, when a rain gauge misses a rain event clearly observed by the link.

The same limitation is visible in the example in Figure 4.7. The strong attenuation event at 14:00 to 15:00 UTC also is preceded by more than one hour of wet detection without attenuation. Again, the uncertainty of the gauge as the rain event indicator is present. Between 14:00 and 15:00 UTC, the link yields $\approx 5\,\mathrm{mm\,h^{-1}}$, whereas the gauge did not record any precipitation. Only the following smaller (presumably more widespread) event is detected.

Another limitation revealed by this example is the correct wet event detection for very light rain events. Starting from 01:00 UTC on the 13 August, the rain gauge at Mount Hoher

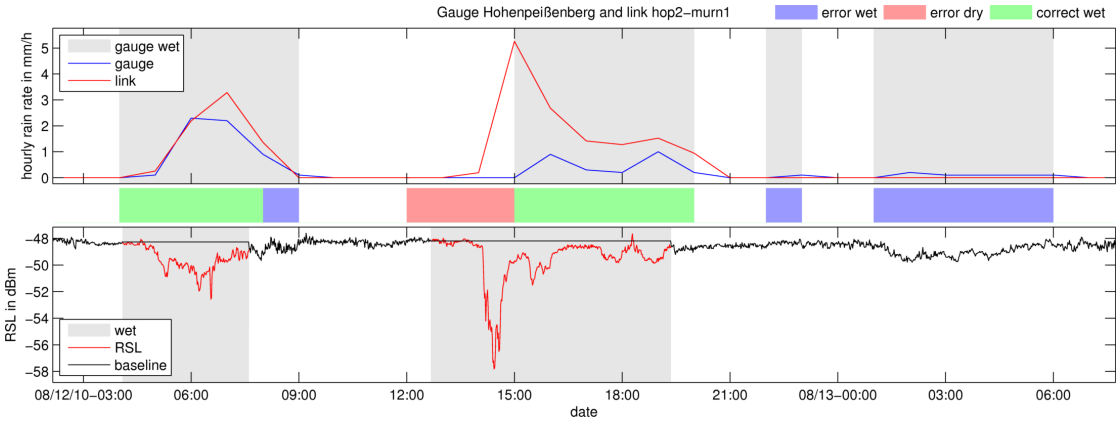

Figure 4.7 – Same plots as in Figure 4.6 but for the link *hop2-murn1* and gauge Hoher Peißenberg.

Peißenberg measures five hours of very light precipitation (0.1–0.2 mm h^{-1}). Looking at the RSL data of the link, a slight decrease ($\approx$ 1 dB) is observable. However, the decrease takes place very slowly (1 dB h^{-1}). That is, in the spectrum only the amplitudes of the lowest four frequencies (from 0.07×10^{-3} Hz $\widehat{=}$ 1/256 min to 2.60×10^{-3} Hz $\widehat{=}$ 1/64 min) will be increased considerably by this very slow change of RSL. For the sum over all 64 low frequencies P_{sumlow}, their contribution is not enough to fulfill the wet period condition $P_{\text{sumlow}} - P_{\text{sumdry}} > \sigma$.

Again, this is a problem of window length. A longer window would have captured the slowly changing RSL level better, however, at the expense of detecting shorter events. Thus, a further improvement of the algorithm may be achieved using spectral analysis tools that are more suitable for revealing simultaneous changes on long and short time scales. Examples could be the discrete wavelet transform or the Hilbert-Huang transform [Huang et al., 1998].

Regarding RSL data sets recorded by the microwave backhaul link network providers themselves, spectral analysis tools may not always be appropriate for a wet/dry classification. Data sets may have a lower temporal resolution, e.g. 15 min [Overeem et al., 2011], or stronger power quantization, e.g. 1 dB [Goldshtein et al., 2009, Schleiss and Berne, 2010]. In particular, a low temporal resolution would limit the applicability of the method proposed here. A data set sampled each 15 min (i.e. at $\approx 1 \times 10^{-3}$ Hz) will not contain frequencies below $\approx 5 \times 10^{-4}$ Hz. Hence, the important frequency range between 2×10^{-3} Hz and 5×10^{-4} Hz (i.e. the range of optimal values for f_{divide}) cannot be resolved. However, with the growing popularity of commercial microwave links as remote sensing tool, the availability of high resolution RSL data directly from the providers can be expected to increase.

4.4 Results

Section 4.3 focused on the rain event detection, which is necessary to determine a RSL baseline. For the application of microwave links as a precipitation remote sensing tool, the crucial parameter is the rain rate it delivers. Hence, rain rates were derived by applying the algorithm introduced above with the values listed in Table 4.4 and the power law relation in equation (2.34). Continuous minute resolution data of RSL records are used throughout the

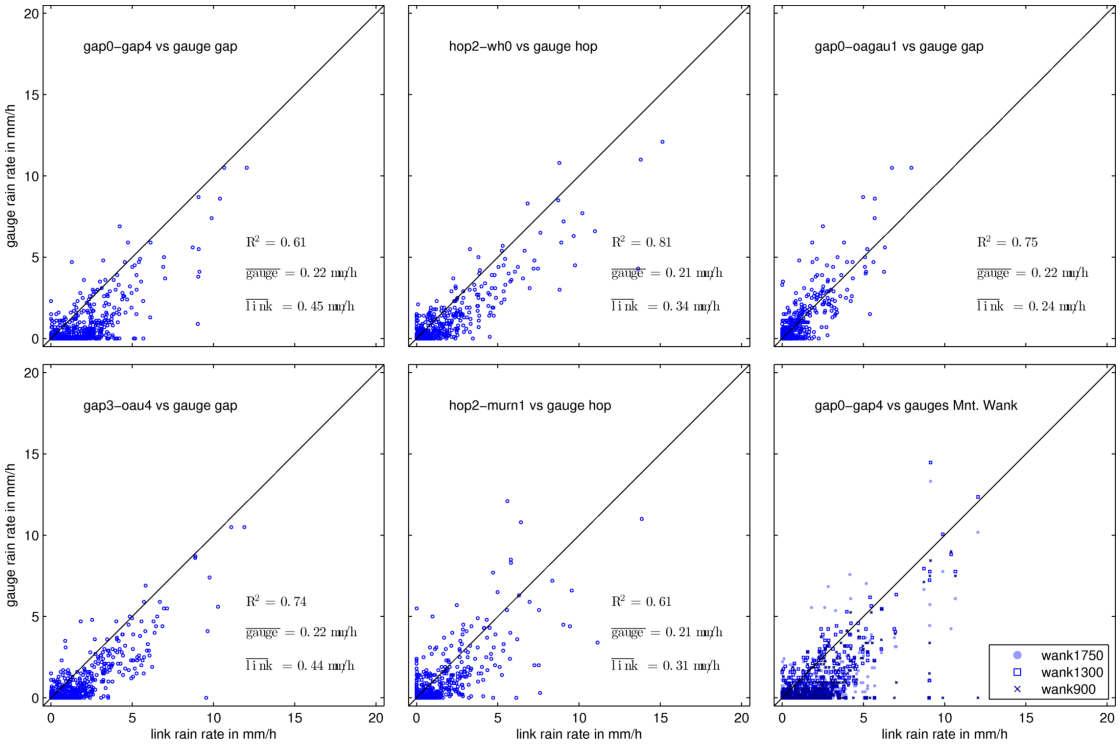

Figure 4.8 – Scatter plots for continuous hourly microwave link rain rate observation and DWD rain gauge data for the period from July 2010 to October 2010. The plot on the bottom right shows gauge data from the rain gauges at different altitudes on Mount Wank directly beneath the link path.

period from July 2010 to October 2010 for all links except for *gap0-gap4*, where two failures of the data acquisition system made several hours of data unusable. The rain rates are then averaged hourly to be comparable with the available rain gauge and radar measurements.

4.4.1 Microwave link – rain gauge comparison

Figure 4.8 gives an overview of the comparison between the hourly rain rate from each of the five links and their closest rain gauge. The sixth plot on the lower right shows data from the link *gap0-gap4* and the three gauges along the slope of Mount Wank beneath the link.

Correlation between the links and the DWD gauges differs from link to link between $R^2 = 0.61$ and $R^2 = 0.81$. A comparison of *gap0-gap4* with our own gauges directly beneath the link on the slope of Mount Wank instead of the DWD gauge does not provide any further improvement. A look at the time series (not shown here) revealed that some events not recorded by the DWD gauge were detected by the gauges at the higher elevations (which can be attributed to precipitation generation due to orographic lifting), but the overall correlation even declined. The advantage of the better spatial representativeness might have been outweighed by the errors attributed to the steep orography and the forest cover at the gauge locations.

In general for all links, problems in the range of small rain rates can be observed, especially along the axes. The values directly on the axes (i.e. the rain gauge or the link measures zero

rainfall but the respective other measurement yields a rain rate greater than zero) stem from the classification errors mentioned in section 4.3.5. The dry detection errors lead to values on the x-axis, wet detection errors to values on the y-axis.

For all links, except *gap0-oagau1*, an overestimation of rain rates is observable, with the mean link rain rate being up to twice the gauge rain rate. Besides the uncertainty of the gauges, this can be due to the uncertainty of the a- and b-values from the power law in equation (2.34) which are not specifically adapted to the rainfall climatology (that is the prevailing DSD type). Furthermore, the non-linearity of the power law leads to overestimation of rain rates because of the heterogeneity of rainfall along the links. This effect increases with lower frequencies (below ≈ 30 GHz) and increasing link length. The observed overestimation for the five links can however not be explained by these effects alone. It is noted that the link with the highest frequency, *gap0-oagau1* ($f = 23$ GHz), yields almost no overestimation though. A further crucial effect leading to overestimation is the additional attenuation introduced by the water film present on the antenna during a rain event. Correction methods for the wet antenna effect exist [Kharadly and Ross, 2001, Leijnse et al., 2008, Minda and Nakamura, 2005, Overeem et al., 2011], but all implicate further uncertainties. Hence, omitting wet antenna correction is a reasonable choice, if, as in the case of this analysis, no reliable ground truth for the absolute rain rates along the links exists and no information on the antenna radome type is available.

4.4.2 Microwave link – weather radar comparison

For the two links connecting Mount Hoher Peißenberg with the cities of Weilheim and Murnau, radar data are available throughout the test period. The radar data are processed according to the description in section 4.2.4 and setting rain rates less than 0.1 mm h^{-1} to zero. The results are then averaged along the corresponding link path. Each pixel is attributed a weight based on the fraction of link length passing through it. Figure 4.9 shows the resulting rain rates for link and radar as well as a comparison of the gauge at Mount Hoher Peißenberg with the radar path average data along the link towards Weilheim.

In comparison with the gauge-link correlation from Figure 4.8, a significant improvement can be observed for the link *hop2-murn1*, as R^2 increases from 0.61 to 0.81. There are still points along the y-axis indicating that the link may have missed a precipitation event, resulting from the error rate for wet detection. However, many of the dry and wet detection errors from Figure 4.8 vanished. The low spatial representativeness of the gauge seemed to be a major cause for the poor performance of the long link *hop2-murn1* (17.4 km). The problem of the artifacts in the radar reflectivity field, which hampered the wet/dry classification performance analysis with the radar data, is not that severe here since the very small rain rates caused by the artifacts only have a large impact in the classification of wet periods. Correlation for the link *hop2-wh0* also increased, from an already high $R^2 = 0.81$ to $R^2 = 0.85$. Just as for the link *hop2-murn1*, the main improvement can be observed when the gauge seemed to have underestimated or completely missed rain events. Overestimation of the links is also less severe here.

The comparison of the gauge rain rates against the averaged radar rain rates along the

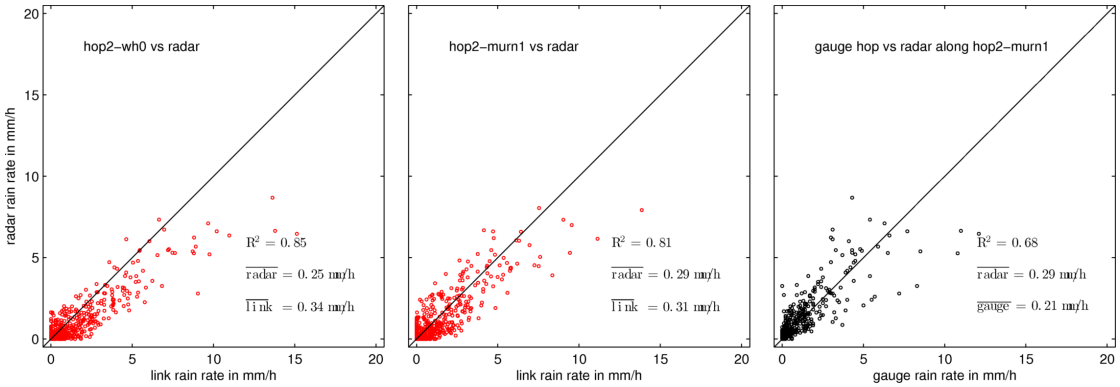

Figure 4.9 – Scatter plots for continuous hourly microwave link rain rate observation and DWD weather radar data along the links for the period from July 2010 to October 2010. The plot on the right gives a comparison of data from the rain gauge at Mount Hoher Peißenberg and the radar along the link *hop2-wh0*.

link *hop2-murn1* (shown on the right in Figure 4.9) emphasizes the problem of rain gauge measurements. For low rain rates the error is small, but with higher rain rates, which mostly occur on smaller horizontal scales, the error increases. Radar rain rate availability is thus desired for the whole test region.

4.5 Conclusion

4.5.1 Summary

Four months of continuous RSL data from five commercial backhaul links in the pre-alpine and alpine region of Southern Germany have been analyzed. To derive rain rates from these data, a classification into wet and dry periods had to be performed to account for fluctuations during dry conditions. To do so, a new classification algorithm using short-time Fourier transform was introduced. It is based on the fact that spectra of wet periods, in contrast to dry periods with strong fluctuations, exhibit a significant deviation from mean dry spectra in the low frequency regime. To decide whether a period is wet or dry, sums of spectral amplitudes are compared against a threshold. Using rain gauge data (and, where possible, also radar data) as ground truth, optimal values for the threshold σ and the spectrum division frequency f_{divide} could be identified for the five links. Analysis showed that error rates are still near the optimum if f_{divide} is derived from the link length and a constant $\sigma = 1$ is used.

Misclassifications of the presented wet/dry classification algorithm are partly due to the low spatial representativeness of rain gauge measurements and limitations of the classification algorithm in detecting the different types of rain events (short and strong, long lasting and weak).

Using the near optimal values f_{divide} determined by the link length and a constant threshold $\sigma = 1$, rain rates were derived throughout the entire four-month test period. Good correlation (up to $R^2 = 0.81$) was found between link and rain gauge data. Using radar data averaged along the links, correlation could be improved showing that rain gauge data might not always

be the best ground truth for microwave link studies. In summary, this study confirmed that commercial microwave links can be used to continuously measure rain rates over complex terrain in summer and autumn conditions.

4.5.2 Outlook

For a further improvement of the wet/dry classification algorithm (especially for the simultaneous detection of short and long events), spectral analysis tools different from Fourier transform may be considered. The determination of f_{divide} from the link length should also be further investigated. A more detailed analysis exploiting a larger number of links and taking into account link frequency, altitude and in particular wind speed and direction could provide useful additional information. With detailed knowledge of the relation of f_{divide} and σ on the given link parameters, the need for error-prone ground truthing could be avoided. This is especially important for potential future applications, e.g. in developing countries where ground truth sources are scarce. Furthermore, the algorithm's performance for longer time series spanning over all seasons should be investigated. For example, winter conditions with sleet, snow and antenna icing will pose further challenges.

Where radar-, gauge- and link measurements are available, a merging of all three data sources may provide the opportunity to obtain improved spatio temporal distributions of rainfall for all kinds of hydrological analyses.

5 Conclusion

This chapter will summarize the work of this thesis, discuss the results and given an outlook on future research in the field of remote sensing using microwave transmission devices.

5.1 Summary

Theory of microwave interaction with precipitation and humidity

The first main part of this thesis focused on the description of the theoretical relation of the interaction of microwave radiation with precipitation and humidity. Starting from the microwave scattering on single drops, the attenuation caused by an ensemble of drops was deduced. The effect of the drop size distribution on the relation between rain rate R, attenuation A and differential attenuation ΔA was then studied. For 35 GHz the A-R relation is very insensitive to changes in the DSD type for rain rates smaller than 15 mm/h (see Figure 2.8). For 22 GHz the opposite is the case. Here the sensitivity to changes in the DSD type is low for high rain rates, in particular for vertical polarization. ΔA is less sensitive to rain, but exhibits a larger dependence on the DSD type.

In addition to the attenuation caused by rain drops, the attenuating effect of water vapor was studied. It was shown that the effect is small compared to the rain induced attenuation and hence can easily be masked by noise stemming from other atmospheric phenomena or from the observation system's electronics. The analysis of the relation between phase delay and refractivity showed that an observation of water vapor changes via phase delay measurements is far more sensitive.

Transmission experiment

In the second main part of this thesis the details of a dual frequency dual polarization microwave transmission experiment were presented: From the definition of the main requirements, to the elaboration of a feasible concept, to the construction work at the test site and the actual test site setup. The final system operates two pulsed monostatic HF transmit/receive stages, at 22.235 GHz and at 34.8 GHz, simultaneously with alternating horizontal and vertical polarization. The four independent attenuation measurements were analyzed concerning the dependence of the derived rain rate on the DSD. An on-site disdrometer was used to provide the ground truth for the DSD. Comparison between A and ΔA measured by the transmission experiment and A and ΔA derived from the disdrometer DSD showed good agreement. The

pronounced sensitivity of the ratio $\Delta A/A$ on DSD changes suggests a future use of these line integrate attenuation measurements to derive line integrated estimates of the DSD.

The transmission experiment was also used to derive changes of absolute humidity from phase delay measurements at a temporal resolution of 20 Hz. These data were averaged to 10 minute values to be able to compare them to data from the on-site weather station. Good agreement was observed for both frequencies, 22 GHz and 35 GHz, with R^2=0.79 and R^2=0.77, respectively (see Figure 3.16).

Commercial microwave links

The third main part of this thesis concentrated on the analysis of data from commercial microwave links to derive line integrated rain rate information. Five links in southern Germany were used. They provided minute resolution averages of the RSL with a power quantization smaller than 0.05 dBm. Due to the strong fluctuations during clear sky conditions a new detection algorithm for rain events had to be developed. The high resolution of the RSL data allowed the implementation of a STFT based algorithm. Analysis of five month of RSL data of the five microwave links showed that the algorithm's parameters can be set according to the link path length without any further calibration. The performance with these standard parameters (mean detection error rate approximately 12%) deviated only slightly from the performance with optimally calibrated parameters (mean detection error rate approximately 10%). Over the analysis period of five months, the comparison of the microwave link derived rain rates with gauge and radar data showed good agreement with correlations up to R^2=0.81 and R^2=0.85, respectively.

5.2 Discussion

Transmission experiment

The validation of the attenuation measurements, using the on-site disdrometer data, ensured that the transmission experiment is working as expected. For the two validation periods, all four attenuation measurements were in good agreement with the attenuation that was calculated from the disdrometer's DSD. The analysis of longer time series was, however, hampered by strong fluctuations of the received signal level. Since these fluctuations affected in particular the 22 GHz system with its wider beam width, their most probable cause is multipath propagation.

Nevertheless, the available data set illustrated the importance of a flexible A-R power law, which accounts for variations of the DSD (see Figure 3.12 on page 56). That is, knowledge of the DSD is important to get the most accurate rain rate estimations from attenuation measurements, even though the A-R relation is quite insensitive to the choice of the assumed DSD type compared to the weather radar Z-R relation.

The DSD is a crucial parameter for all microwave based precipitation remote sensing methods. Hence, the potential estimation of a path averaged DSD from two or more attenuation measurements of the transmission experiment could be an important advancement in DSD observation techniques. Rincon and Lang [2002] already showed that the estimation of path averaged DSDs is feasible. They, however, only had two attenuation measurements

available. Hence, they had to keep one parameter of the gamma DSD (see equation 2.4) fixed. By using the four attenuation measurements provided by the transmission experiment, all three parameters of the gamma DSD could be fitted, while the remaining fourth attenuation measurement would improve the robustness of this approach.

Using the phase delay measurements of the transmission experiment, line integrated estimates of humidity with high temporal resolution (20 Hz) were derived. They showed good agreement with the station observations. With a path length of 660 m, the scale which is covered by the averaging is similar to the horizontal resolution of high resolution NWP models. Since their ability to accurately forecast convective events is significantly influenced by variations in the boundary layer fields of moisture and temperature [Crook, 1996, Ducrocq et al., 2002] the line integrated humidity observations could help to improve validation or initialization, and hence forecasting skill.

The phase delay measurements were not without problems, though. Significant deviations between phase delay derived humidity and the station observations were present, mainly in the morning hours. Most likely they stemmed from temperature and humidity gradients at the test site since the weather station measures at 2 meters above the ground, whereas the microwave transmission experiment measures 10 meters above the ground. However, problems with the instrument stability or the alignment, e.g. due to temperature induced mechanical deflection, could also be potential causes.

To study these deviations of the phase delay measurements in more detail, additional ground truth observations, i.e. more humidity and temperature sensors would be required at the test site. They would also allow to investigate if the line integrated microwave transmission measurements averages the spatial heterogeneity of humidity correctly. The same holds true for precipitation. Additional ground truth observations for rain rate and DSD would be needed to evaluate how well the line integrated attenuation measurements capture and average the spatial variation of the rain rate and DSD.

Commercial microwave links

Analyzing data from five commercial microwave links showed that they can provide precipitation information with quality similar to that of weather radars and rain gauges. Correct processing of the data is, however, crucial. The developed STFT based wet-dry classification algorithm was found to be able to perform close to its optimum without empirical calibration to each of the links. Only the length of the individual links are used to adjust the algorithm. For an operational application this would be a crucial advantage, because calibration of the wet-dry classification algorithms is not feasible for a countrywide network of links. Since only five microwave links have been available for analysis in this work, a validation with an increased number of links is necessary to prove the robustness of the algorithm, though.

Recent results have demonstrated the possibilities that arise when a very large number of commercial microwave links is available. Based on data of approximately 2400 links in the Netherlands, Overeem et al. [2013] showed that commercial microwave link networks can provide countrywide spatial rain rate estimates similar to weather radar based products.

However, the advantages of the line integrated measurements of microwave links, in

particular in urban and mountainous regions, have to be investigated further. In these regions radar and gauges are prone to errors. Microwave links are expected to outperform them concerning the quality of the retrieved rain rates. But validating the advanced performance is challenging, since gauge or radar data, which are considered to have poorer quality in these regions, commonly are used as ground truth. Hence the proof of the eventual advantages of microwave links over radar and rain gauges is still to be made. Fencl et al. [2013] made a first step in this direction by using synthetic microwave link rain rate observations to simulate the pipe flow of the sewer system of Prague. They observed an improvement of the modeled pipe flow when using rain rates derived from microwave links compared to cases where only rain rates from rain gauges were used.

Commercial microwave links can also be used to mitigate the uncertainties of weather radar data processing. Based on the data that was used in this work, Trömel et al. [2014] showed that commercial microwave links can improve the attenuation correction of operational weather radars.

To fully exploit its potential, the major task for microwave link rain rate observation, however, still remains to understand and mitigate all uncertainties inherent to commercial microwave link measurements: The wet antenna attenuation, the power quantization, the electronic systems drift and last but not least the remaining, yet to be explained, fluctuations of the RSL.

5.3 Outlook

Transmission experiment

In addition to the path averaged DSD estimation based on the four attenuation measurements, the specific differential phase K_{dp} in $^\circ\,\mathrm{km}^{-1}$ should be included in the analysis. It is caused by the different horizontal and vertical extent of the scatterers, i.e. the oblate spheroid shape of rain drops. Compared to differential attenuation ΔA, or the differential reflectivity Z_{dr} from radar measurements, which depend only on the different horizontal and vertical diameter of rain drops, K_{dp} is very sensitive to the drop concentration [Bringi and Chandrasekar, 2001]. It hence adds an additional independent measurement that can be used to estimate the path averaged DSD. The analysis of K_{dp} can be carried out with the data that has already been acquired during the operational phase of the transmission experiment.

A further new opportunity for analysis will be provided by the 25 KHz raw data sampling mode. It could be used to study rain drop Doppler spectra, both in transmission and reflection configuration, similar to the electromagnetic simulation performed by Hipp et al. [2011]. They modeled the transmission experiment's configuration and did a drop-by-drop scattering calculation. Combining the possible insights, from both, experiment and simulation, could yield further insight in the dynamics of precipitation on the sub-km scale.

Since the TERENO test site in Fendt also provides flux measurements from an eddy correlation tower, a comparison with the 20 Hz data from the transmission experiment is envisaged. The attenuation data can be analyzed similar to data from microwave scintillometers [Leijnse et al., 2007a, Meijninger et al., 2006], while the phase delay data could add additional insight.

The most important task, however, is to improve the validation of the line integrated

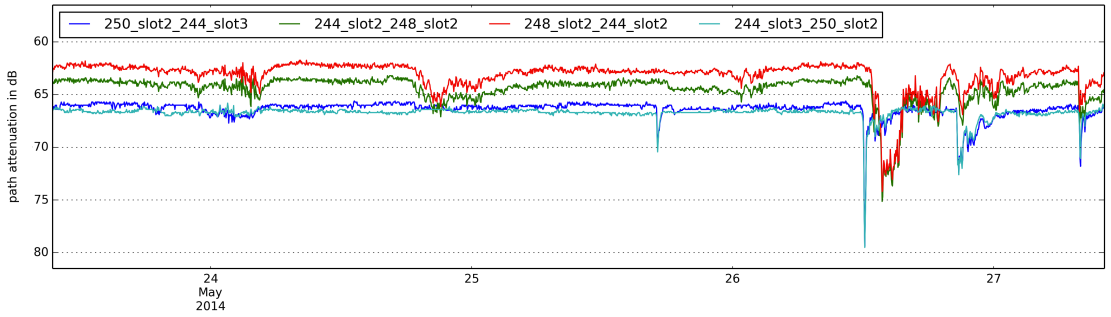

Figure 5.1 – Example time series of path attenuation data (Tx-level minus Rx-level) from two bidirectional microwave links, acquired with the new data acquisition system at Ericsson. In this case the link locations are identified by a three digit number and the relevant link path (since there may be several at each link location) are identified by the slot number. E.g. link *250_slot2_244_slot3* and link *244_slot3_250_slot2* hence operate along the same path, but in different directions.

attenuation and phase delay measurements. Therefore, additional ground truth observations will be installed at the test site. A second disdrometer and several humidity sensors will reveal the spatial heterogeneity of the DSD and atmospheric humidity and hence allow for better interpretation of the microwave transmission experiment measurements.

The additional precipitation ground truth will also enable a very precise determination of the onset and end of a rain event on the link path and hence help with testing wet-dry classification algorithms and estimating the wet antenna attenuation after a rain shower.

Commercial microwave links

Even though the data acquisition with the custom loggers at the commercial microwave link towers has the advantage of high temporal- and power resolution, the main drawback is significant. The costs for installation and maintenance render an extension of this method to a larger number of links impossible. Hence, a software tool for an IT based central data acquisition is currently being developed with the assistance of engineers at Ericsson GmbH. After several test runs in a closed lab environment, the new data acquisition was installed at the central control server of Ericsson's operational microwave link network in May 2014. In the first phase, data of only two microwave links was recorded to proof the feasibility and check whether the data acquisition interferes with the operation of the microwave link network. The results of this first successful test are shown in Figure 5.1.

Power quantization is determined by the link hardware and is 0.3 dB for the Rx-level and 1 dB for the variable Tx-level. As can be seen from the almost four days of data, the low power fluctuations during clear sky conditions and the rain events are perfectly visible. Furthermore the two bidirectional measurements along one path (dark and light blue line, red and green line) show very good agreement during the rain events. During clear sky condition the two signals deviate slightly. This effect could maybe also be used in the future to detect the onset of a rain event.

After the first test run in the operational network, the subsequent successful testing phase

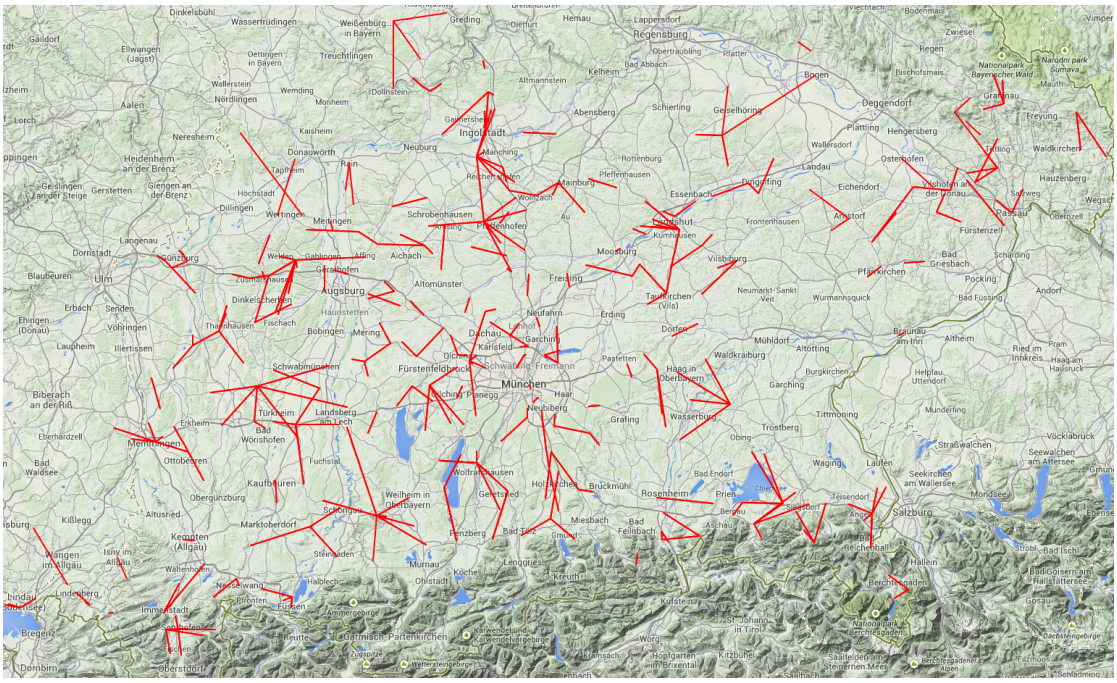

Figure 5.2 – Map showing the 280 bidirectional links that will be available in the next stage of the new data acquisition system at Ericsson. In this stage only links in southern Bavaria and only the newest generation of hardware are available.

increased the number of links to 60. The next step will be to extend the coverage to the whole of southern Bavaria. Figure 5.2 shows the location of the 280 links that will be included. It shall be noted, that this is just a subset of the microwave links in that area, though. Only the newest generation of Ericsson microwave links is included. Step by step the older hardware generations will be made available, which will fill a lot of the gaps on the map. The final aim is to cover the whole of Germany with the new data acquisition system, providing real-time delivery of the Rx- and Tx-level measurements of 5000 to 10000 links.

Compared to Germany, where the German Weather Service operates 16 C-band weather radars with a countrywide coverage, most developing countries completely lack weather radars. Hence, the addition of microwave link derived rainfall information will be even more beneficial there. Doumounia et al. [2014] have already shown that it is feasible to use commercial microwave links in West-Africa to derive rain rates. Following their first application with yet only one link, a workshop on the use of commercial microwave links as remote sensing tool will be held in Burkina Faso in spring 2015 to promote this new technique in West-Africa.

In conclusion it can be said that line integrated microwave measurements can play an important role in the crucial advancement of precipitation and humidity observations, which are required for the mitigation of the predicted climate change impacts by improving short- and long term forecasting.

Bibliography

Andrieu, H., Creutin, J. D., Delrieu, G., and Faure, D. (1997). Use of a weather radar for the hydrology of a mountainous area. part i: Radar measurement interpretation. *Journal of Hydrology*, 193(1-4):1–25.

Atlas, D. (1964). Advances in radar meteorology. In *Advances in Geophysics*, number 10, page 385. Academic Press.

Atlas, D., Srivastava, R. C., and Sekhon, R. S. (1973). Doppler radar characteristics of precipitation at vertical incidence. *Reviews of Geophysics*, 11(1):1–35.

Atlas, D. and Ulbrich, C. W. (1977). Path- and area-integrated rainfall measurement by microwave attenuation in the 1–3 cm band. *Journal of Applied Meteorology*, 16(12):1322–1331.

Aydin, K. and Daisley, S. (2002). Relationships between rainfall rate and 35-GHz attenuation and differential attenuation: modeling the effects of raindrop size distribution, canting, and oscillation. *Geoscience and Remote Sensing, IEEE Transactions on*, 40(11):2343–2352.

Bartels, H., Weigl, E., Reich, T., Lang, P., Wagner, A., Kohler, O., and Gerlach, N. (2004). Abschlussbericht projekt RADOLAN. Technical report, Deutscher Wetterdienst.

Bean, B. R. and Dutton, E. J. (1968). *Radio meteorology*, volume pp 435. Dover Publications.

Beard, K. V. (1976). Terminal velocity and shape of cloud and precipitation drops aloft. *J. Atmos. Sci*, 33(5):851–864.

Bennitt, G. V. and Jupp, A. (2012). Operational assimilation of GPS zenith total delay observations into the met office numerical weather prediction models. *Monthly Weather Review*, 140(8):2706–2719.

Berne, A. and Krajewski, W. (2013). Radar for hydrology: Unfulfilled promise or unrecognized potential? *Advances in Water Resources*, 51:357–366.

Berne, A. and Schleiss, M. (2009). Retrieval of the rain drop size distribution using telecommunication dual-polarization microwave links. In *34th Conference on Radar Meteorology*.

Bevis, M., Businger, S., Herring, T., Rocken, C., Anthes, R., and Ware, R. (1992). GPS meteorology- remote sensing of atmospheric water vapor using the global positioning system. *Journal of Geophysical Research*, 97(D14):15787–15801.

Bolton, D. (1980). The computation of equivalent potential temperature. *Mon. Wea. Rev*, 108(7):1046–1053.

Borowska, L., Ryzhkov, A., Zrnić, D., Simmer, C., and Palmer, R. (2011). Attenuation and differential attenuation of 5-cm-wavelength radiation in melting hail. *Journal of Applied Meteorology and Climatology*, 50(1):59–76.

Bringi, V. N. and Chandrasekar, V. (2001). *Polarimetric Doppler weather radar: Principles and applications*. Cambridge Univ Pr.

Chuang, C. C. and Beard, K. V. (1990). A numerical model for the equilibrium shape of electrified raindrops. *Journal of the Atmospheric Sciences*, 47(11):1374–1389.

Chwala, C., Gmeiner, A., Qiu, W., Hipp, S., Nienaber, D., Siart, U., Eibert, T., Pohl, M., Seltmann, J., Fritz, J., and Kunstmann, H. (2012). Precipitation observation using microwave backhaul links in the alpine and pre-alpine region of southern germany. *Hydrol. Earth Syst. Sci.*, 16(8):2647–2661.

Chwala, C., Kunstmann, H., Hipp, S., and Siart, U. (2014). A monostatic microwave transmission experiment for line integrated precipitation and humidity remote sensing. *Atmospheric Research*, 144:57–72.

Crook, N. A. (1996). Sensitivity of moist convection forced by boundary layer processes to low-level thermodynamic fields. *Monthly Weather Review*, 124(8):1767–1785.

Cuccoli, F., Facheris, L., Tanelli, S., and Giuli, D. (2001). Microwave attenuation measurements in satellite-ground links: the potential of spectral analysis for water vapor profiles retrieval. *Geoscience and Remote Sensing, IEEE Transactions on*, 39(3):645 –654.

David, N., Alpert, P., and Messer, H. (2009). Technical note: Novel method for water vapor monitoring using wireless communication networks measurements. *Atmos. Chem. Phys.*, 9:2413–2418.

Doumounia, A., Gosset, M., Cazenave, F., Kacou, M., and Zougmore, F. (2014). Rainfall monitoring based on microwave links from cellular telecommunication networks: First results from a west african test bed. *Geophysical Research Letters*, 41(16):6016–6022.

Ducrocq, V., Ricard, D., Lafore, J.-P., and Orain, F. (2002). Storm-scale numerical rainfall prediction for five precipitating events over france: On the importance of the initial humidity field. *Weather and Forecasting*, 17(6):1236–1256.

Fabry, F., Frush, C., Zawadzki, I., and Kilambi, A. (1997). On the extraction of near-surface index of refraction using radar phase measurements from ground targets. *Journal of Atmospheric and Oceanic Technology*, 14(4):978–987.

Fencl, M., Rieckermann, J., Schleiss, M., Stránský, D., and Bareš, V. (2013). Assessing the potential of using telecommunication microwave links in urban drainage modelling. *Water Science & Technology*, 68(8):1810.

Friedrich, K., Kalina, E. A., Masters, F. J., and Lopez, C. R. (2012). Drop-size distributions in thunderstorms measured by optical disdrometers during VORTEX2. *Monthly Weather Review*, 41:1182–1203.

Gao, B.-C. and Kaufman, Y. J. (2003). Water vapor retrievals using moderate resolution imaging spectroradiometer (MODIS) near-infrared channels. *Journal of Geophysical Research: Atmospheres*, 108(D13):4389.

Goldshtein, O., Messer, H., and Zinevich, A. (2009). Rain rate estimation using measurements from commercial telecommunications links. *Signal Processing, IEEE Transactions on*, 57(4):1616–1625.

Gunn, R. and Kinzer, G. D. (1949). The terminal velocity of fall for water droplets in stagnant air. *Journal of Meteorology*, 6(4):243–248.

Hazenberg, P., Leijnse, H., and Uijlenhoet, R. (2011). Radar rainfall estimation of stratiform winter precipitation in the belgian ardennes. *Water Resources Research*, 47:W02507.

Hipp, S., Siart, U., Chwala, C., Eibert, T., and Kunstmann, H. (2011). Dynamic modelling of atmospheric microwave transmission for precipitation quantification using mie scattering. In *Antennas and Propagation (EUCAP), Proceedings of the 5th European Conference on*, pages 3380–3383.

Ho, C. M., Wang, C., Angkasa, K., and Gritton, K. (2004). Estimation of microwave power margin losses due to earth's atmosphere and weather in the frequency range of 3–30 GHz. Technical report, JPL.

Holt, A., Kuznetsov, G., and Rahimi, A. (2003). Comparison of the use of dual-frequency and single-frequency attenuation for the measurement of path-averaged rainfall along a microwave link. *Microwaves, Antennas and Propagation, IEE Proceedings* -, 150(5):315–20.

Hou, A. Y., Kakar, R. K., Neeck, S., Azarbarzin, A. A., Kummerow, C. D., Kojima, M., Oki, R., Nakamura, K., and Iguchi, T. (2013). The global precipitation measurement mission. *Bulletin of the American Meteorological Society*, 95(5):701–722.

Huang, N. E., Shen, Z., Long, S. R., Wu, M. C., Shih, H. H., Zheng, Q., Yen, N.-C., Tung, C. C., and Liu, H. H. (1998). The empirical mode decomposition and the hilbert spectrum for nonlinear and non-stationary time series analysis. *Proc. R. Soc. Lond. A*, 454(1971):903–995.

Huffman, G. J., Bolvin, D. T., Nelkin, E. J., Wolff, D. B., Adler, R. F., Gu, G., Hong, Y., Bowman, K. P., and Stocker, E. F. (2007). The TRMM multisatellite precipitation analysis (TMPA): Quasi-global, multiyear, combined-sensor precipitation estimates at fine scales. *Journal of Hydrometeorology*, 8(1):38–55.

Ishimaru, A. (1978). *Wave propagation and scattering in random media*, volume 1. Wiley-IEEE Press.

ITU (2003). ITU-r p.838-2: Specific attenuation model for rain for use in prediction methods. *International Telecommunication Union*.

Joss, J. and Waldvogel, A. (1967). Ein spektrograph für niederschlagstropfen mit automatischer auswertung. *Pure and applied Geophysics*, 68(1):240–246.

Joss, J. and Waldvogel, A. (1969). Raindrop size distribution and sampling size errors. *J. Atmos. Sci*, 26(3):566–569.

Kharadly, M. and Ross, R. (2001). Effect of wet antenna attenuation on propagation data statistics. *IEEE Transactions on Antennas and Propagation*, 49(8):1183–1191.

Kleinschmidt, E., Albrecht, F., and Duckert, P. (1935). *Handbuch der meteorologischen Instrumente und ihrer Auswertung*. J. Springer.

Knight, N. C. (1986). Hailstone shape factor and its relation to radar interpretation of hail. *Journal of Climate and Applied Meteorology*, 25(12):1956–1958.

Kumjian, M. R. and Prat, O. P. (2014). The impact of raindrop collisional processes on the polarimetric radar variables. *Journal of the Atmospheric Sciences*, 71(8):3052–3067.

Laws, J. O. and Parsons, D. A. (1943). The relation of raindrop-size to intensity. *Trans. Amer. Geophys. Union*, 24(Part II):452–460.

Leijnse, H., Uijlenhoet, R., and Stricker, J. (2008). Microwave link rainfall estimation: Effects of link length and frequency, temporal sampling, power resolution, and wet antenna attenuation. *Advances in Water Resources*, 31(11):1481–1493.

Leijnse, H., Uijlenhoet, R., and Stricker, J. N. M. (2007a). Hydrometeorological application of a microwave link: 1. evaporation. *Water Resources Research*, 43:W04416.

Leijnse, H., Uijlenhoet, R., and Stricker, J. N. M. (2007b). Hydrometeorological application of a microwave link: 2. precipitation. *Water Resources Research*, 43:W04417.

Leijnse, H., Uijlenhoet, R., and Stricker, J. N. M. (2007c). Rainfall measurement using radio links from cellular communication networks. *Water Resources Research*, 43:W03201.

Liebe, H. J. (1989). MPM—an atmospheric millimeter-wave propagation model. *International Journal of Infrared and Millimeter Waves*, 10(6):631–650.

Liebe, H. J., Hufford, G. A., and Cotton, M. G. (1993). Propagation modeling of moist air and suspended water/ice particles at frequencies below 1000 GHz. In *AGARD Conf. Proc*, volume 542, pages 3.1–3.10.

Liebe, H. J., Hufford, G. A., and Manabe, T. (1991). A model for the complex permittivity of water at frequencies below 1 THz. *International Journal of Infrared and Millimeter Waves*, 12(7):659–675.

Lorenz, E. N. (1965). A study of the predictability of a 28-variable atmospheric model. *Tellus*, 17(3):321–333.

László, F. T. (2011). Ftp2me - THE ftp client library for handheld devices.

Marshall, J. S. and Palmer, W. M. K. (1948). The distribution of raindrops with size. *Journal of Meteorology*, 5(4):165–166.

Meijninger, W., Beyrich, F., Lüdi, A., Kohsiek, W., and Bruin, H. (2006). Scintillometer-based turbulent fluxes of sensible and latent heat over a heterogeneous land surface – a contribution to litfass-2003. *Boundary-Layer Meteorology*, 121(1):89–110.

Messer, H., Zinevich, A., and Alpert, P. (2006). Environmental monitoring by wireless communication networks. *Science*, 312(5774):713.

Minda, H. and Nakamura, K. (2005). High temporal resolution path-average rain gauge with 50-GHz band microwave. *Journal of Atmospheric and Oceanic Technology*, 22(2):165–179.

Mishchenko, M. I., Travis, L. D., and Mackowski, D. W. (1996). T-matrix computations of light scattering by nonspherical particles: A review. *Journal of Quantitative Spectroscopy and Radiative Transfer*, 55(5):535–575.

Montero-Martínez, G., Kostinski, A. B., Shaw, R. A., and García-García, F. (2009). Do all raindrops fall at terminal speed? *Geophysical Research Letters*, 36(11):L11818.

Mueller, G. (1946). Propagation of 6-millimeter waves. *Proceedings of the IRE*, 34(4):181–183.

Mätzler, C. and Martin, L. (2003). Advanced model of extinction by rain and measurements at 38 and 94 GHz and in the visible range. IAP research report, University of Bern, Bern, Switzerland.

Nešpor, V. and Sevruk, B. (1999). Estimation of wind-induced error of rainfall gauge measurements using a numerical simulation. *Journal of Atmospheric and Oceanic Technology*, 16:450.

Olsen, R., Rogers, D., and Hodge, D. (1978). The aR^b relation in the calculation of rain attenuation. *Antennas and Propagation, IEEE Transactions on*, 26(2):318–329.

Overeem, A., Leijnse, H., and Uijlenhoet, R. (2011). Measuring urban rainfall using microwave links from commercial cellular communication networks. *Water Resources Research*, 47:W12505.

Overeem, A., Leijnse, H., and Uijlenhoet, R. (2013). Country-wide rainfall maps from cellular communication networks. *Proceedings of the National Academy of Sciences*, 110(8):2741–2745.

Pruppacher, H. R. and Beard, K. V. (1970). A wind tunnel investigation of the internal circulation and shape of water drops falling at terminal velocity in air. *Quarterly Journal of the Royal Meteorological Society*, 96(408):247–256.

Rahimi, A. R., Holt, A. R., Upton, G. J. G., and Cummings, R. J. (2003). Use of dual-frequency microwave links for measuring path-averaged rainfall. *Journal of Geophysical Research (Atmospheres)*, 108o:4467.

Rahimi, A. R., Upton, G. J. G., and Holt, A. R. (2004). Dual-frequency links–a complement to gauges and radar for the measurement of rain. *Journal of Hydrology*, 288(1-2):3–12.

Rayitsfeld, A., Samuels, R., Zinevich, A., Hadar, U., and Alpert, P. (2012). Comparison of two methodologies for long term rainfall monitoring using a commercial microwave communication system. *Atmospheric Research*.

Rincon, R. F. and Lang, R. H. (2002). Microwave link dual-wavelength measurements of path-average attenuation for the estimation of drop size distributions and rainfall. *IEEE Transactions on Geoscience and Remote Sensing*, 40(4):760–770.

Roberts, R. D., Fabry, F., Kennedy, P. C., Nelson, E., Wilson, J. W., Rehak, N., Fritz, J., Chandrasekar, V., Braun, J., Juanzhen, S., et al. (2008). REFRACTT 2006: Real-time retrieval of high-resolution, low-level moisture fields from operational NEXRAD and research radars. *Bulletin of the American Meteorological Society*, 89(10):1535–1548.

Ruf, C. S., Aydin, K., Mathur, S., and Bobak, J. P. (1996). 35-GHz dual-polarization propagation link for rain-rate estimation. *Journal of Atmospheric and Oceanic Technology*, 13(2):419–425.

Savic, P. (1953). Circulation and distortion of liquid drops falling through a viscous medium. *Natl Res. Counc. Can., Div. Mech. Engng Rep. MT-22*.

Schleiss, M. and Berne, A. (2010). Identification of dry and rainy periods using telecommunication microwave links. *Geoscience and Remote Sensing Letters, IEEE*, 7(3):611–615.

Schönhuber, M., Urban, H., Baptista, J. P. V. P., Randeu, W. L., and Riedler, W. (1994). Measurements of precipitation characteristics by a new distrometer. In *Proceedings of Atmospheric Physics and Dynamics in the Analysis and Prognosis of Precipitation Fields*, pages 15–18.

Sevruk, B. and Zahlavova, L. (1994). Classification system of precipitation gauge site exposure: Evaluation and application. *International Journal of Climatology*, 14(6):681–689.

Smith, D. R., Pumphry, M. E., and Snow, J. T. (1986). A comparison of errors in objectively analyzed fields for uniform and nonuniform station distributions. *Journal of Atmospheric and Oceanic Technology*, 3(1):84–97.

Stratton, J. (1930). The effect of rain and fog on the propagation of very short radio waves. *Proceedings of the Institute of Radio Engineers*, 18(6):1064–1074.

Trömel, S., Ziegert, M., Ryzhkov, A. V., Chwala, C., and Simmer, C. (2014). Using microwave backhaul links to optimize the performance of algorithms for rainfall estimation and attenuation correction. *Journal of Atmospheric and Oceanic Technology*, 31(8):1748–1760.

Ulbrich, C. W. (1983). Natural variations in the analytical form of the raindrop size distribution. *Journal of Climate and Applied Meteorology*, 22(10):1764–1775.

Ulbrich, C. W. and Lee, L. G. (1999). Rainfall measurement error by WSR-88d radars due to variations in z–r law parameters and the radar constant. *Journal of Atmospheric and Oceanic Technology*, 16(8):1017–1024.

Upton, G., Holt, A., Cummings, R., Rahimi, A., and Goddard, J. (2005). Microwave links: The future for urban rainfall measurement? *Atmospheric Research*, 77(1-4):300–312.

Valtr, P., Pechac, P., Kvicera, V., and Grabner, M. (2011). Estimation of the refractivity structure of the lower troposphere from measurements on a terrestrial multiple-receiver radio link. *Antennas and Propagation, IEEE Transactions on*, 59(5):1707–1715.

Waterman, P. C. (1971). Symmetry, unitarity, and geometry in electromagnetic scattering. *Physical review D*, 3(4):825.

Weckwerth, T. M., Pettet, C. R., Fabry, F., Park, S. J., LeMone, M. A., and Wilson, J. W. (2005). Radar refractivity retrieval: Validation and application to short-term forecasting. *Journal of Applied Meteorology*, 44(3):285–300.

Wolf, D. A. d. (2001). On the laws-parsons distribution of raindrop sizes. *Radio Science*, 36(4):639–642.

Zinevich, A., Alpert, P., and Messer, H. (2008). Estimation of rainfall fields using commercial microwave communication networks of variable density. *Advances in Water Resources*, 31(11):1470–1480.

Zinevich, A., Messer, H., and Alpert, P. (2010). Prediction of rainfall intensity measurement errors using commercial microwave communication links. *Atmospheric Measurement Techniques*, 3:1385–1402.

Danksagung

Mein Dank gilt:

- *Prof. Dr. Harald Kunstmann* für die Möglichkeit in einem spannenden interdisziplinären und internationalen Projekt mitzuarbeiten und zu promovieren. Vielen Dank für deine Betreuung, die Einführung in die Wissenschaftswelt und das in mich gesetzte Vertrauen, auch über die Zeit des Doktorandenvertrags hinaus.
- *Prof. Dr. Jucundus Jacobeit* für die Übernahme des Zweitgutachtens und die dafür aufgewendete Zeit und Arbeit.
- *Prof. Dr. Uwe Siart* für die Betreuung während der Planungs- und Aufbauphase des Tranmissionsexperiments. Ohne deine Hilfe hätte mein Quereinstieg in das Feld der Mikrowellenfernerkundung sicher zeit- und kostenintensive Umwege genommen.
- Dem Team der *Mechanik Werkstatt am Lehrstuhl für Hochfrequenztechnik der TUM* für die Planung und Ausführung der mechanischen Komponenten des Transmissionsexperiments sowie für die präzise Fertigung des Corner-Reflektors.
- Dem Team der *Mechatronik am IMK-IFU*, deren Know-How und Einsatz für jede Installation vom Messgeräten im Felde unabdingbar ist.
- Unseren *Projektpartner bei Ericsson*, Herrn Jürgen Fritz, Herrn Jürgen Alschbach, Herrn Ronald Riedel und Herrn Reinhard Gerigk. Nur Dank ihrer wohlwollenden Zusammenarbeit konnten wir die erste Datenerfassung für Richtfunk in Deutschland realisieren und nun ein IT-basiertes zweites System entwickeln.
- *Meinen Kollegen* in der *AG Kunstmann* für das tolle wissenschaftliche und soziale Umfeld.